

TECHNICAL UNIVERSITY OF CRETE

DEPARTMENT OF ELECTRONIC AND COMPUTER ENGINEERING



DIPLOMA THESIS

Development of a Microelectronic System
for Maximizing the Energy Produced by
Thermoelectric Generators

by

ALEXANDROS PARASKEVAS

COMMITTEE:

EFTICHIOS KOUTROULIS, Assistant Professor (Supervisor)

KONSTANTINOS KALAITZAKIS, Professor

GEORGIOS STAVRAKAKIS, Professor

CHANIA, 2013

Acknowledgements

I would like to express my gratitude to my supervisor professor who trusted me with and guided me towards such an interesting topic.

I would like to thank all those who provided me with samples and those who made their work and research freely available in the internet.

Last but not least, I would like to thank my family, my loved ones and my colleagues for their continuous support.

Abstract

Thermoelectric generators (TEGs) are solid state devices used for energy harvesting purposes, utilizing the waste heat produced by heat sources. TEG devices are suitable for use in applications such as powering Wireless Sensor Networks, the electronic systems of vehicles etc. The present work focuses on the development of a novel microelectronic system for the maximization of the energy produced by TEG devices, which is based on tracking their Maximum Power Point (MPP) and reducing the total power consumption of the corresponding control system. The proposed system is pre-programmed to operate on a specific MPP locus in order to maximize the power transferred to the system load. The system consists of a power-conditioning circuit with a closed-loop controller to achieve load-matching conditions. The system load is a battery bank, which also provides power to the control system, making the whole system fully autonomous. In order to evaluate the performance of the developed system, several experiments were performed by employing various configurations of TEG modules as power sources. The Maximum Power Point Tracking (MPPT) accuracy of the proposed system is much higher compared to that of past-proposed MPPT systems for TEGs and higher than 99% in most cases investigated. Also, the power-consumption of the proposed system is much lower compared to that of other widely-used MPPT approaches, due to the lower computational complexity of the proposed MPPT method.

Contents

| | |
|---|-----------|
| Acknowledgements..... | ii |
| Abstract..... | iv |
| Contents | vi |
| 1. Introduction..... | 1 |
| 1.1 Thermoelectric generators study motivation..... | 1 |
| 1.2 Thesis justification..... | 1 |
| 1.3 Thesis objectives | 3 |
| 1.4 Thesis outline..... | 4 |
| 2. TEG Model Analysis..... | 6 |
| 2.1 Introduction | 6 |
| 2.2 TEG basic structure and model | 6 |
| 2.2.1 TEG basic structure..... | 6 |
| 2.2.2 TEG equivalent circuit | 9 |
| 2.2.3 Electro-thermal interactions during operation..... | 10 |
| 2.3 TEG model calculation..... | 11 |
| 2.4 Simulations based on theoretical model..... | 13 |
| 2.4.1 Simulation results for one eTEG HV56..... | 13 |
| 2.4.2 Simulation results for two eTEG HV56 connected in series | 16 |
| 2.4.3 Simulation results for two eTEG HV56 connected in parallel..... | 18 |
| 3. Past-Proposed MPPT Methods for TEGS..... | 21 |
| 3.1 Significance of MPPT | 21 |
| 3.2 MPPT techniques..... | 22 |
| 3.2.1 Perturb and Observe (P&O)..... | 22 |
| 3.2.2 Incremental Conductance (INC) | 24 |
| 3.2.3 Fractional Open-Circuit Voltage / Short-Circuit Current | 27 |

| | | |
|-----------|---|-----------|
| 3.2.3.1 | Fractional Open-Circuit Voltage..... | 27 |
| 3.2.3.2 | Fractional Short-Circuit Current | 27 |
| 4. | The Proposed MPPT System | 29 |
| 4.1 | Introduction | 29 |
| 4.2 | TEG energy source | 30 |
| 4.3 | DC-DC Boost Converter | 34 |
| 4.3.1 | Input capacitor..... | 35 |
| 4.3.2 | Boost inductor | 35 |
| 4.3.3 | Schottky diode rectifier | 39 |
| 4.3.4 | MOSFET | 41 |
| 4.3.5 | Output capacitor | 43 |
| 4.4 | Microelectronic control system | 44 |
| 4.5 | Pulse Width Modulator..... | 52 |
| 4.6 | Battery overcharge protection | 53 |
| 4.7 | Power conditioning system total power dissipation | 54 |
| 4.7.1 | Power conditioning system power dissipation for one TEG module..... | 55 |
| 4.7.2 | Power conditioning system power dissipation for two TEG modules connected in series..... | 57 |
| 4.7.3 | Power conditioning system power dissipation for two TEG modules connected in parallel..... | 60 |
| 5. | Experimental Results | 63 |
| 5.1 | Introduction | 63 |
| 5.2 | Experiments | 64 |
| 5.2.1 | Experimental results for one eTEG HV56..... | 64 |
| 5.2.2 | Experimental results for two eTEG HV56 connected in series | 68 |
| 5.2.3 | Experimental results for two eTEG HV56 connected in parallel..... | 71 |
| 5.2.4 | I-V and P-V curves for two TEG modules at different ΔT | 74 |
| 5.2.5 | System efficiency | 77 |

| | | |
|----------------------|--|-----------|
| 5.2.6 | Oscilloscope waveforms | 78 |
| 5.2.7 | Control circuit power consumption..... | 80 |
| 6. Conclusion | | 81 |
| References | | 84 |

1.

Introduction

1.1 Thermoelectric generators study motivation

Thermoelectric generators (TEGs) are solid state devices used for energy harvesting. TEGs can be used as energy sources in Wireless Sensor Network applications, where the network nodes demand power periodically for information collection, processing and retransmission. Utilizing TEGs to supply power to the wireless-sensor energy-storage unit, the sensors can be autonomous for significantly long time intervals.

TEGs can also be used in automobiles by utilizing the waste heat produced by the engine, in order to provide power to the vehicle electronics systems, thus reducing the fuel consumption and CO₂ emissions.

Furthermore, it has also been proposed to utilize the waste heat produced by microprocessors in order to supply power to the energy-storage unit of portable devices.

1.2 Thesis justification

Thermoelectric Generators (TEGs) are solid state devices that are used as energy sources in many applications nowadays. Thermal energy from a temperature gradient can be converted directly into electric energy, or vice versa, electric energy can be converted into thermal energy for cooling or heating demands. Due to low conversion efficiency (about 10%-15%) and high cost issues, thermoelectric generators were firstly used in special environments, such as aerospace or sub-water generating electricity applications. The

thermoelectric generators are attracting more and more attention due to the following features they exhibit:

- **reliability:** as solid-state devices, they contain no consumable parts decreasing maintenance cost,
- **environmentally friendly:** due to the lack of mechanical and moving parts they provide operation without noise or vibration,
- **scalability:** thermoelectric generators can be applied to a wide heat range and
- **dimensions:** thermoelectric generators have small footprint, profile and weight.

Therefore, thermoelectric generators have recently been used as energy sources in many applications, including automotive converting exhaust heat to electric power, wireless sensors in environments where thermal gradients exists, medical implants, thermal batteries, etc.

The power which is produced by a TEG, as is thoroughly explained in Chap. 2, is directly dependent on the temperature gradient. Since the energy conversion using TEGs is expensive and most applications demand a constant power supply, systems using TEG modules as energy source should be designed to transfer maximum power at any temperature gradient, ΔT . That means that TEG energy sources should operate at the Maximum Power Point (MPP). Fig. 1.1 shows I-V and P-V curves, as well as the MPP (shown as a circle on the P-V curve) for two different ΔT , $\Delta T=10.4$ °K and $\Delta T=16.8$ °K.

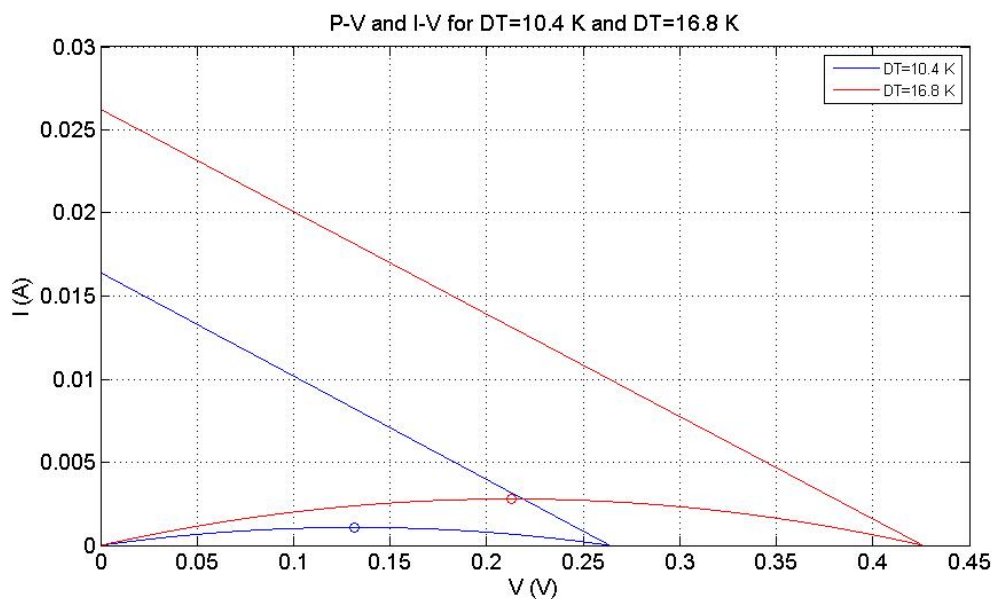


Fig. 1.1 Examples of TEG P-V, I-V curves and MPP for $\Delta T=10.4$ K and $\Delta T=16.8$ K.

To achieve maximum power transfer to the load TEGs should operate at the MPP on the P-V curve. This is achieved by using a DC-DC converter with a control circuit.

1.3 Thesis objectives

As mentioned above, maximum power transfer is of interest at any temperature gradient. Therefore, a novel Maximum Power Point Tracking technique for TEG modules is introduced in this thesis, to achieve maximum power transfer to the load. Hence, a DC-DC boost converter and a microelectronic control circuit were designed and constructed for experimental verification.

The control circuit is preprogrammed to operate on a specific curve, which is as close to the MPPs as possible, as shown in Fig. 1.2, where the MPPs are connected with the MPP curve.

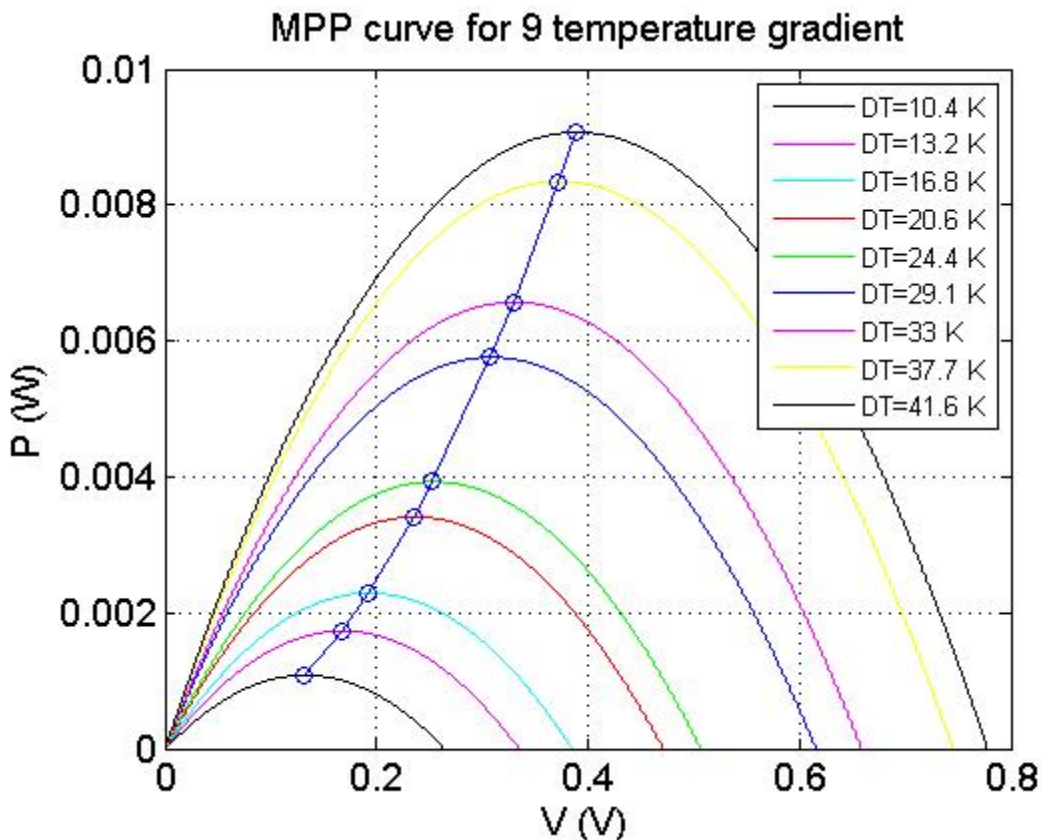


Fig. 1.2 Example of TEG MPP curve.

The block diagram of the proposed circuit is depicted in Fig. 1.3. It is a closed-loop circuit which consists of the TEG power supply, a power conditioning system, which refers to

the DC-DC boost converter, the load which is an accumulator, the loop composed of the microelectronic control circuit and finally the Pulse Width Modulator (PWM). Each part is thoroughly examined in Chap. 4.

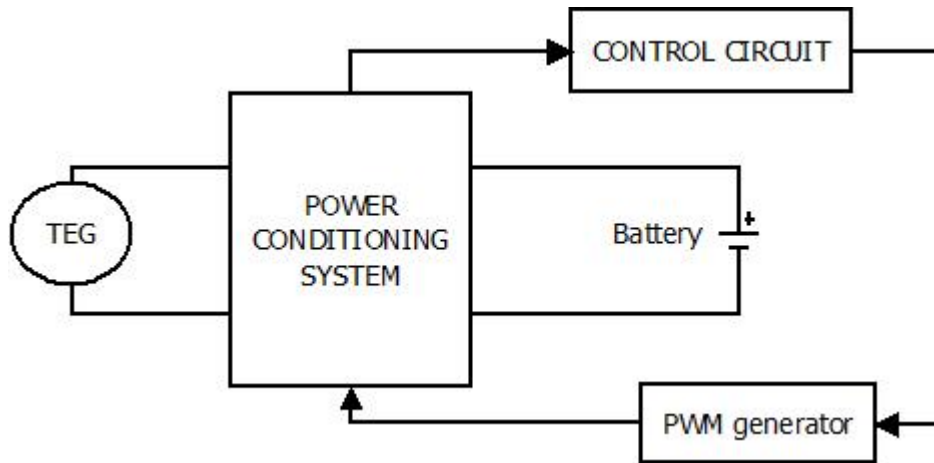


Fig. 1.3 A block diagram of proposed circuit.

1.4 Thesis outline

The present thesis mainly copes with analysis and implementation of a microelectronic system for maximum power transfer from a TEG power supply to the load. The whole work is divided in the following chapters:

- **Chapter 1: Introduction.** The main concepts of the project are analyzed, which are necessary for individuals to comprehend next chapters, and justification for utilization of TEGs as energy sources.
- **Chapter 2: TEG Model Analysis.** This chapter deals with the theoretical model of a TEG source, accompanied with simulations, useful for developing the appropriate system for a TEG application.
- **Chapter 3: Literature Review.** This chapter provides an introduction to widely used methods and explains the necessity of the present work.
- **Chapter 4: System Implementation.** This chapter copes with the procedure of the proposed system development explaining in details the selection of the individual parts.

- **Chapter 5: Experimental Results.** The experimental results are presented in this chapter and a comparison with the theoretical simulations is performed.
- **Chapter 6: Conclusion.** The major points of the thesis are summarized and a comparison of the proposed method is performed with three widely used TEG MPPT methods.

2.

TEG Model Analysis

2.1 Introduction

As mentioned in Chap.1, TEGs are solid-state devices that transform temperature gradients into electric energy. TEG operation is based on the Seebeck effect, which is the process of converting a temperature difference directly into electricity. This effect was first discovered by Thomas Johann Seebeck in 1821, who noticed a voltage difference between the edges of a metal bar when temperature gradient existed in this bar [4].

2.2 TEG basic structure and model

The TEG basic structure and phenomena taking place during TEG operation are described in details in the following sections.

2.2.1 TEG basic structure

A TEG device consists of a large number of thermocouples that are connected electrically in series and thermally in parallel. The basic structure of a single thermocouple is presented in Fig. 2.1. The structure consists of two heavily doped semiconductors the edges of which are connected to conductors, creating an electrical loop. Different temperatures T_{HJ} and T_{CJ} are applied on these junctions causing electrons and holes from n-type and p-type semiconductors, respectively, to move from hot to cold side. This movement of positive and negative charges has a result of net diffusion, producing an electric charge. Assuming the circuit is open at the cold junction, then a voltage difference $V_G = \Delta V_{pn}$ is present between the

p and n semiconductors due to the Seebeck effect. Based on the Seebeck effect, thermoelectric generators have the advantages of no moving parts, silent operation and being very reliable.

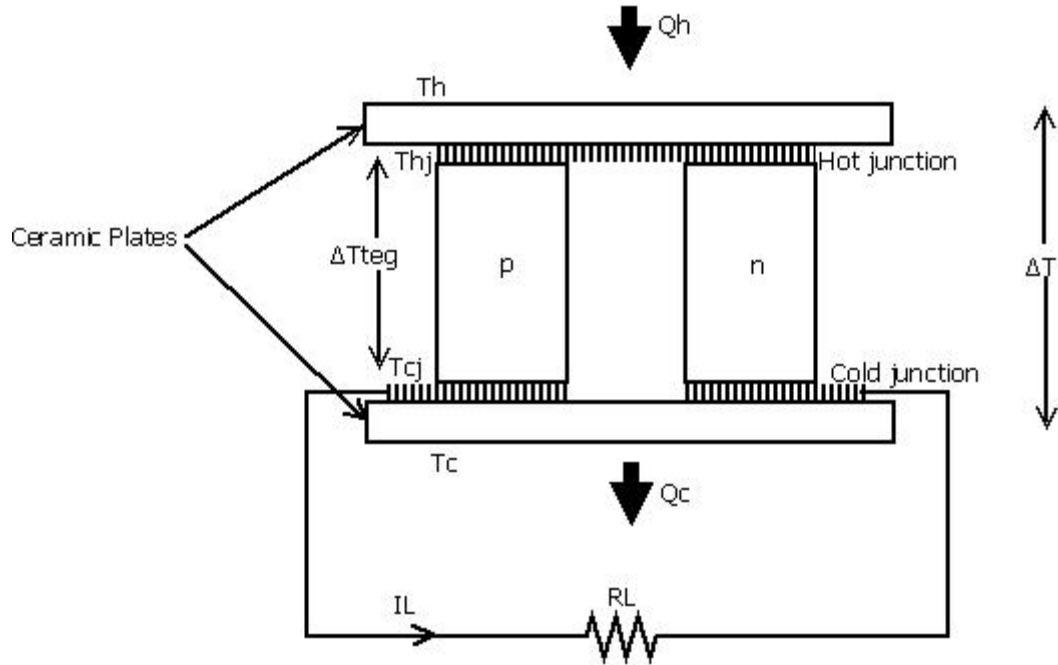


Fig. 2.1 Basic structure of TEG [2].

The voltage V_G which is produced due to the Seebeck effect is proportional to the temperature difference, according to the following equation:

$$V_G = \Delta V_{pn} = \alpha_{pn} (T_{HJ} - T_{CJ}) \quad (2.1)$$

where α_{pn} is the Seebeck coefficient between the p and n semiconductors.

The p and n semiconductors have positive and negative Seebeck coefficient, respectively. Thus $\alpha_{pn} = \alpha_p - \alpha_n$ is positive. The reverse is the Peltier effect, which is present when current I flows in semiconductors through the loop. In this case, the heat is absorbed by a junction and is transferred to the other junction causing a variation in its temperature. The temperature transfer rate to junction X due to Peltier effect is proportional to the current I according to the following equation:

$$Q_X = \alpha_{pn} T_X I_L \quad (2.2)$$

where T_X is the absolute temperature of the junction.

Assuming that the current I flowing through semiconductor p has a positive sign from hot junction to cold junction, then Q_H is considered positive for an incoming flow of heat to the thermoelectric generator and Q_C is considered positive for an outgoing flow of heat.

The thermocouples are interposed between electrically isolated and thermally conductible ceramic plates with finite thermal conduction K . The thermal energy is transferred from a thermal source that is at T_H temperature to the hot junction which in turn is at T_{HJ} temperature through the ceramic plate. On the other hand, the cold junction that is at T_{CJ} temperature emits heat to the environment through the ceramic plate which is at a lower temperature, T_C .

For theoretical analysis purposes it is assumed that junctions have insignificant thermal and electrical contact resistance. Also, it is assumed that the Seebeck coefficient α , electrical resistance ρ and thermal conductivity λ of the semiconductors are independent to temperature.

Assuming a load, R_L , is connected to the thermocouple, then a current I_L that flows through it is given by the following equation:

$$I_L = \frac{V_G}{R_{in} + R_L} = \frac{\alpha_{pn}(T_{HJ} - T_{CJ})}{R_{in} + R_L} \quad (2.3)$$

where R_{in} is the internal electrical resistance of the thermocouple and it is given by the following equation:

$$R_{in} = \frac{2\rho h}{A_{leg}} \quad (2.4)$$

where h is the height and A_{leg} is the cross-sectional area of a single thermo-element.

The heat transfer rate from the thermal source to the hot junction, through the top ceramic plate and from the cold junction to the environment, through the bottom ceramic plate as a result of thermal conductance, as seen in Fig. 2.1 above, are given by the following equations:

$$Q_H = (T_H - T_{HJ})K \quad (2.5)$$

$$Q_C = (T_{CJ} - T_C)K \quad (2.6)$$

The heat exchange rate on hot and cold junctions is the summation of Peltier effect, thermal conductance through the thermocouple according to Fourier's law and the Joule heat loss due to current flow. Thus, Q_H and Q_C can be expressed by the following equations:

$$Q_H = \alpha_{pn} T_{HJ} I_L + K_{in} (T_{HJ} - T_{CJ}) - \frac{1}{2} I_L^2 R_{in} \quad (2.7)$$

$$Q_C = \alpha_{pn} T_{CJ} I_L + K_{in} (T_{HJ} - T_{CJ}) + \frac{1}{2} I_L^2 R_{in} \quad (2.8)$$

where K_{in} is the internal thermal conductance of the thermo-elements and it is given by the following equation:

$$K_{in} = \frac{2\lambda A_{leg}}{h} \quad (2.9)$$

2.2.2 TEG equivalent circuit

The thermal conductance according to Fourier's law and the Joule heat loss are irreversible procedures that reduce the overall efficiency of energy conversion of the thermoelectric generator. The following figure shows an equivalent thermocouple model where thermal coefficients Q , T , K are represented by current, voltage and conductance, respectively.

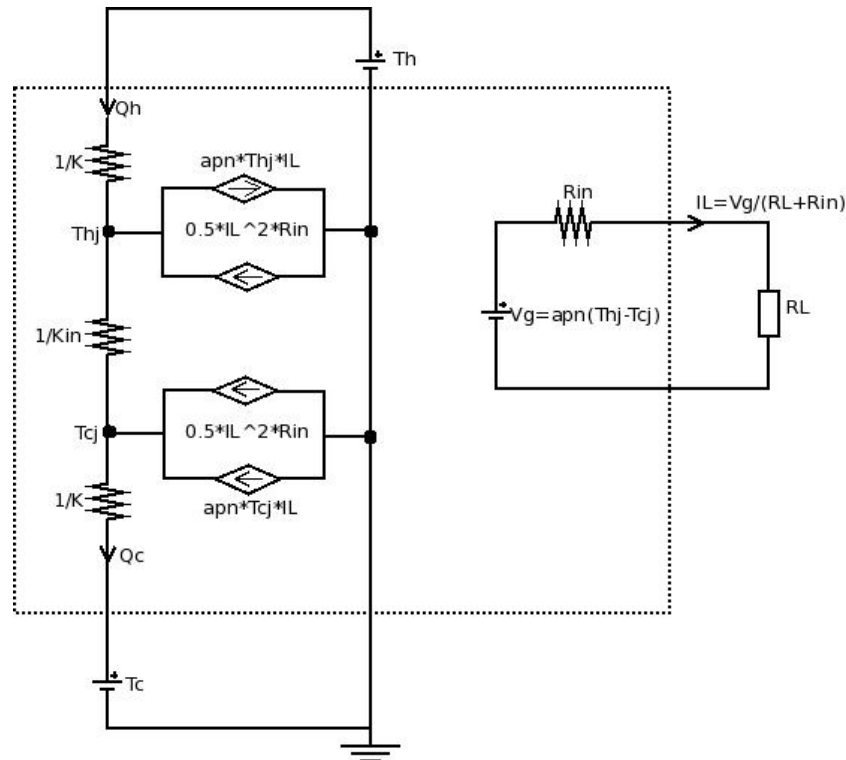


Fig. 2.2 The equivalent electric circuit of a TEG device [2].

The bottom thermal port represents the cold side of the thermocouple in ambient temperature T_C , whereas the top thermal port represents the hot source which is at temperature T_H . The current sources, which are described by equations (2.7) and (2.8), represent the Joule and Peltier effects contribution to the heat transfer rate to hot and cold junctions. The right loop represents the electrical output port of the thermocouple, where V_G is the open-circuit voltage given by equation (2.1) and R_{in} is the internal electrical resistance given by equation (2.4).

2.2.3 Electro-thermal interactions during operation

To sum up, assuming that a temperature gradient is applied across the hot and cold junctions of a thermoelectric generator, then due to the Seebeck effect, a voltage V_G that is proportional to the temperature difference is produced according to equation (2.1). In case that a load R_L is connected to the thermoelectric generator, thus creating a loop, then a current I_L , which is proportional to the voltage V_G , flows in that loop. Due to the current flow, a Joule heat occurs as a result of the power dissipation in the internal resistance R_{in} of the thermocouple. Joule heat, in turn, perturbs the temperature gradient and therefore influences the Seebeck voltage. Then the whole procedure restarts as seen in the figure below [5].

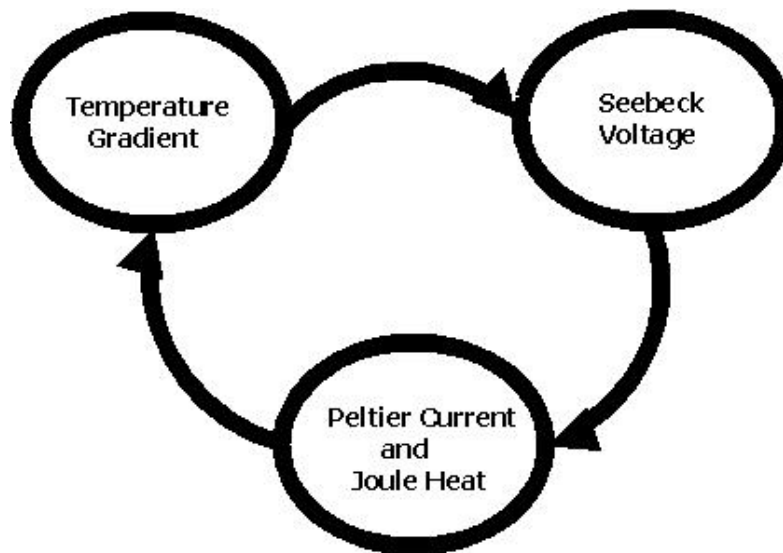


Fig. 2.3 Cycle of effects that take place[5].

2.3 TEG model calculation

Equations (2.5)-(2.8) comprise the model, which is used to simulate the operation of thermoelectric generators.

$$Q_H = (T_H - T_{HJ})K \quad (2.5)$$

$$Q_C = (T_{CJ} - T_C)K \quad (2.6)$$

$$Q_H = \alpha_{pn} T_{HJ} I_L + K_{in} (T_{HJ} - T_{CJ}) - 0,5 I_L^2 R_{in} \quad (2.7)$$

$$Q_C = \alpha_{pn} T_{CJ} I_L + K_{in} (T_{HJ} - T_{CJ}) + 0,5 I_L^2 R_{in} \quad (2.8)$$

Considering that (2.5)=(2.7) and (2.6)=(2.8), it is possible to calculate $(T_H - T_{HJ})$ and $(T_C - T_{CJ})$ respectively, as follows:

$$(2.5) = (2.7) \Rightarrow (T_H - T_{HJ})K = \alpha_{pn} T_{HJ} I_L + K_{in} (T_{HJ} - T_{CJ}) - 0,5 I_L^2 R_{in} \Rightarrow$$

$$T_H - T_{HJ} = \frac{\alpha_{pn} T_{HJ} I_L + K_{in} (T_{HJ} - T_{CJ}) - 0,5 I_L^2 R_{in}}{K} \quad (2.9)$$

and:

$$(2.6) = (2.8) \Rightarrow (T_{CJ} - T_C)K = \alpha_{pn} T_{CJ} I_L + K_{in} (T_{HJ} - T_{CJ}) + 0,5 I_L^2 R_{in} \Rightarrow$$

$$T_{CJ} - T_C = \frac{\alpha_{pn} T_{CJ} I_L + K_{in} (T_{HJ} - T_{CJ}) + 0,5 I_L^2 R_{in}}{K} \quad (2.10)$$

Comparing (2.9) and (2.10) it is possible to calculate $T_{HJ} - T_{CJ}$:

$$(9) + (10) \Rightarrow T_H - T_{HJ} + T_{CJ} - T_C = \frac{(T_{HJ} + T_{CJ})\alpha_{pn} I_L + 2K_{in} (T_{HJ} - T_{CJ})}{K} \Rightarrow$$

$$T_{HJ} - T_{CJ} = -\frac{2K_{in} (T_{HJ} - T_{CJ})}{K} - \frac{(T_{HJ} + T_{CJ})\alpha_{pn} I_L}{K} - T_C + T_H \quad (2.11)$$

Subtracting (2.10) from (2.9) it is possible to calculate $T_{HJ} + T_{CJ}$, as follows:

$$(9) - (10) \Rightarrow T_H - T_{HJ} - T_{CJ} + T_C =$$

$$\frac{\alpha_{pn} T_{HJ} I_L + K_{in} (T_{HJ} - T_{CJ}) - 0,5 I_L^2 R_{in}}{K} - \frac{\alpha_{pn} T_{CJ} I_L + K_{in} (T_{HJ} - T_{CJ}) + 0,5 I_L^2 R_{in}}{K} \Rightarrow$$

$$T_{HJ} + T_{CJ} = \frac{-a_{pn}(T_{HJ} - T_{CJ})I_L + I_L^2 R_{in}}{K} + T_H + T_C \quad (2.12)$$

Substituting (2.12) to (2.11) and setting $\Delta T_{TEG} = T_{HJ} - T_{CJ}$ and $\Delta T = T_H - T_C$, it results that:

$$(11) \stackrel{(12)}{\implies} T_{HJ} - T_{CJ} + \frac{2K_{in}(T_{HJ} - T_{CJ})}{K} + \frac{\left(\frac{-a_{pn}(T_{HJ} - T_{CJ})I_L + I_L^2 R_{in}}{K} + T_H + T_C\right) a_{pn} I_L}{K} =$$

$$-T_C + T_H \Rightarrow \Delta T_{TEG} = \frac{-a_{pn} I_L (I_L^2 R_{in} + K(T_H + T_C)) + K^2 \Delta T}{K^2 + 2K_{in}K - a_{pn}^2 I_L^2} \quad (2.13)$$

Finally using (2.9) and (2.10) it is possible to calculate T_{HJ} and T_{CJ} respectively:

$$(9) \stackrel{T_{CJ} = T_{HJ} - \Delta T_{TEG}}{\implies} T_H - T_{HJ} = \frac{a_{pn} T_{HJ} I_L + K_{in}(T_{HJ} - T_{HJ} + \Delta T_{TEG}) - 0,5 I_L^2 R_{in}}{K} \Rightarrow$$

$$T_{HJ} = \frac{K T_H - K_{in} \Delta T_{TEG} + 0,5 I_L^2 R_{in}}{a_{pn} I_L + K} \quad (2.14)$$

Furthermore:

$$(10) \stackrel{T_{HJ} = T_{CJ} + \Delta T_{TEG}}{\implies} T_{CJ} - T_C = \frac{a_{pn} T_{CJ} I_L + K_{in}(T_{CJ} + \Delta T_{TEG} - T_{CJ}) + 0,5 I_L^2 R_{in}}{K} \Rightarrow$$

$$T_{CJ} = \frac{K T_C + K_{in} \Delta T_{TEG} + 0,5 I_L^2 R_{in}}{K - a_{pn} I_L} \quad (2.15)$$

The output power of the thermoelectric generator is given by the following equation:

$$P_L = I_L V_L = I_L (a_{pn} \Delta T_{TEG} - I_L R_{in}) \quad (2.16)$$

Substituting equation (2.3) to (2.16), P_L can be written as a function of ΔT_{TEG} :

$$(2.16) \stackrel{(2.3)}{\implies} P_L = \frac{\alpha_{pn} \Delta T_{TEG}}{R_{in} + R_L} \left(a_{pn} \Delta T_{TEG} - \frac{\alpha_{pn} \Delta T_{TEG}}{R_{in} + R_L} R_{in} \right) = \frac{\alpha_{pn}^2 \Delta T_{TEG}^2}{R_{in} + R_L} \left(1 - \frac{R_{in}}{R_{in} + R_L} \right)$$

$$= \frac{\alpha_{pn}^2 \Delta T_{TEG}^2}{R_{in} + R_L} \frac{R_L}{R_{in} + R_L} = \frac{\alpha_{pn}^2 \Delta T_{TEG}^2 R_L}{(R_{in} + R_L)^2} \quad (2.17)$$

The maximum power transfer can be achieved in matched load conditions. This occurs if $R_{in} = R_L$. In this case the transferred power can be expressed by the following equation:

$$P_{Lmax} = \frac{\alpha_{pn}^2 \Delta T_{TEG}^2}{4R_L} \quad (2.18)$$

The output power P_L depends on the temperature difference between the hot and cold junctions, ΔT_{TEG} . However, ΔT_{TEG} is always less than ΔT due to the finite value of the thermal conductance, K , of the ceramic plates. Thus, the thermal conductance K should be as high as possible, in order to maximize the limited power produced. In addition, ΔT_{TEG} is dependent on the value of the load, R_L . The lower the value of R_L , the higher the current I_L which flows in the loop. Higher current causes the hot junction to become cooler and the cold junction to become hotter due to the Peltier effect, as described above. As a result, ΔT_{TEG} becomes lower causing the output power to drop.

2.4 Simulations based on theoretical model

Using equations (2.1), (2.14), (2.15) for $0 \leq I_L \leq I_{sc}$ and various values of ΔT , a model has been developed in Matlab for the available TEG device eTEG HV56. The model is applied to 3 different types of connection:

- One eTEG HV56 module,
- Two eTEG HV56 modules connected in series and
- Two eTEG HV56 modules connected in parallel.

The method of MMP to be used is based on the results of the simulations. Then, the simulations are compared with the experimental results.

2.4.1 Simulation results for one eTEG HV56

The following figures illustrate the simulation results for one eTEG HV56 device. Figs. 2.4 through 2.7 depict the characteristics of I - V , P - V , T_{cj} - V and T_{hj} - V respectively for one TEG for $\Delta T=10.4^\circ K, 13.2^\circ K, 16.8^\circ K, 20.6^\circ K, 24.4^\circ K, 29.1^\circ K, 33^\circ K, 37.7^\circ K$ and $41.6^\circ K$.

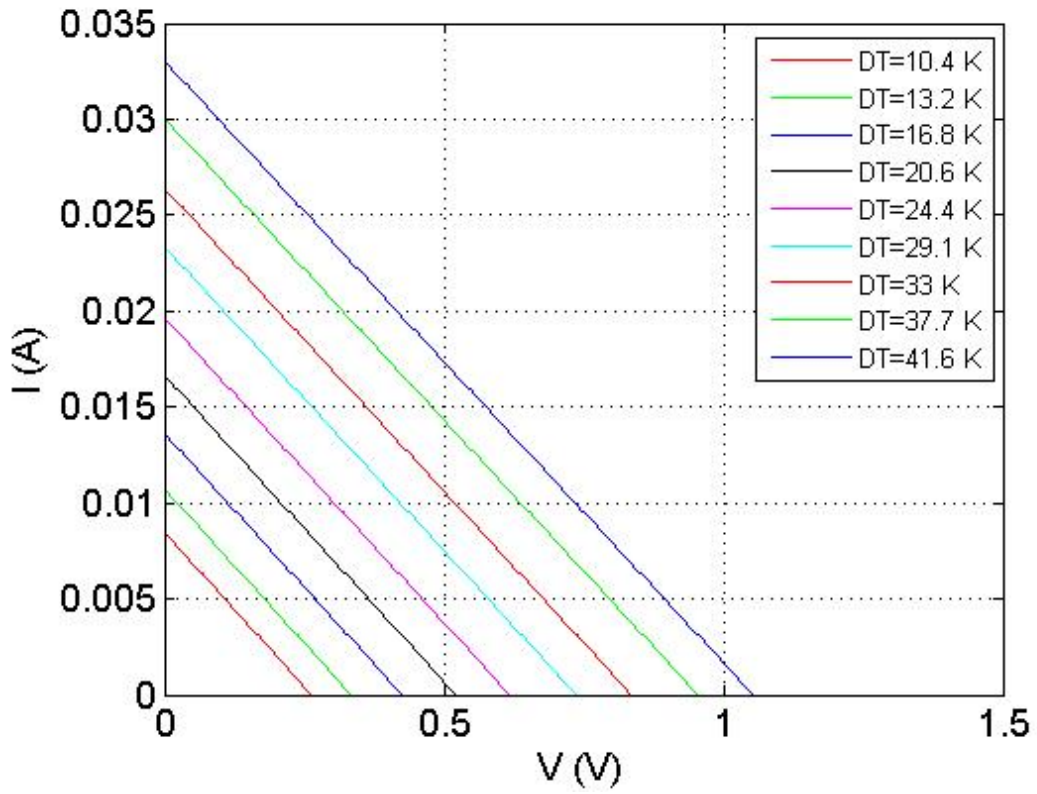


Fig. 2.4 I-V characteristics of the TEG.

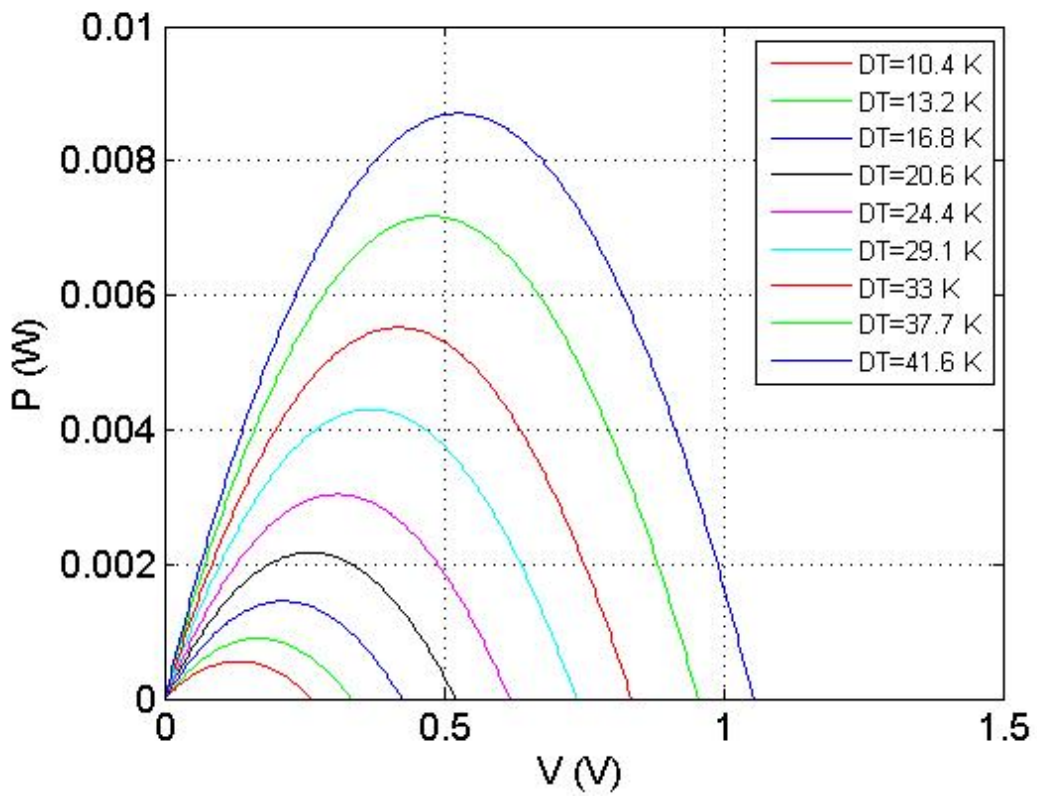


Fig. 2.5 P-V characteristics of the TEG.

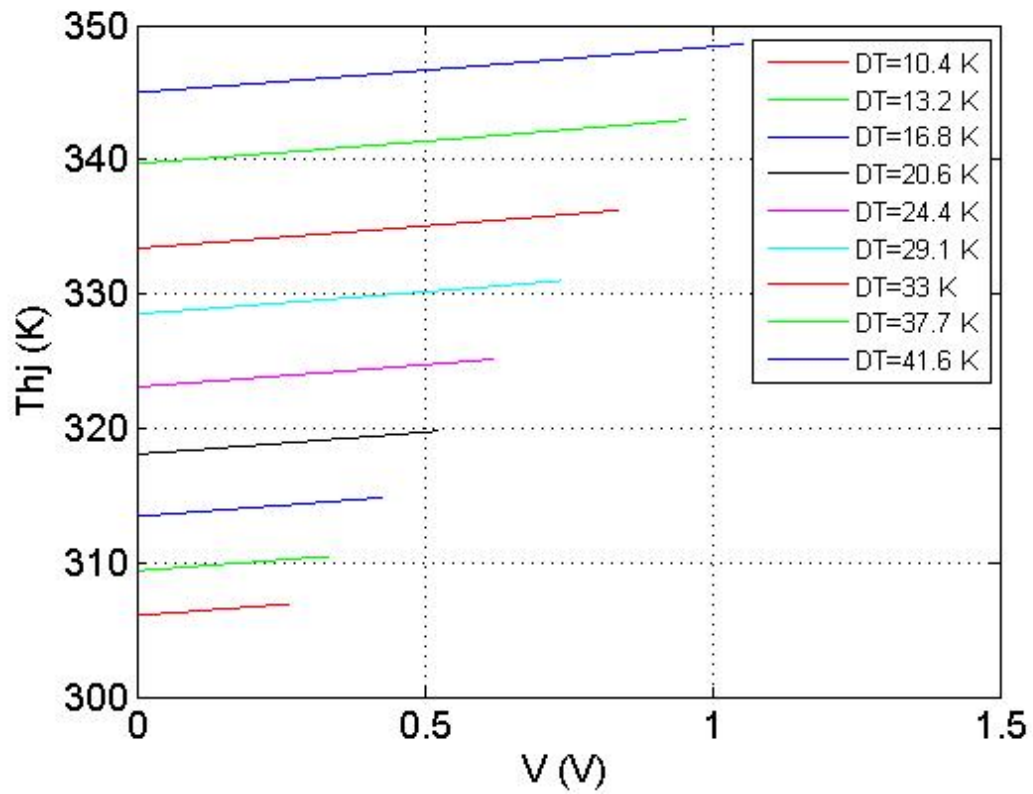


Fig. 2.6 T_{hj} - V characteristics of the TEG.

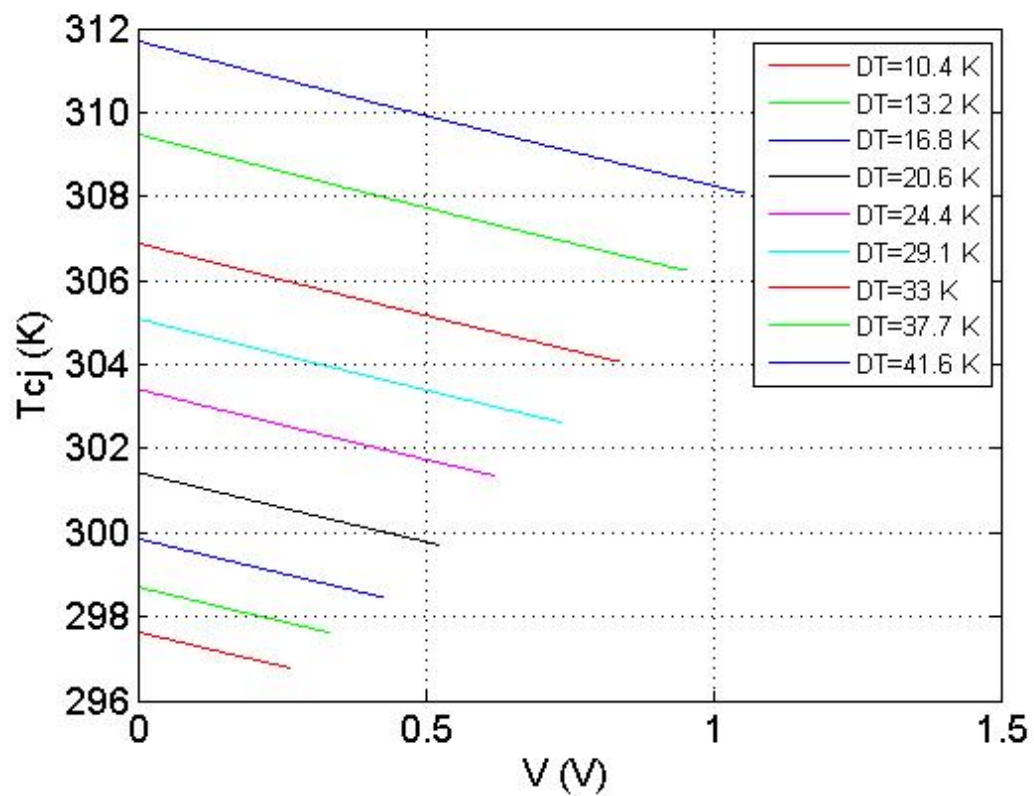


Fig. 2.7 T_{cj} - V characteristics of the TEG.

2.4.2 Simulation results for two eTEG HV56 connected in series

The following figures illustrate the simulation results for two eTEG HV56 devices connected in series. Figs. 2.8 through 2.11 represent the characteristics of I - V , P - V , T_{cj} - V and T_{hj} - V , respectively, for two TEG modules connected in series for $\Delta T=9.6^\circ\text{K}$, 13.3°K , 16.9°K , 20.2°K , 24.3°K , 28.3°K , 32.3°K , 36°K and 40.3°K .

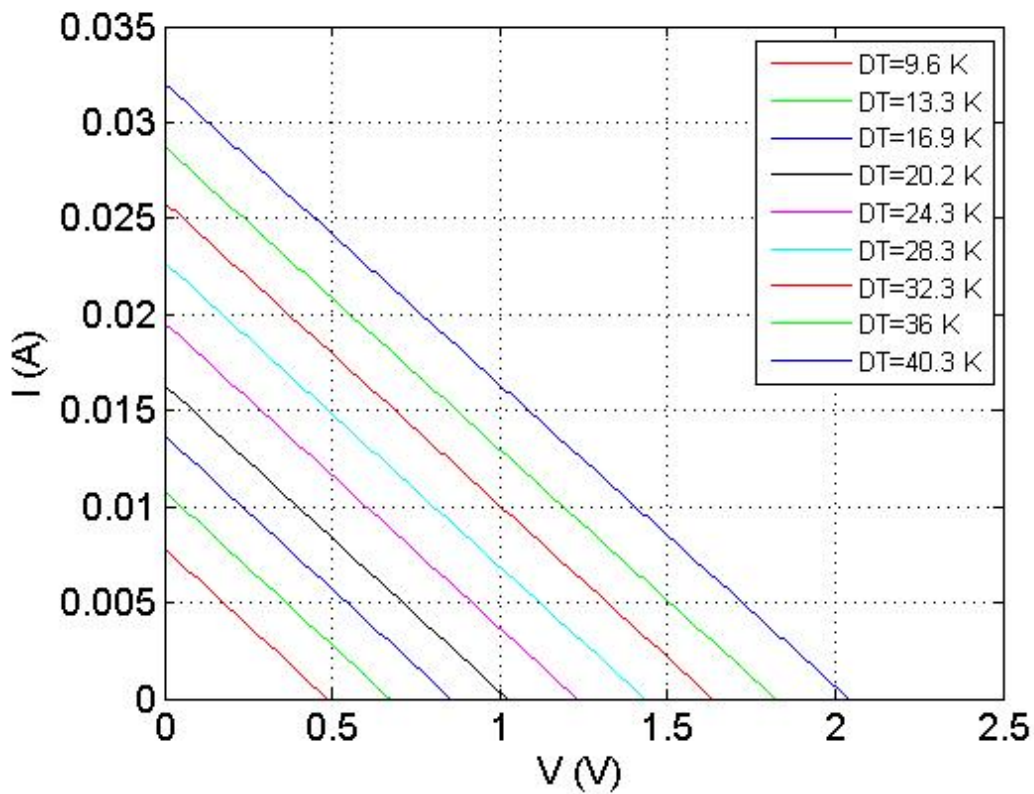


Fig. 2.8 I-V characteristics of two TEG modules connected in series.

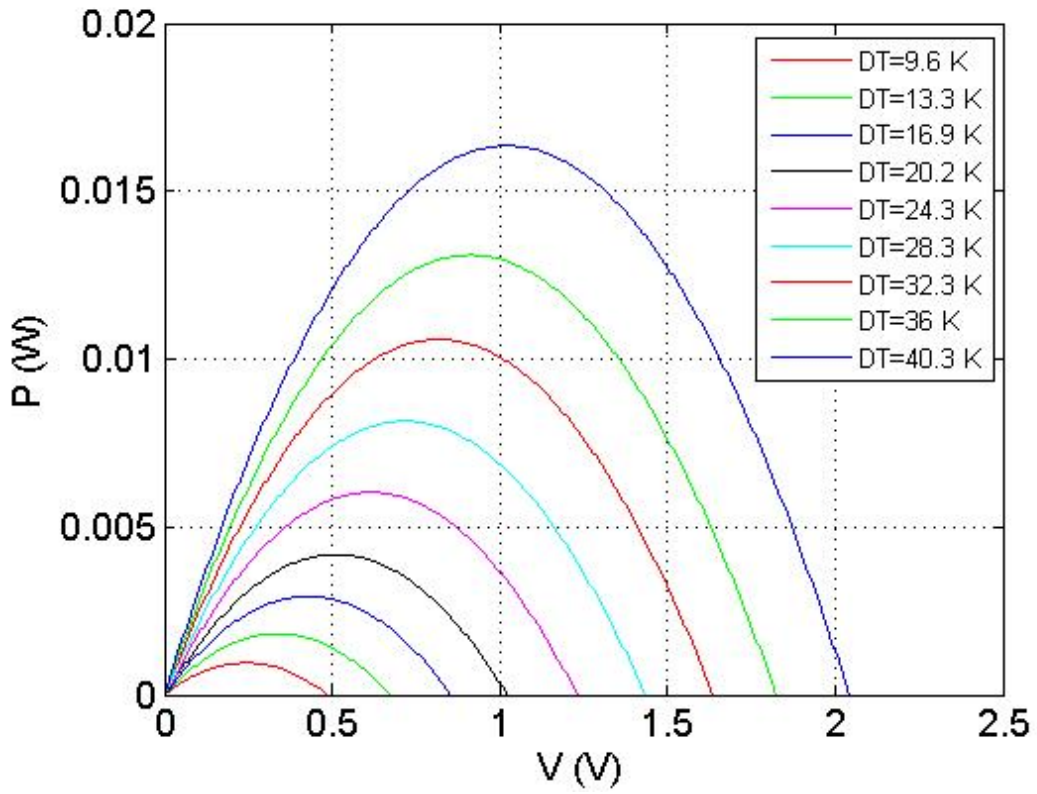


Fig. 2.9 P-V characteristics of two TEG modules connected in series.

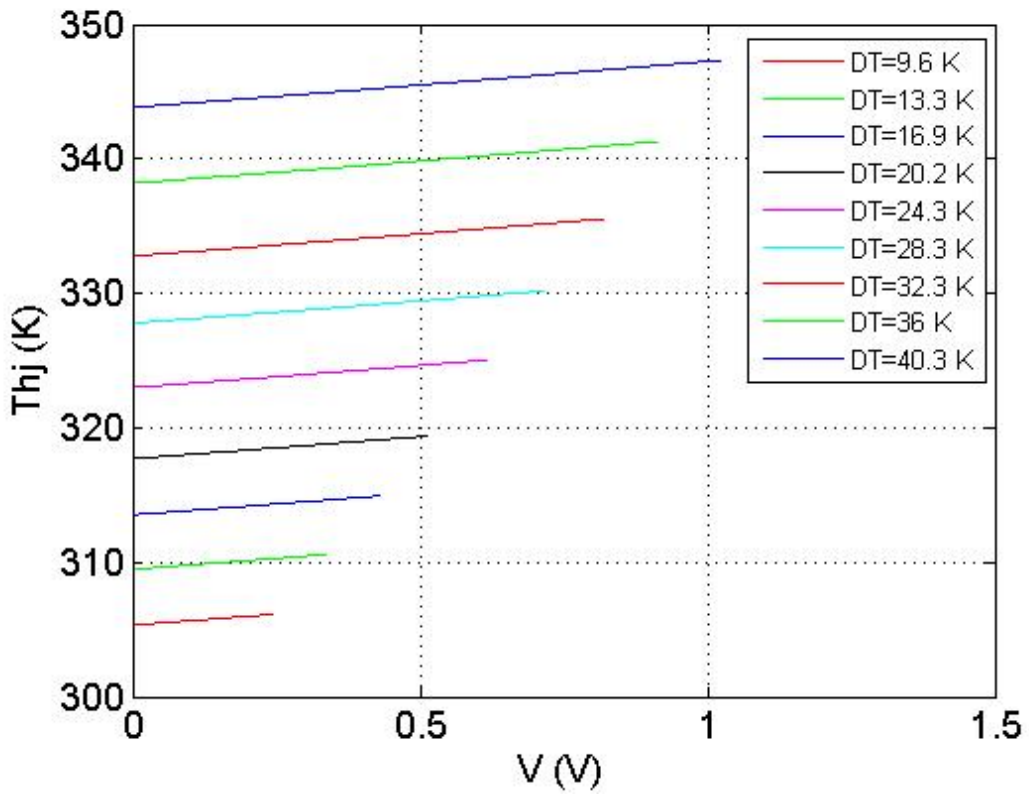


Fig. 2.10 T_{hj} -V characteristics of two TEG modules connected in series.

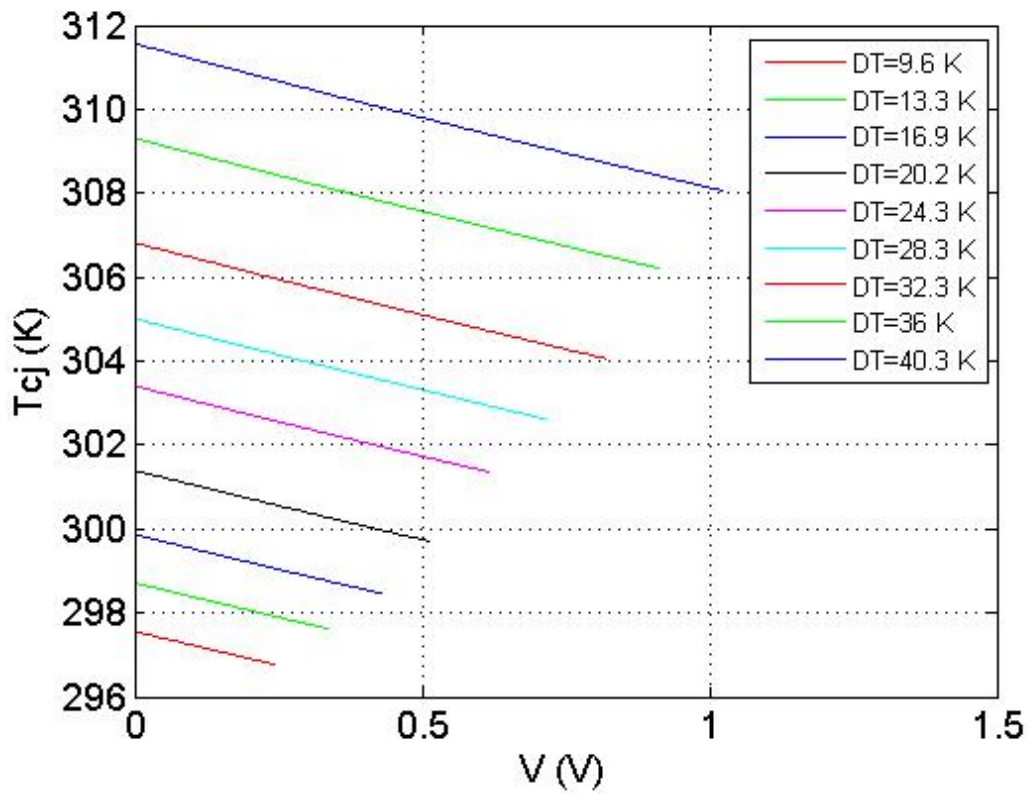


Fig. 2.11 T_{cj} - V characteristics of two TEG modules connected in series.

2.4.3 Simulation results for two eTEG HV56 connected in parallel

The following figures illustrate the simulation results for two eTEG HV56 devices connected in parallel. Figs. 2.12 through 2.15 represent the characteristics of I - V , P - V , T_{cj} - V and T_{hj} - V , respectively, for two TEG modules connected in parallel for $\Delta T=10.4$ °K, 13.2 °K, 16.6 °K, 20.4 °K, 24.4 °K, 28 °K, 32.3 °K, 36.2 °K and 40 °K.

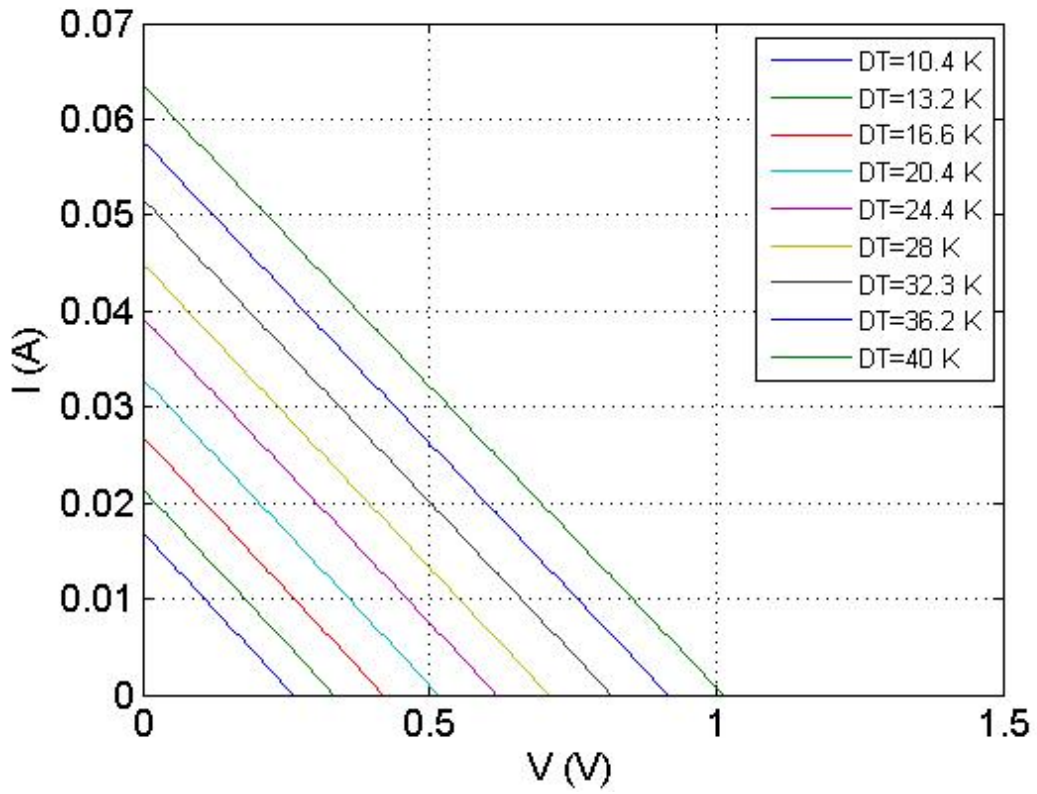


Fig. 2.12 I-V characteristics of two TEG modules connected in parallel.

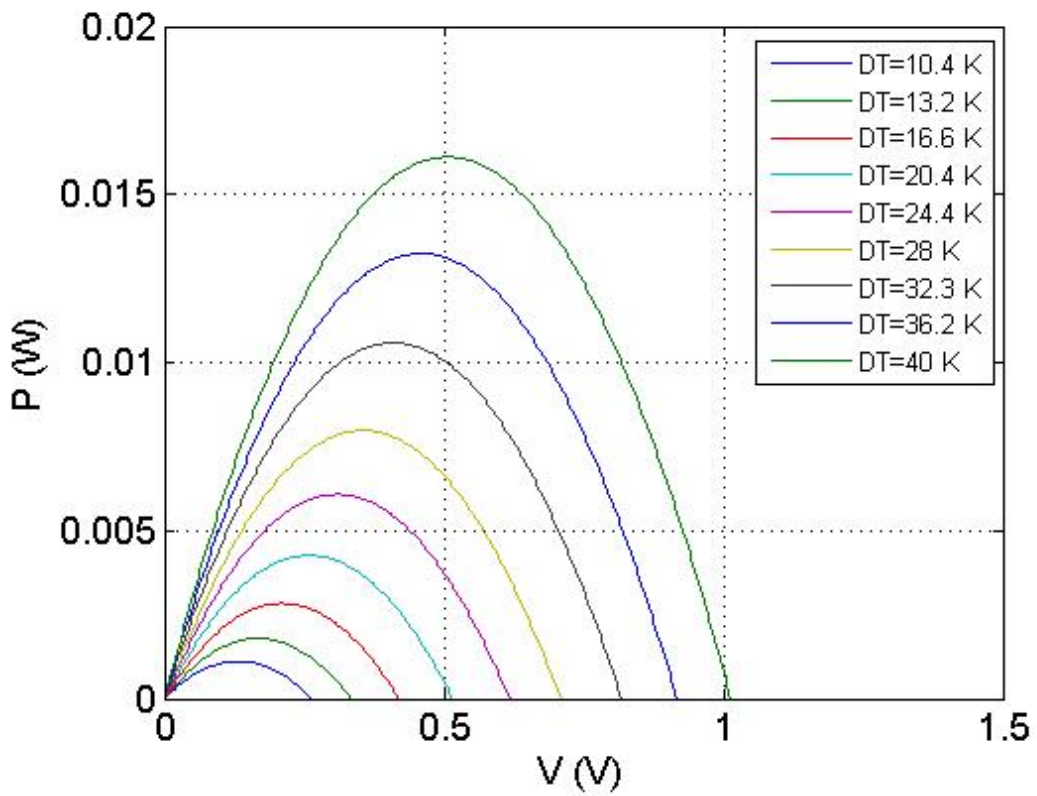


Fig. 2.13 P-V characteristics of two TEG modules connected in parallel.

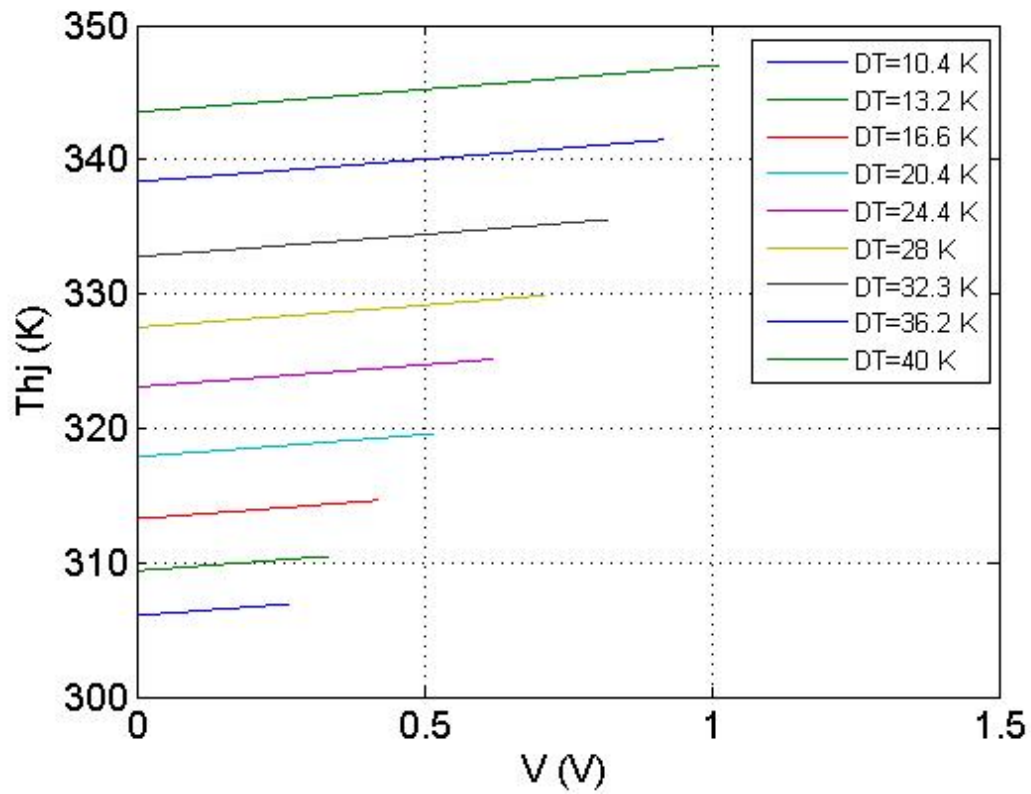


Fig. 2.14 T_{hj} - V characteristics of two TEG modules connected in parallel.

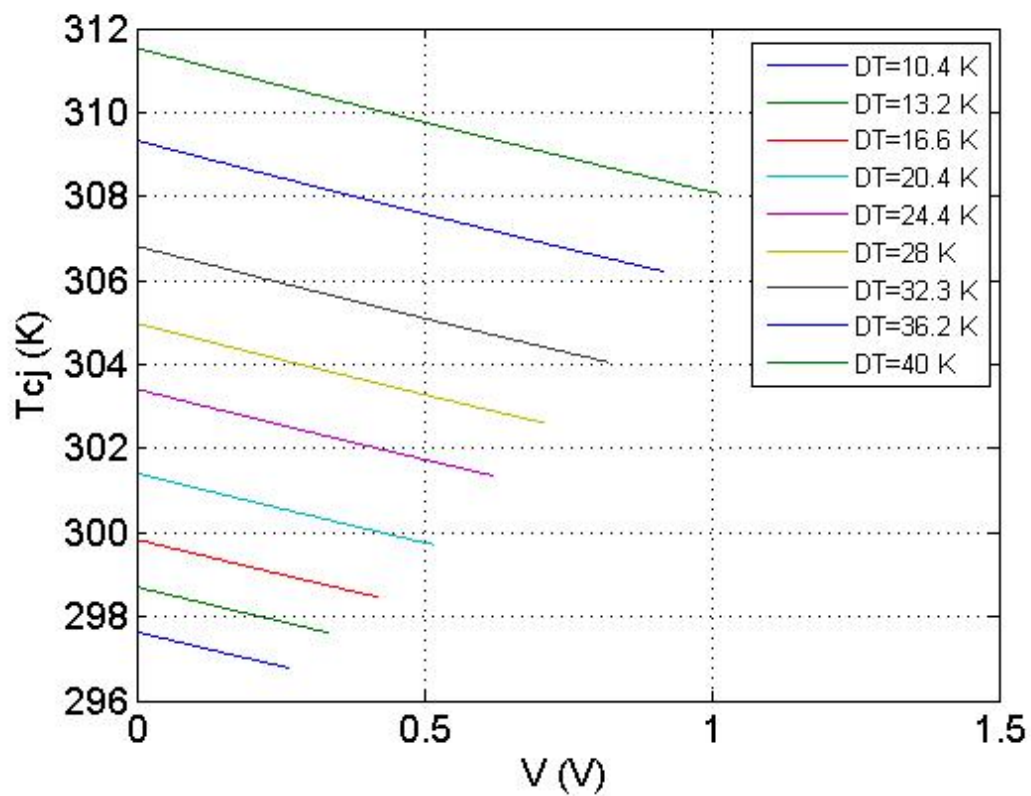


Fig. 2.15 T_{cj} - V characteristics of two TEG modules connected in parallel.

3.

Past-Proposed MPPT Methods for TEGS

3.1 Significance of MPPT

As mentioned in Chap. 1, maximum power transfer to the load of a circuit is of major interest and is achieved using a Maximum Power Point Tracking (MPPT) technique. Fig. 3.1 illustrates the MPPT principle. Purple dotted line and letters show the direction followed by the operating point.

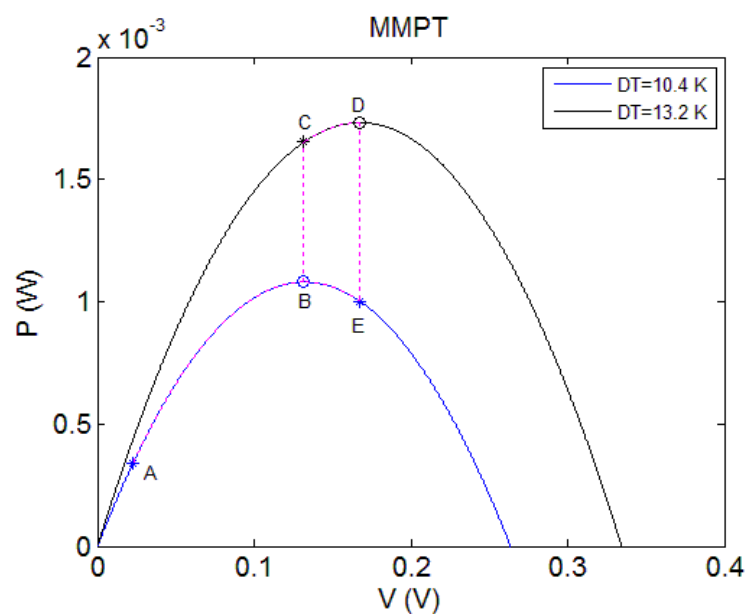


Fig. 3.1 MPPT operation in different temperature gradient conditions.

It is assumed that a temperature gradient equal to $\Delta T=10.4\text{ }^{\circ}K$ is developed across the TEG. Thus, the MPPT process starts operation from point *A* producing a PWM signal with a certain duty cycle value of the power converter shown in Fig. 1.3. As mentioned before, it is of major interest that the TEG output power is increased, therefore the duty cycle must be increased to reach the maximum output power for this temperature gradient, which is at point *B*. In case that the temperature gradient increases to $\Delta T=13.2\text{ }^{\circ}K$, then the Power – Voltage curve of the TEG device changes and due to the duty cycle remaining at the same value, then the new operating point shall be point *C*. Despite the fact that the output power has been increased, due to the increase in the temperature gradient, the maximum power point of the new curve is not reached. Therefore, duty cycle must be increased again to reach point *D*, which is the MPP for the $\Delta T=13.2\text{ }^{\circ}K$ curve. Assuming the temperature gradient drops again to $\Delta T=10.4\text{ }^{\circ}K$, then the new operating point is point *E*, which is not the maximum power point on the Power - Voltage curve for $\Delta T=10.4\text{ }^{\circ}K$. Thus, the duty cycle must be decreased to reach point *B*.

3.2 MPPT techniques

Many MPP tracking techniques have been developed and applied to systems employing TEG modules as energy sources in order to increase the output power produced by the TEG modules. The most suitable method for each application can be selected according to specific aspects, such as cost, effectiveness, implementation hardware, complexity and convergence speed. Some of the above aspects can be more important for some applications and less important for others, e.g., in applications with slow rate of temperature gradient, convergence speed is of minor importance. The Perturb & observe (P&O), Incremental Conductance (INC) and fractional open-circuit voltage / short-circuit current MMPT techniques are described in the following paragraphs.

3.2.1 Perturb and Observe (P&O)

P&O algorithm is the most common MPPT method due to its simplicity [3]. Many different variations of the P&O algorithm have been developed. The P&O algorithm is often referred to as hill-climbing method, as its operation involves the displacement of the operation point gradually towards the top of the Power - Voltage curve. The P&O algorithm operation is based on the method of disturbance and observation of the operation point. Fig. 3.2 shows the flowchart of the algorithm. P&O algorithm reaches the MPP by measuring the output voltage

and current of an energy source, calculating the output power and stepping the operating voltage towards a specific direction. After the perturb operation, the new output current and voltage are measured again and the current value of the output power is re-calculated and compared to the previous one.

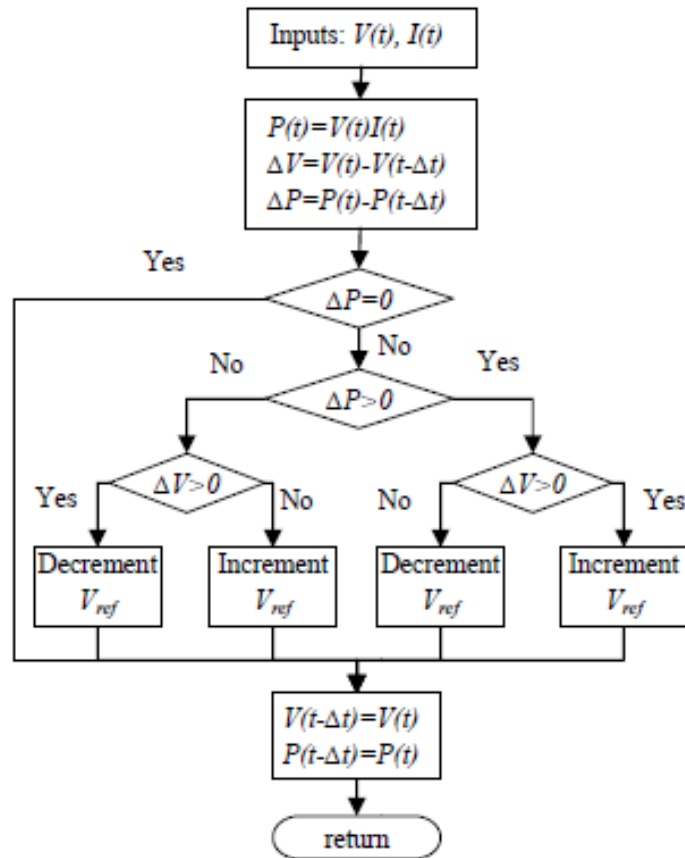


Fig. 3.2 P&O algorithm flowchart [3].

After the output power comparison, the previous and current values of the output voltage are compared. In case that the current value of the output power is less than the previous value and the current value of the output voltage is greater (less) than the previous one, that means the operating point is on the right (left) side of the MPP and the direction of the subsequent perturbation should be reversed. In case that the current value of the output power is greater than the previous value and the current value of the output voltage is greater (less) than the previous one, that means the operating point is on the left (right) side of the MPP and the direction of the subsequent perturbation should remain the same. The whole operation is summarized in Table 1.

| ΔP | ΔV | Perturbation |
|------------|------------|---------------------|
| >0 | >0 | Same |
| >0 | <0 | Same |
| <0 | >0 | Reversed |
| <0 | <0 | Reversed |

As illustrated in Fig. 3.2, the P&O algorithm has no way of establishing when the MPP has been reached. Instead, the system will oscillate around the MPP resulting in a decrease of the output power. The magnitude of the oscillation depends on the perturbation step size. By reducing the perturbation step size, the operating point oscillates closer to the MPP, thus obtaining more output power. However, as a result of reducing the step size, more steps and consequently more time is required for the system to reach steady-state operation. Thus, a variation of the P&O algorithm using variable step size has also been proposed [3]. In the beginning of the tracking process the step size is large enough to allow quick convergence between the operating point and the MPP. As soon as the operating point is close to the MPP, the step size is reduced to minimize the steady-state error.

3.2.2 Incremental Conductance (INC)

The INC method requires more complex computations than the P&O method, but has the ability to track changes in the output power more rapidly. The INC MPPT algorithm is considered to be another hill-climbing method of reaching the MPP.

As seen in Fig. 3.3, the slope of the P-V curve of a TEG is:

- positive on the left of the MPP,
- negative on the right of the MPP and
- zero at the MPP.

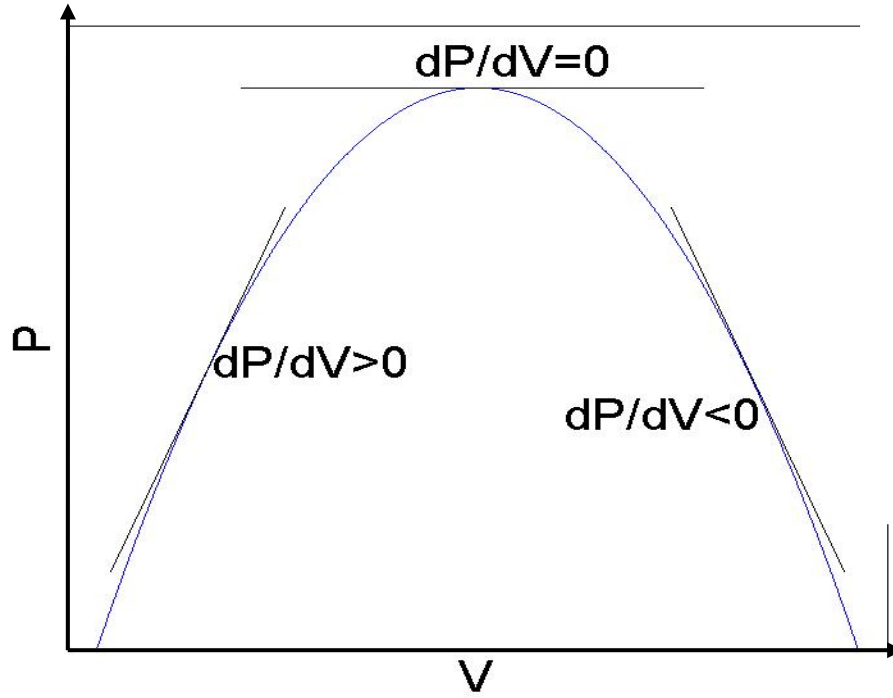


Fig. 3.3 *P-V curve slopes.*

The Incremental Conductance method utilizes the above property for tracking the MPP. Thus, the following equations are used to control the tracking process:

$$- \quad \frac{dP}{dV} > 0 \Rightarrow V_{op} < V_{MPP} \quad (3.1a)$$

$$- \quad \frac{dP}{dV} = 0 \Rightarrow V_{op} = V_{MPP} \quad (3.1b)$$

$$- \quad \frac{dP}{dV} < 0 \Rightarrow V_{op} > V_{MPP} \quad (3.1c)$$

where V_{op} is the voltage at the current operating point.

Furthermore, since $P = VI$ the above derivatives can be re-written as follows:

$$\frac{dP}{dV} = \frac{dVI}{dV} = \frac{dV}{dV}I + \frac{dI}{dV}V = I + \frac{\Delta I}{\Delta V}V \quad (3.2)$$

Using (3.2), inequalities (3.1) can be written as follows:

$$(3.1a) \stackrel{(3.2)}{\implies} \frac{dP}{dV} > 0 \Rightarrow I + \frac{\Delta I}{\Delta V}V > 0 \Rightarrow \frac{\Delta I}{\Delta V} > -\frac{I}{V} \text{ then } V_{op} < V_{MPP} \quad (3.3a)$$

$$(3.1b) \stackrel{(3.2)}{\implies} \frac{dP}{dV} = 0 \Rightarrow I + \frac{\Delta I}{\Delta V}V = 0 \Rightarrow \frac{\Delta I}{\Delta V} = -\frac{I}{V} \text{ then } V_{op} = V_{MPP} \quad (3.3b)$$

$$(3.1c) \stackrel{(3.2)}{\implies} \frac{dP}{dV} < 0 \implies I + \frac{\Delta I}{\Delta V} V < 0 \implies \frac{\Delta I}{\Delta V} < -\frac{I}{V} \text{ then } V_{op} > V_{MPP} \quad (3.3c)$$

Using the above equations, the MPP can be reached by comparing the incremental conductance, $\frac{\Delta I}{\Delta V}$, with the negative of the instantaneous conductance, i.e. $-\frac{I}{V}$ [3]. The MPP is reached as soon as the incremental conductance equals the instantaneous conductance. At this point the MPPT operation is suspended until a new disturbance in the output power of the source is detected by the MPPT system. Fig 3.4 depicts a flowchart of the INC algorithm.

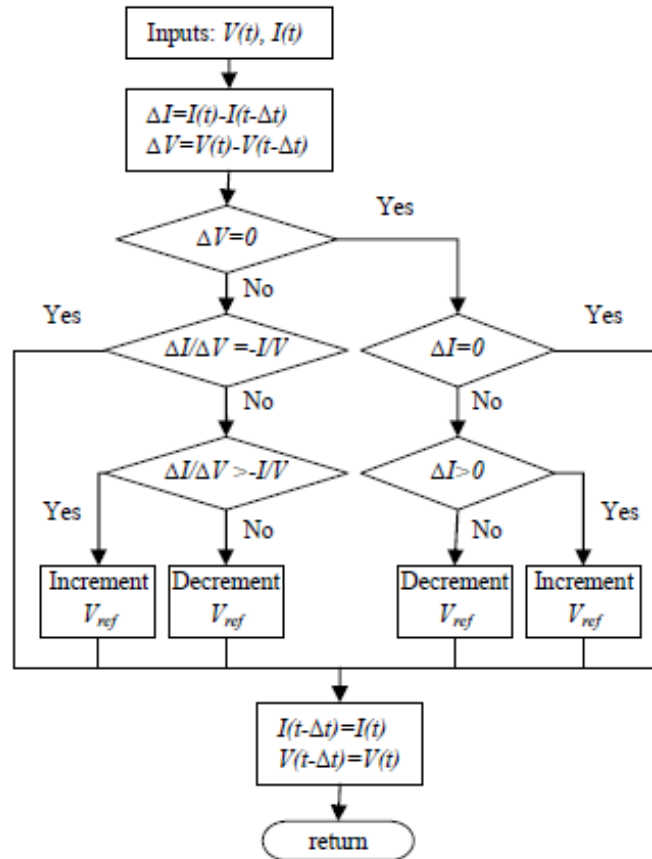


Fig. 3.4 INC algorithm flowchart [3].

As in the P&O algorithm, INC tracks the MPP by perturbing the voltage. However, the difference is that in this case the comparison is made between instantaneous and incremental conductance, instead of comparing the previous and current values of output power, as in the P&O method. In case that the incremental conductance is greater (less) than the negative of the instantaneous conduction, which means that the operating point is on the left (right) of the MPP then the voltage will be increased (decreased).

As in the P&O algorithm, it is very unlikely for the system to stop operation exactly at the MPP. Thus, the INC algorithms use a variable step size to reach the MPP rapidly and

reduce the distance from the MPP, when the MPPT operation has been finished. In addition, an error margin, e , which is larger than the step size, is used in order to stop the INC algorithm operation when the operating point is close enough to the MPP, as follows:

$$\left| \frac{\Delta I}{\Delta V} + \frac{I}{V} \right| < e \quad (3.4)$$

3.2.3 Fractional Open-Circuit Voltage / Short-Circuit Current

Both the fractional open-circuit voltage and fractional short-circuit current methods are based on the fact that the current and voltage of a TEG device have almost linear relationship.

3.2.3.1 Fractional Open-Circuit Voltage

The fractional open-circuit voltage tracking method, usually referred to as constant voltage method, utilizes the fact that the MPP voltage (V_{MPP}) is at a fixed ratio of the open-circuit voltage (V_{OC}) [3]:

$$V_{MPP} = kV_{OC} \quad (3.5)$$

where k is a constant.

As seen from the simulations in Chap. 2.4, the relationship between the output voltage and current of a TEG device is linear, thus it is considered that $k = \frac{1}{2}$.

In the fractional open-circuit voltage method, the power transferred to the load is momentarily interrupted by disconnecting the TEG energy source from the power converter and measuring the open-circuit voltage (while the corresponding output current is zero). Equation (3.5) is then used to calculate the corresponding voltage at the MPP and the operation of the power converter is controlled to reach the MPP. The above operation is repeated periodically. The main disadvantage of this method is that due to the disconnection of the power source, power is not transferred to the load during the open-circuit voltage measurement. Thus, a proper sampling frequency should be selected to reduce power loss to an acceptable level.

3.2.3.2 Fractional Short-Circuit Current

The fractional short-circuit current method has a similar operation to that of the fractional open-circuit voltage tracking method [3]. The difference is that in this method, instead of measuring the open-circuit voltage, the short-circuit current is measured (while the

corresponding output voltage is zero). A similar equation to (3.5) is used to calculate the current at the MPP:

$$I_{MPP} = kI_{SC} \quad (3.6)$$

where $k = \frac{1}{2}$ is a constant.

In this case the I_{SC} value is acquired by short-circuiting the TEG output terminals.

4.

The Proposed MPPT System

4.1 Introduction

The proposed MPPT system, as seen in Fig. 4.1, consists of the following parts:

- TEG energy source (eTEG HV56 in the present application),
- power conditioning system (DC-DC boost converter),
- microelectronic control circuit and
- Pulse Width Modulator.

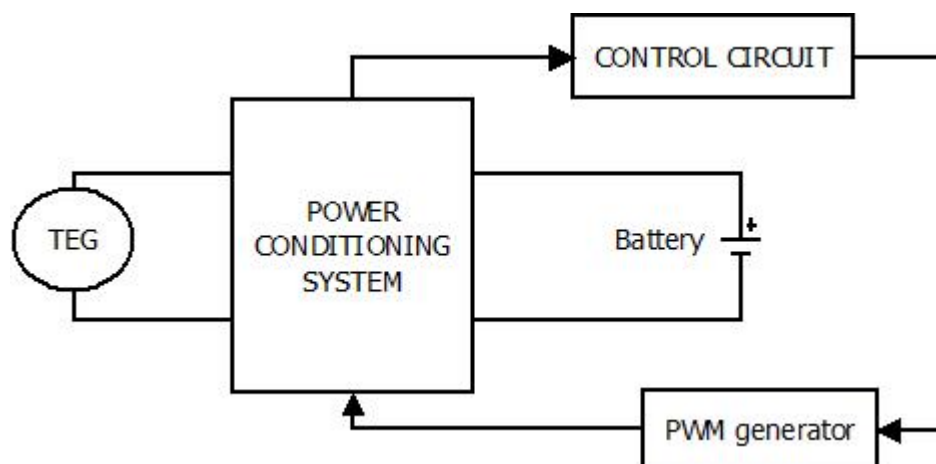


Fig. 4.1 A block diagram of the proposed MPPT system.

The overall circuit-level diagram is depicted in Fig. 4.2. The proposed system consists of low-voltage and low-power microelectronic devices in order to minimize its power

consumption. The individual parts comprising the proposed system are thoroughly analyzed in the following sections.

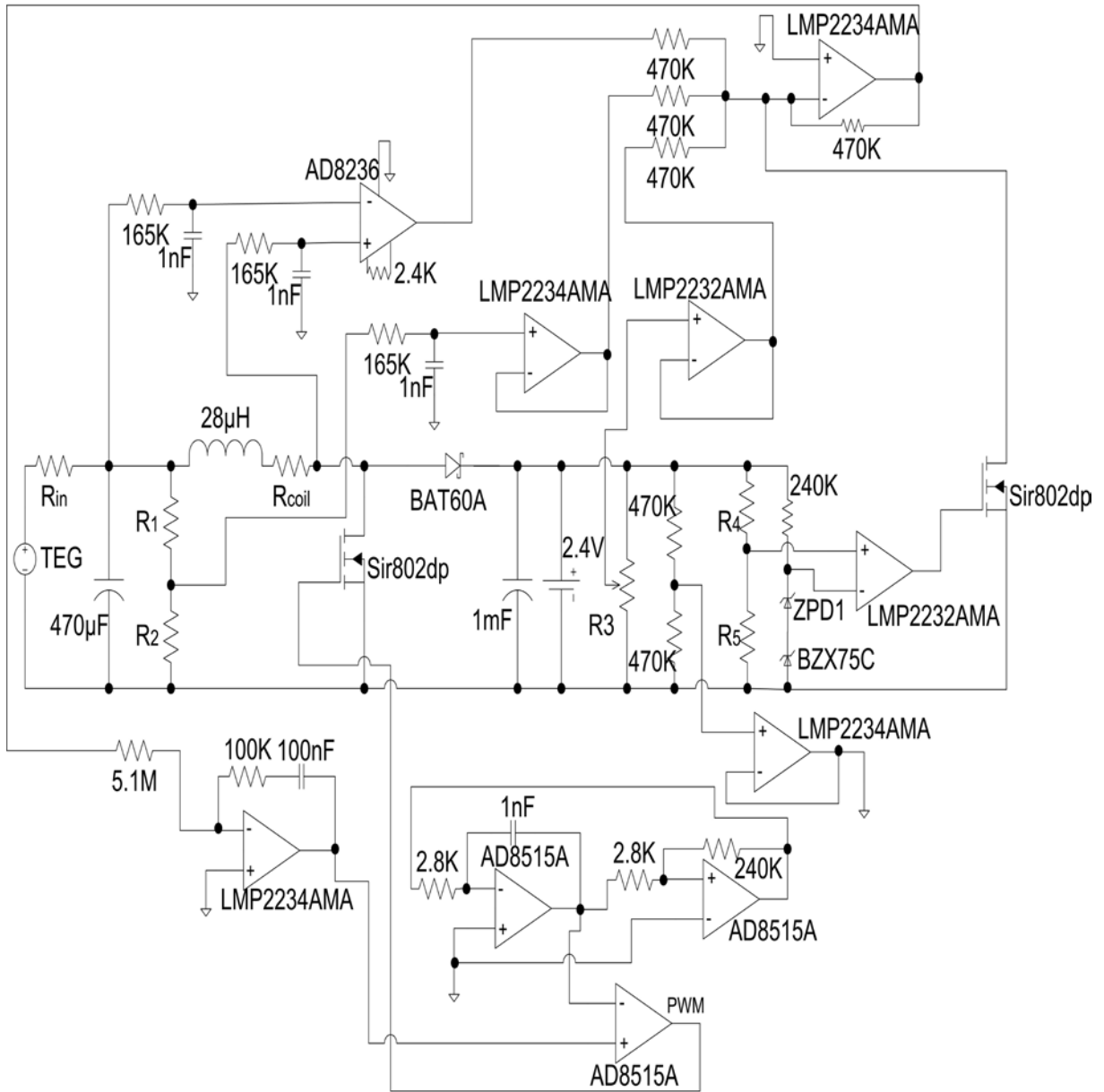


Fig. 4.2 A circuit diagram of the proposed MPPT system.

4.2 TEG energy source

The implemented system as mentioned in Chap. 2, uses the Nextreme eTEG HV56 as energy source. The eTEG HV56 device and the corresponding dimensions can be seen in Fig. 4.3. The eTEG HV56 has considerably small footprint (10.33 mm^2) and profile (0.6 mm), which makes it suitable for small-scale applications with restricted space available.

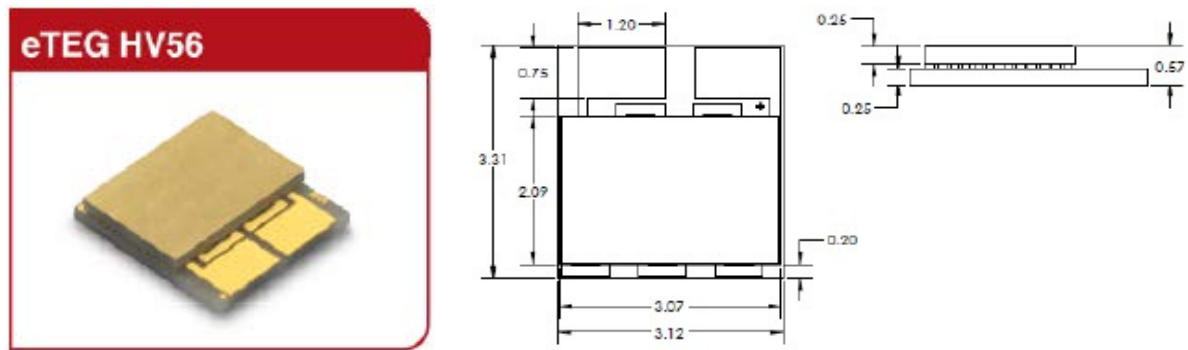


Fig. 4.3 The eTEG HV56 device employed in the proposed system [19].

The structure of eTEG HV56 is made of thin-film thermoelectric material embedded into copper pillar, soldered with eutectic gold-tin (AuSn) solder.

The output voltage, current and consequently power are dependent on the temperature gradient ΔT which is applied on the eTEG HV56. The higher the value of ΔT , the higher the value of voltage, current and power produced. However, the hot side temperature, cold side temperature and ΔT cannot be arbitrarily high, to avoid damaging the module. Table 4.1 shows the operating ranges, as well as the thermal and electrical parameters of the eTEG HV56 module.

| Table 4.1 Operating range, thermal parameters and electrical values of eTEG HV56 [19] | | | |
|---|---------------|----------------|------------|
| Thermal Operating Range | | | |
| Hot side temperature | T_{hot} | 25-200 °C | 298-473 °K |
| Cold side temperature | T_{cold} | 0-50 °C | 273-323 °K |
| Temperature difference | ΔT | 10-200 °C | 10-200 °K |
| Max. mean temperature | $T_{m,max}$ | 150 °C | 423 °K |
| Thermal Parameters | | | |
| Thermal resistance | R | 13.1 K/W | |
| Thermal conductance | K | 0.076 W/K | |
| Seebeck coefficient | α_{pn} | 0.026 V/K | |
| Typical Electrical Maximum (for $\Delta T=200$ °K) and Minimum (for $\Delta T=10$ °K) Values | | | |
| Max. open-circuit voltage | $V_{OC,max}$ | 5.2 V | |
| Max. short-circuit current | $I_{SC,max}$ | 397 mA | |
| Max. power output | $P_{o,max}$ | 516 mW | |
| Max. internal resistance | $R_{in,max}$ | 13.09 Ω | |
| Min. open-circuit voltage | $V_{OC,min}$ | 0.26 V | |
| Min. short-circuit current | $I_{SC,min}$ | 12 mA | |
| Min. power output | $P_{o,min}$ | 1.56 mW | |
| Min. internal resistance | $R_{in,min}$ | 10.83 Ω | |

In order to provide the required power to the proposed system, the eTEG HV56 power generator evaluation kit has been used, which is depicted in Fig 4.4.



Fig. 4.4 The Nextreme eTEG HV56 power generator evaluation kit [20].

As seen in Fig 4.4, the evaluation kit is an easy-to-use, self-contained kit. The pink foam provides thermal insulation to the thick film heater from the ambient temperature. The individual parts of the kit are shown in Fig. 4.5.

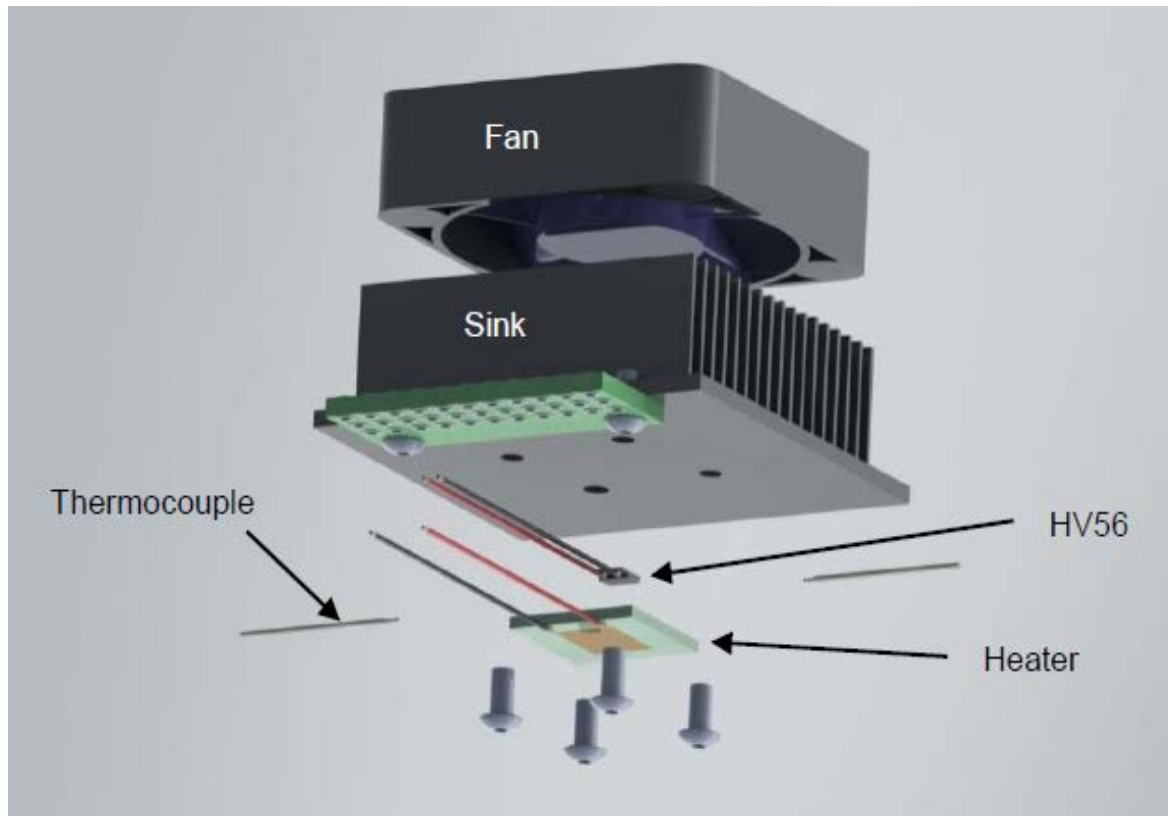


Fig. 4.5 The parts comprising the Nextreme eTEG HV56 Power Generator Evaluation Kit [20].

The power generator evaluation kit consists of the following parts:

- **HV56 TEG** as energy source,
- **thick film heater** for heating the hot side of the TEG,
- **heat sink/fan assembly** for cooling the cold side of the TEG,
- **two Type K thermocouples** for temperature measurement and
- **12 Vdc transformer** as power supply for the fan.

4.3 DC-DC Boost Converter

Due to variations in temperature gradient, in order to maximum power transfer from the TEG device to the load (which consists of two Ni-MH batteries connected in series with a total voltage of 2.4 V) a power conditioning system has been developed. The input of the power conditioning system is connected to the TEG output and its output is connected directly to the battery.

The available TEG module, with the existing temperature gradient, produced much less output voltage than that required to charge the battery. Thus, the suitable power conditioning system for the present application is a DC-DC Boost converter, in order to step up the input voltage.

As seen in Fig 4.6, the boost converter, which has been developed, consists of the following parts:

- input capacitor,
- 28 μH inductor,
- Schottky diode,
- MOSFET and
- output capacitor.

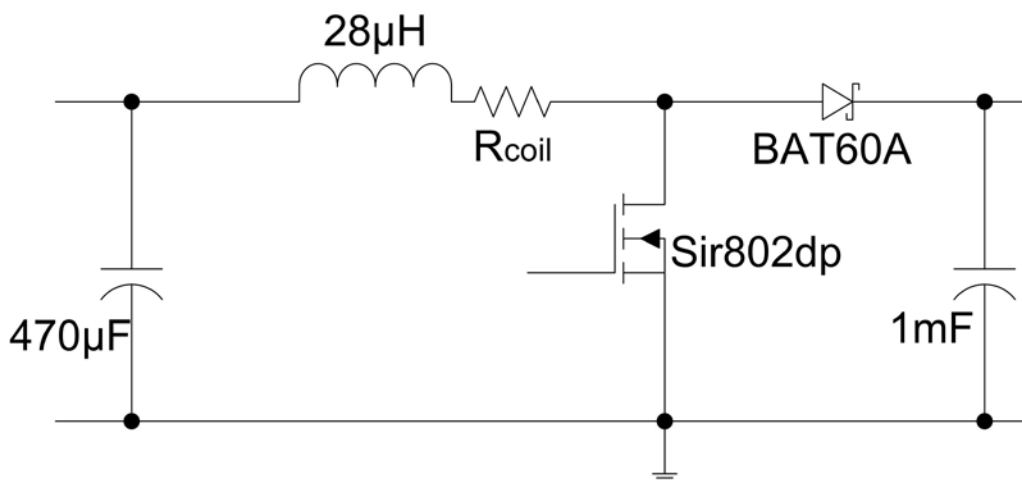


Fig. 4.6 Boost converter diagram

The selection of each part is described in details in Sections 4.3.1-4.3.5.

4.3.1 Input capacitor

The input and output capacitors are used to filter out the input and output voltage ripple, respectively, due to the switching operation of the boost converter circuit. Their values has been selected such that the input voltage ripple is substantially reduced.

4.3.2 Boost inductor

The necessity in reduction of the system size and power loss led to the design and implementation of a planar core inductor operating at high frequency. Planar core inductors are part of a printed circuit board with windings made of printed circuit tracks or constructed with multi-layer circuit boards. The basic advantages of the implementation of a planar core inductor over conventionally shaped inductors are:

- significantly low profile, which is of interest in small-scale system development,
- improved heat dissipation due to large surface area to volume ratio,
- large magnetic cross section, which leads to fewer turns needed for the same value of inductance and
- lower leakage inductance due to the easily implemented interleaving and fewer turns.

Calculations have been made for four possible frequencies and for two available cores to design a planar core inductor with the minimum power dissipation. The following calculations are for 100 kHz switching frequency and for R-41805 EC type R (round permalloy 80) ferrite planar core. The values of $I_{sc}=1.678$ A, $V_{oc}=0.563$ V and $V_{out}=1.8$ V have been taken into consideration to calculate the inductor parameters.

The inductance is given by the following equation:

$$L = V_L \frac{\Delta t}{\Delta I} \quad (4.1)$$

where V_L is the inductor voltage (it is equal to V_d),

Δt is the on-time of the duty cycle and

ΔI is the maximum peak-to-peak current in order to avoid operation in discontinuous conduction mode.

Operation in continuous conduction mode provides higher efficiency and less complex calculations, as the output voltage depends only on the values of input voltage and duty cycle, as described by the following fundamental boost-converter equation:

$$V_{out} = \frac{V_{in}}{1-D} \quad (4.2)$$

The off-time of the switch can be calculated using the following equation:

$$t_{off} = \frac{T_s V_d}{V_o} = \frac{10^{-5} \times 0.563}{1.8} = 0.31278 \times 10^{-5} \text{ s} \quad (4.3)$$

where T_s is the switching period and

V_o is the output voltage of the converter.

Using equation (4.3), Δt can be calculated by the following equation:

$$\Delta t = t_{on} = T_s - t_{off} = 10^{-5} - 0.31278 \times 10^{-5} = 0.6872 \times 10^{-5} \text{ s} \quad (4.4)$$

The value of ΔI has been set to 10%:

$$\Delta I = I_{pp} = 0.1 \times 1.678 = 0.1678 \text{ A} \quad (4.5)$$

Substituting the values calculated from equations (4.3) through (4.5) to equation (4.1), the inductance can be calculated as follows:

$$L = 0.563 \frac{0.6872 \times 10^{-5}}{0.1678} = 23.0568 \text{ } \mu\text{H} \quad (4.6)$$

The number of the required turns to obtain the requested inductance value is calculated by the following equation:

$$L = N^2 \times A_L \Rightarrow N = \sqrt{\frac{L}{A_L}} = \sqrt{\frac{23.0568 \times 10^{-6}}{3244 \times 10^{-9}}} \approx 3 \text{ turns} \quad (4.7)$$

where A_L is the inductance factor of the core in mH/1000 turns.

The change in flux density for the specific inductor is given by the following equation:

$$\Delta B_{ac} = \frac{L \Delta i}{N A_e} = \frac{23.0568 \times 10^{-6} \times 0.1678}{3 \times 40.1 \times 10^{-6}} = 32.1607 \text{ mT} = 321.607 \text{ Gauss} \quad (4.8)$$

where A_e is the effective core area.

Using equation (4.9), the core power loss – flux density curve can be plotted as shown in Fig. 4.7 and the power loss per cm^3 of the inductor core can be calculated as follows:

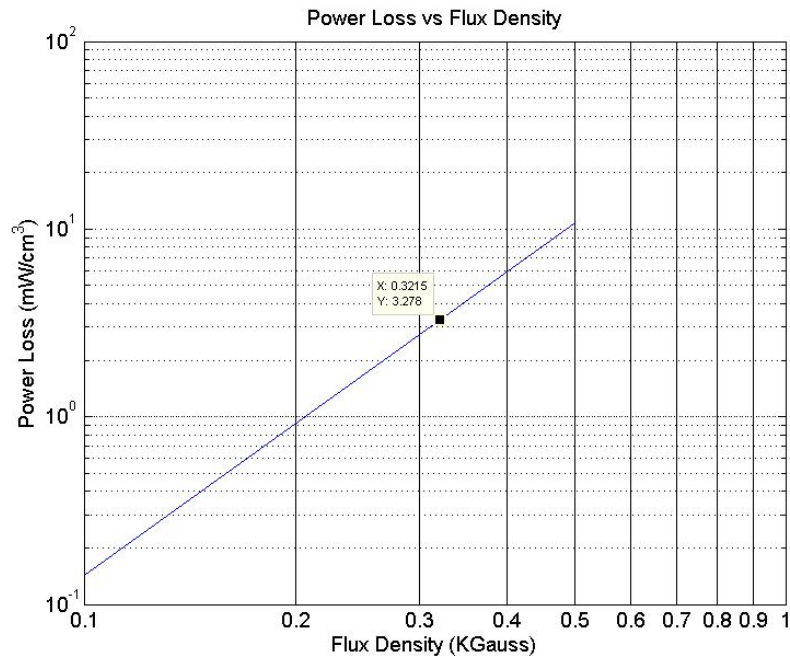


Fig. 4.7 Core power loss – Flux density curve at 100 kHz switching frequency.

$$\begin{aligned}
 PL &= af^c B^d = 0.036 \times 100^{1.64} \times (0.321607)^{2.68} \\
 &= 3.2805 \text{ mW/cm}^3
 \end{aligned} \tag{4.9}$$

where a, c, d are constant values,

f is the switching frequency in kHz and

B is the flux density in kGs.

The available core has a volume of 1.944 cm^3 . Thus, the power loss of the core is calculated by the following equation:

$$P_{core,loss} = 3.2805 \times 1.944 = 6.3772 \text{ mW} \tag{4.10}$$

Assuming a current density of 4 A/mm^2 , the cross-sectional area of the wire for the maximum current of 0.894 A can be calculated by the following equation:

$$A_x = \frac{0.894}{4} = 0.2235 \text{ mm}^2 \tag{4.11}$$

where A_x is the printed circuit track cross sectional area.

Since the thickness of the copper of the printed circuit board, which will be used to construct the inductor, is 0.5 mm, the width of the printed tracks is calculated using the following equation:

$$x = \frac{A_x}{\text{profile}} = \frac{0.2235 \text{ mm}^2}{0.5 \text{ mm}} = 0.447 \text{ mm} \quad (4.12)$$

The dimensions of the available planar core and the form of the printed circuit tracks are shown in Fig. 4.8. It is observed that it is possible to design tracks with approximately 1 mm width.

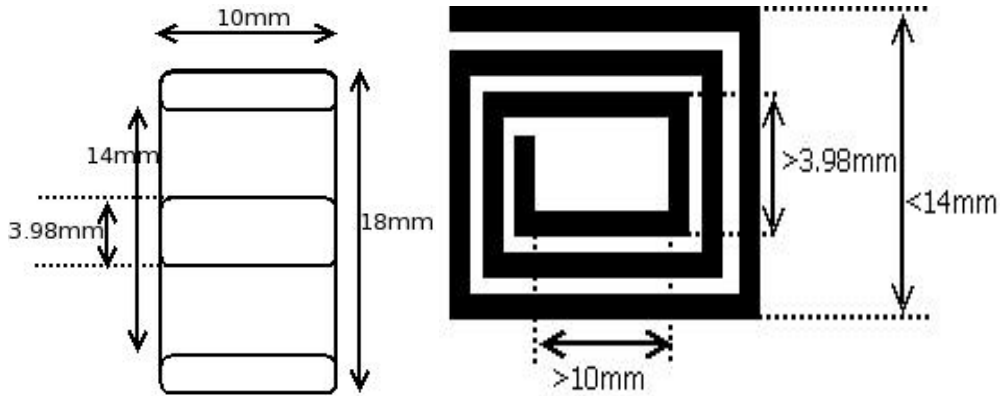


Fig. 4.8 The inductor construction: dimensions of the available core and the form of the printed circuit tracks.

Due to the core dimensions restrictions, shown in Fig. 4.8, the distance between the printed tracks results to be not more than 1mm. Therefore, the total length of the printed tracks turns up to be 14.0243 cm.

The resistance of the printed tracks is calculated as follows:

$$R = \rho \frac{L}{A_x} (1 + t_c (T - 25)) \quad (4.13)$$

where ρ is the resistivity of copper, $\rho = 1.7 \times 10^{-6} \Omega \text{ cm}$,

L is the length of the track,

T is the track temperature in degrees Celcius and

t_c is the temperature coefficient of copper, $t_c = 3.9 \times 10^{-3} \Omega / \Omega / C$.

According to (4.13), the resistance of the printed tracks at 293 °K is calculated to be equal to 4.68 m Ω .

$$P_{\text{wind,loss,max}} = I^2 R = 0.894^2 \times 4.68 \times 10^{-3} = 3.7 \text{ mW} \quad (4.14)$$

The inductor total power dissipation is equal to the sum of the core power loss and the windings power loss. Hence, the total power loss of the inductor is calculated by the following equation:

$$P_{tot,loss} = P_{wind,loss} + P_{core,loss} \quad (4.15)$$

The minimum power dissipation for one TEG module with temperature gradient $\Delta T=10.4$ °K is 6.7197×10^{-9} W and the maximum power dissipation for two TEG modules connected in parallel with temperature gradient $\Delta T=40$ °K is 1.007×10^{-2} W.

Due to the core dimensions restrictions, the cross sectional area of the printed circuit tracks is rather small. In order to decrease the DC coefficient of the resistance of the printed circuit tracks, the leakage inductance and the flux density, a copper wire has been soldered on the printed circuit tracks. The measured inductance value of the constructed inductor is 28 μ H. The constructed inductor can be seen in Fig. 4.9.

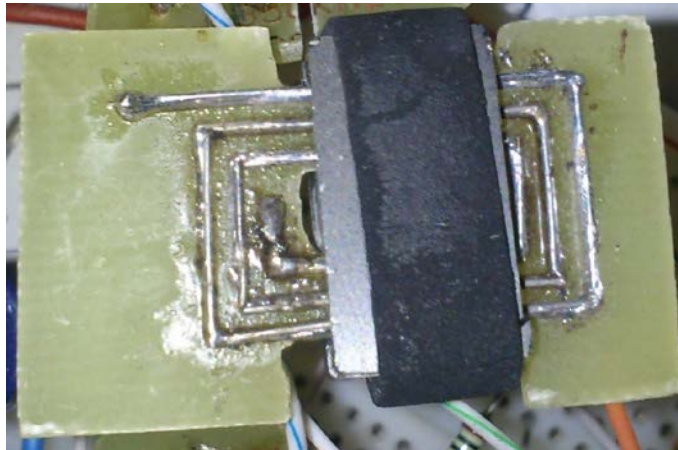


Fig. 4.9 The constructed inductor.

4.3.3 Schottky diode rectifier

In order to obtain a low voltage drop across the diode and fast recovery time, a Schottky diode rectifier has been used. The total power dissipation in the diode is the sum of the conduction power loss in continuous conduction mode, P_{CCM} , and the switching power loss, P_{SW} , and it is calculated by the following equation:

$$P_{tot,loss} = P_{CCM} + P_{SW} \quad (4.15)$$

Initially, the maximum output current is calculated by the following equation:

$$P_{TEG} = V_{MPP} I_{MPP} = \frac{V_{OC}}{2} \frac{I_{SC}}{2} \quad (4.16)$$

Assuming that the entire power produced by the TEG is transferred to the load, then since the output voltage is known, the output current can be calculated by the following equation:

$$I_O = \frac{P_{TEG}}{V_O} \quad (4.17)$$

where V_O is the output voltage.

The power dissipation in continuous conduction mode is calculated from the following equation:

$$P_{CCM} = I_O V_F + I_O^2 R_d \quad (4.18)$$

where V_F is the forward voltage drop,

R_d is the forward resistance and

I_O is the output current.

Substituting I_O from equation (4.17) to (4.18), equation (4.18) can be written as follows:

$$P_{CCM} = \frac{P_{TEG}}{V_O} V_F + \left(\frac{P_{TEG}}{V_O}\right)^2 R_d \quad (4.19)$$

The switching power loss of the Schottky diode can be calculated by the following equation:

$$P_{SW} = Q_C V_O f_{SW} \quad (4.20)$$

where Q_C is the diode junction charge and

f_{SW} is the switching frequency.

Finally, using equations (4.15), (4.19) and (4.20), the total power loss of the diode can be calculated according to the following equation:

$$P_{tot,loss} = \frac{P_{TEG}}{V_O} V_F + \left(\frac{P_{TEG}}{V_O}\right)^2 R_d + Q_C V_O f_{SW} \quad (4.21)$$

The total power loss among many diodes on the market has been calculated using equation (4.21). The most suitable device for the specific application with a minimum total power loss, for one TEG module with temperature gradient $\Delta T=10.4$ °K, of 0.021 mW and a maximum total power loss, for two TEG modules connected in series with temperature gradient $\Delta T=40.3$ °K, of 2 mW at 100 kHz is the diode BAT60A.

4.3.4 MOSFET

The switching operation of the power converter is controlled by a MOSFET. The selection of the suitable MOSFET for the system is based on the power loss during the operation and an acceptable switching-frequency capability. To reduce the total power dissipation, a reduction in switching power loss, P_{SW} , and power dissipation during conduction of the switch, P_{On} , is of importance, as given by the following equation:

$$P_{tot,loss} = P_{SW} + P_{On} \quad (4.22)$$

On the other hand, the power loss during the off-state is of very low value, compared to the switching power loss and the power loss during the on-state, and can be neglected.

Initially, the power loss during the switching operation is calculated. The power loss during the switching operation depends on the dissipated energy during the turn-on and turn-off transitions, and it is given by the following equation:

$$P_{sw} = (E_{on} + E_{off})f_s \quad (4.23)$$

where E_{on} is the dissipated energy during the turn-on transition and

E_{off} is the dissipated energy during the turn-off transition.

The value of E_{on} is calculated as follows:

$$E_{on} = V_d I_{don} \frac{t_{ri} + t_{fu}}{2} + Q_{rr} V_d \quad (4.24)$$

where t_{ri} is the current rise time,

I_{don} is the on-state drain current,

Q_{rr} is the body diode reverse recovery charge and

t_{fu} is the switch voltage fall time to a small on-state value of $I_d R_{DSon}$.

The value of I_{don} is given by the following equation:

$$I_{don} = I_d - \frac{\Delta I_d}{2} \quad (4.25)$$

The value of t_{fu} is given by the following equation:

$$t_{fu} = \frac{t_{fu1} + t_{fu2}}{2} \quad (4.26)$$

where t_{fu1} and t_{fu2} are the fall times defined through the gate current and the gate-drain capacitances.

The values of t_{fu1} and t_{fu2} are given by the following equations:

$$t_{fu1} = (V_d - R_{DSon} I_d) R_G \frac{C_{GD1}}{V_{Dr} - V_{(plateau)}} \quad (4.27)$$

$$t_{fu2} = (V_d - R_{DSon} I_d) R_G \frac{C_{GD2}}{V_{Dr} - V_{(plateau)}} \quad (4.28)$$

where R_{DSon} is the drain-source on-state resistance,

I_D is the continuous drain current,

R_G is the gate resistance,

V_{Dr} is the voltage across the diode,

$V_{(plateau)}$ is the gate plateau voltage observed during switching transition,

C_{GD1} is the gate-drain capacitance and is equal to $C_{rSS}(V_d)$ and

C_{GD2} is the gate-drain capacitance and is equal to $C_{rSS}(I_d R_{DSon})$.

The value of E_{off} is given by the following equation:

$$E_{off} = V_d I_{doff} \frac{t_{ru} + t_{fi}}{2} \quad (4.29)$$

where I_{doff} is the off-state drain current,

t_{fi} is the current fall time and

t_{ru} is the switch voltage rise time to an off-state value of V_d .

The value of I_{doff} is calculated as follows:

$$I_{doff} = I_d + \frac{\Delta I_d}{2} \quad (4.30)$$

The rise time t_{ru} is given by:

$$t_{ru} = \frac{t_{ru1} + t_{ru2}}{2} \quad (4.31)$$

where t_{ru1} and t_{ru2} are the rise times defined through the gate current and the gate-drain capacitances.

The values of t_{ru1} and t_{ru2} are calculated as follows:

$$t_{ru1} = (V_d - R_{DSon} I_d) R_G \frac{C_{GD1}}{V_{(plateau)}} \quad (4.32)$$

$$t_{ru2} = (V_d - R_{DSon} I_d) R_G \frac{C_{GD2}}{V_{(plateau)}} \quad (4.33)$$

Finally, the power dissipation during the on-state of the switch, which is a major contribution to the power loss, is calculated using the following equation:

$$P_{On} = R_{DSon} I_{rms}^2 \quad (4.34)$$

where

$$I_{rms}^2 = D I_d^2 \quad (4.35)$$

and D is the duty cycle.

Combining (4.24) - (4.33), equation (4.23) can now be written as follows:

$$P_{SW} = V_d (V_d - R_{DSon} I_d) R_G (C_{r_{ss}} (V_d) + C_{r_{ss}} (R_{DSon} I_d)) \left(\frac{2I_D + \Delta I_D}{8V_{(plateau)}} + \frac{2I_D - \Delta I_D}{8(V_{Dr} - V_{(plateau)})} \right) + V_d \left(\left(\frac{I_D + \Delta I_D}{2} \right) \frac{t_{fi}}{2} + \left(\frac{I_D - \Delta I_D}{2} \right) \frac{t_{ri}}{2} \right) + Q_{rr} V_d \quad (4.36)$$

Also by combining (4.34) - (4.36), equation (4.22) can be written as follows:

$$P_{tot,loss} = V_d (V_d - R_{DSon} I_d) R_G (C_{r_{ss}} (V_d) + C_{r_{ss}} (R_{DSon} I_d)) \left(\frac{2I_D + \Delta I_D}{8V_{(plateau)}} + \frac{2I_D - \Delta I_D}{8(V_{Dr} - V_{(plateau)})} \right) + V_d \left(\left(\frac{I_D + \Delta I_D}{2} \right) \frac{t_{fi}}{2} + \left(\frac{I_D - \Delta I_D}{2} \right) \frac{t_{ri}}{2} \right) + Q_{rr} V_d + R_{DSon} I_{rms}^2 \quad (4.37)$$

Equation (4.37) has been used to calculate the total power loss among many MOSFETs available on the market. The MOSFET SiR802DP has been selected as the MOSFET with the less power dissipation for the TEG application under study. The minimum total power loss, for one TEG module with temperature gradient $\Delta T=10.4$ °K, of the specific module at a 100 kHz switching frequency has been calculated to be equal to 0.26 mW and the maximum total power loss, for two TEG modules connected in series with temperature gradient $\Delta T=40.3$ °K, has been calculated to 2.3 mW.

4.3.5 Output capacitor

The minimum value of the output capacitor has been calculated using the following equation:

$$C_{OUT,min} = \frac{I_{OUT,max}DC_{max}}{f_s\Delta V_{OUT}} \quad (4.38)$$

where $I_{OUT,max}$ is the maximum value of the output current,

DC_{max} is the maximum value of the duty cycle,

f_s is the switching frequency and

ΔV_{OUT} is the maximum value of the acceptable output voltage ripple.

The maximum value of the output current has been set to 1.673 mA. The switching frequency is 100 kHz. The maximum acceptable ripple has been selected equal to 0.5% of the output voltage. The following equation for the boost converter has been used to define the maximum value of the duty cycle:

$$D = 1 - \frac{V_{in}}{V_{out}} \quad (4.39)$$

where V_{in} is the input voltage to the boost converter and

V_{out} is the output voltage of the boost converter.

The input voltage is equal to 0.563 V and the output voltage is equal to 2.4 V. Thus the duty cycle has been calculated as follows:

$$D = 1 - \frac{0.563}{2.4} = 0.765 \approx 76\% \quad (4.40)$$

The minimum value of the output capacitor can now be calculated using (4.38) as follows:

$$C_{OUT,min} = \frac{1.673 \times 0.76}{100 \times 10^3 \times 0.012} \approx 1 \text{ mF} \quad (4.41)$$

Using an oscilloscope connected in parallel across the output capacitor it was verified that the selected output electrolytic capacitor adequately reduces the output voltage ripple.

4.4 Microelectronic control system

The microelectronic control system, as seen in Fig. 4.10, consists of the following parts:

- Low-Pass Filters (LPF),
- a voltage divider,

- buffer amplifiers,
- a differential amplifier,
- an inverting adder and
- a Proportional Integral (PI) controller.

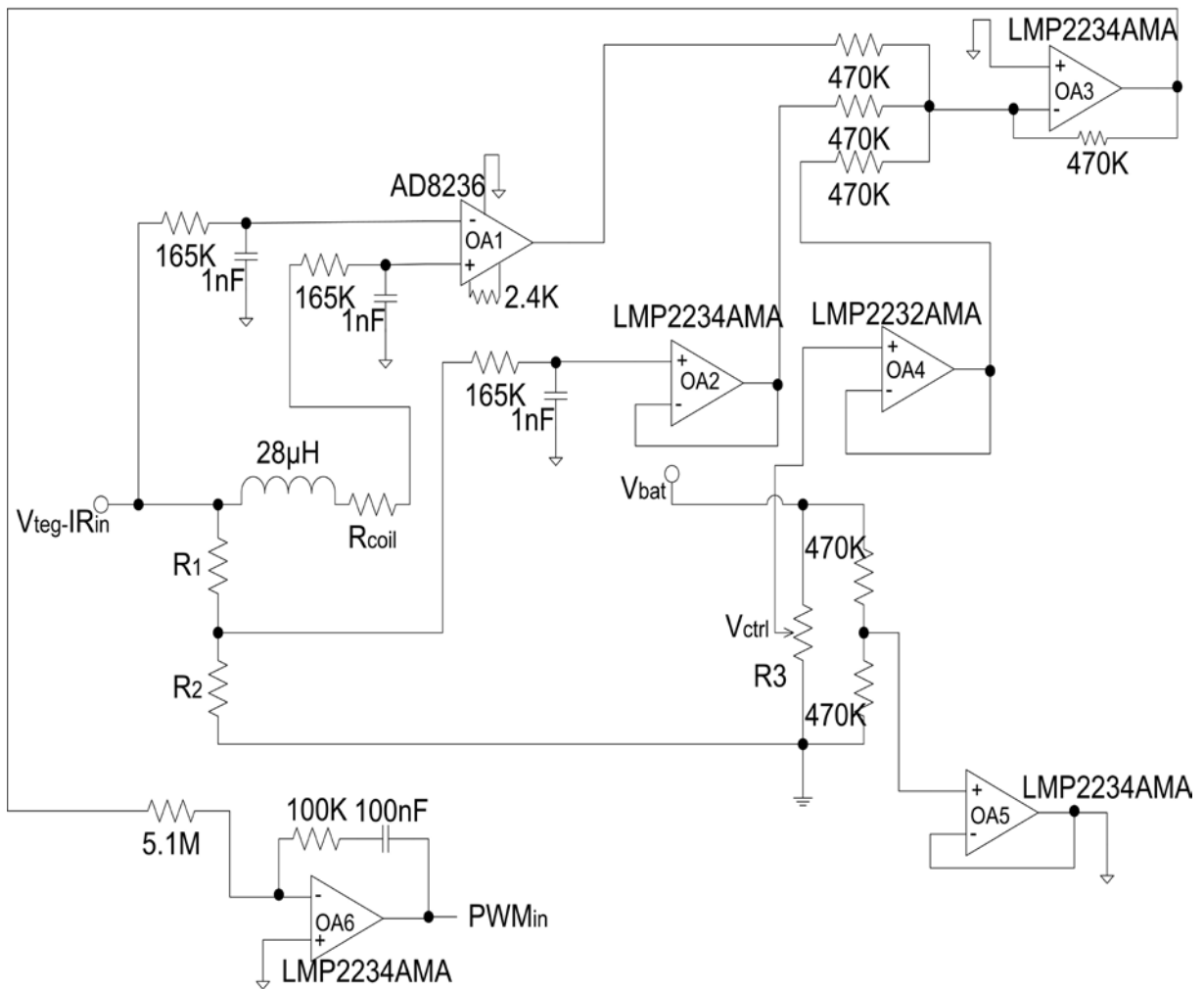


Fig. 4.10 Control circuit diagram.

The design of the microelectronic system is based on the following equation:

$$\frac{dP}{dV} = \frac{dVI}{dV} = \frac{dV}{dV} I + \frac{dI}{dV} V = I - \frac{1}{R_{TEG}} V \quad (4.42)$$

where the samples of voltage, V , and current, I , are acquired from the voltage divider and inductor, respectively.

The derivative $\frac{dP}{dV}$ is:

- positive on the left of the MPP,
- negative on the right of the MPP and
- zero at the MPP.

The microelectronic control system has been designed to minimize the absolute value of the derivative $\frac{dP}{dV}$ as much as possible, in order to transfer the operating point as close to the MPP as possible, regardless of the value of the temperature gradient, ΔT . The control operation is preprogrammed to operate on a specific MPP curve as shown in Fig. 1.2.

Each part is described in details in the following paragraphs.

Due to the switching operation of the circuit, a voltage ripple is developed at the inputs of the differential amplifier AO1 and buffer amplifier OA2. Thus, for precise circuit response, the connection of a Low-Pass Filter (LPF) between the sampling points and inputs of OA1 and OA2 is mandatory.

Targeting to reduce the power consumption of the microelectronic control system, a passive LPF has been implemented. Its 3-dB cut-off frequency has been set to 1% of the switching frequency. The cut-off frequency is given by the following equation:

$$f_c = \frac{1}{2\pi R_1 C_1} \quad (4.43)$$

To reduce the power loss of the filter, a low value of available capacitors has been selected in order to acquire as high value of resistor as possible. For $C_1=1\text{nF}$ the value of R_1 can be calculated using the following equation:

$$(4.43) \Rightarrow R_1 = \frac{1}{2\pi f_c C_1} = \frac{1}{2\pi \cdot 10^3 \cdot 10^{-9}} = 159 \text{ k}\Omega \quad (4.44)$$

The voltage coefficient of equation (4.42) is set by the voltage divider attenuation coefficient. The voltage divider, as seen in Fig. 4.67, consists of resistors R_1 and R_2 . The fundamental equation of the voltage divider for the general case is the following:

$$V_o = \frac{Z_2}{Z_1+Z_2} V_I \quad (4.45)$$

The factor $\frac{1}{R_{TEG}}$ of equation (4.42) is obtained by the attenuation coefficient of the voltage divider and is given by the following equation:

$$G_{vd} = \frac{1}{R_{TEG}} = \frac{R_2}{R_1 + R_2} \quad (4.46)$$

The gain of the voltage divider, G_{vd} , has been calculated for R_{TEG} at $\Delta T=20$ K for one TEG and two TEG modules connected in series and in parallel, respectively. The gain is constant during the experiments.

The following calculations demonstrate the selection of resistors R_1 and R_2 to obtain the required gain for one TEG.

The internal resistance of TEG, R_{TEG} , at $\Delta T=20$ K is calculated to be equal to 10.95Ω . The required voltage divider attenuation coefficient can be calculated using equation (4.46), as follows:

$$G_{vd} = \frac{1}{R_{TEG}} = \frac{1}{10.95} = 0.0913 \quad (4.47)$$

Also, equation (4.46) can be re-written as follows:

$$R_2 = \frac{R_1 G_{vd}}{1 - G_{vd}} \quad (4.48)$$

To reduce power consumption, a high value of resistor R_1 has been selected. For $R_1=470$ k Ω and $G_{vd}=0.0913$ the value of R_2 is then calculated from equation (4.48):

$$R_2 = \frac{R_1 G_{vd}}{1 - G_{vd}} = \frac{470 \text{ k}\Omega \times 0.0913}{1 - 0.0913} \approx 47 \text{ k}\Omega \quad (4.49)$$

To acquire impedance matching conditions and linearity between the sub-circuits of the control circuit, the use of buffer amplifiers is mandatory. Buffer amplifiers have ideally infinite input impedance and zero output impedance, while also providing unity gain. In addition, the use of buffer amplifiers provides the ability to drive more than one circuits.

The operational amplifier OA2 is configured as a buffer amplifier, interposed between the voltage divider and input resistance of inverting adder, in order to obtain linear response. The output level of the specific buffer amplifier is the same as that of the voltage divider output.

The buffer amplifier consisting of operational amplifier OA5 is used to provide a reference signal for the control circuit. It grants linearity and ability to drive inputs of many sub-circuits, as seen in Fig. 4.1. The output of OA5 depends on the charge level of the battery and is given by the following equation:

$$V_{ref} = \frac{470 \text{ k}\Omega}{470 \text{ k}\Omega + 470 \text{ k}\Omega} V_{bat} = \frac{1}{2} V_{bat} \quad (4.50)$$

where V_{bat} is the voltage of the battery bank.

Finally, the operational amplifier OA4 is configured as a buffer amplifier and provides linearity and impedance matching between resistor R_3 and the input resistance of the inverting adder. The circuit consisting of R_3 and OA4 provides the additional input V_{ctrl} to the inverting adder, thus granting the ability to control the output level of the inverting adder to track the TEG MPP. As soon as the potentiometer R_3 has been adjusted so that the system operating point is at the MPP for $\Delta T = 20 \text{ }^\circ\text{K}$, which is in the middle of the entire ΔT range, the value of the potentiometer R_3 remains constant during the MPP tracking process and at different values of ΔT .

To acquire the current coefficient of (4.42), the inductor resistance voltage drop is sampled and applied to the input of the instrumentation amplifier OA1. An instrumentation amplifier has been selected for better accuracy and stability, as the current and inductor resistance values are substantially low, eliminating the necessity for impedance matching and providing adequately high common-mode rejection ratio.

The output of OA1 is given by the following equation:

$$V_{diff_amp} = G_{diff_amp}(-V_{ind}) \quad (4.51)$$

where V_{ind} is the inductor resistance voltage drop and

G_{diff_amp} is the instrumentation amplifier gain.

The value of V_{ind} is calculated as follows:

$$V_{ind} = IR_{ind} \quad (4.52)$$

where R_{ind} is the inductor winding resistance.

The instrumentation amplifier gain is given by:

$$G_{diff_amp} = \frac{1}{R_{ind}} \quad (4.53)$$

Substituting (4.52) and (4.53) in (4.51), equation (4.51) is re-written as follows:

$$(4.51) \xrightarrow{(4.52),(4.53)} V_{diff_amp} = \frac{1}{R_{ind}} (-IR_{ind}) = -I \quad (4.54)$$

The instrumentation amplifier reference voltage is set to V_{ref} to employ only positive supply voltage and be able to respond to positive and negative values of the input signal with respect to V_{ref} . Therefore, (4.54) can be written as follows:

$$(4.54) \xrightarrow{(4.50)} V_{diff_amp} = -I + \frac{1}{2}V_{bat} \quad (4.55)$$

The inductor winding resistance has been experimentally measured to be equal to $5.55 \times 10^{-3} \Omega$. The gain of the differential amplifier can be calculated using (4.53).

$$G_{diff_amp} = \frac{1}{R_{ind}} = \frac{1}{5.55 \times 10^{-3}} = 180 \quad (4.56)$$

According to the AD8236 instrumentation amplifier datasheet, the gain resistance can be defined by the following gain equation:

$$R_G = \frac{420 \text{ k}\Omega}{G_{diff_amp} - 5} \quad (4.57)$$

Thus, using (4.57) the value of R_G is set equal to 2.4 k Ω .

The inverting adder sums the input signals of the processed samples of V, I and level control voltage and inverts the output. The three input signals are the following:

- differential amplifier OA1 output: -I,
- buffer amplifier OA2 output: $\frac{1}{R_{TEG}}V$ and
- buffer amplifier OA4 output: V_{ctrl} .

Considering that input resistances equal to each other have been used and they are also equal to the feedback resistance the output of the inverting adder is given by the following equation:

$$V_{adder} = - \left(-I + \frac{1}{R_{TEG}}V + V_{ctrl} \right) = I - \frac{1}{R_{TEG}}V - V_{ctrl} \quad (4.58)$$

To acquire an output signal within the power supply voltage range, the reference voltage of the inverting adder is set to V_{ref} . Therefore, using (4.50), (4.58) is now written as follows:

$$(4.58) \xrightarrow{(4.50)} V_{adder} = I - \frac{1}{R_{TEG}}V - V_{ctrl} + \frac{1}{2}V_{bat} \quad (4.59)$$

To ensure a stable operation of the control loop, a PI controller is employed. Fig. 4.11 depicts the block diagram of the control system developed.

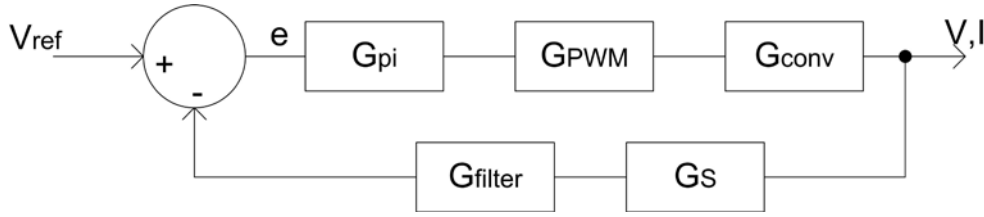


Fig. 4.11 A block diagram of the control system developed.

As shown in Fig 4.11, the control loop consists of the following parts:

- PI controller transfer function:

$$G_{pi} = K_p + \frac{K_i}{s} \quad (4.60)$$

- PWM modulator gain:

$$G_{pwm} = \frac{1}{V_{TH} - V_{TL}} \quad (4.61)$$

where V_{TH} and V_{TL} are the maximum and minimum voltage levels of the triangular waveform produced by the PWM modulator circuit as described in Section 4.5.

- Boost converter transfer function:

$$G_{conv} = \frac{V_{acc}}{sL} \quad (4.62)$$

- RC filter transfer function:

$$G_{filter} = \frac{1}{1 + RCs} \quad (4.63)$$

- TEG source small-signal gain:

$$G_s = 1 - \frac{R_{th}}{R_{TEG}} \quad (4.64)$$

where R_{th} is the TEG small-signal internal resistance, which is determined using (4.42) by the following calculations:

$$\tilde{v} = \tilde{i}R_{th} \quad (4.65)$$

$$(4.42) \xrightarrow{(4.59)} \frac{d\tilde{p}}{d\tilde{v}} = \tilde{i} - \frac{1}{R_{TEG}} \tilde{i} R_{th} = \tilde{i} \left(1 - \frac{R_{th}}{R_{TEG}}\right) \quad (4.66)$$

According to Fig. 4.11, the error signal is given by the following equation:

$$e = V_{ref} - \left(I - \frac{1}{R_{TEG}} V\right) \quad (4.67)$$

Implementing the block diagram of Fig. 4.11 and the transfer functions given by (4.61) - (4.64) in Simulink, the K_p (proportional gain) and K_i (integral gain) parameters of the PI controller have been derived. With minor additional tuning the resulting values of K_p and K_i are the following:

$$K_p = 0.0196 \quad (4.68)$$

$$K_i = 1.9608 \quad (4.69)$$

The circuit implementing the PI controller is shown in Fig. 4.12.

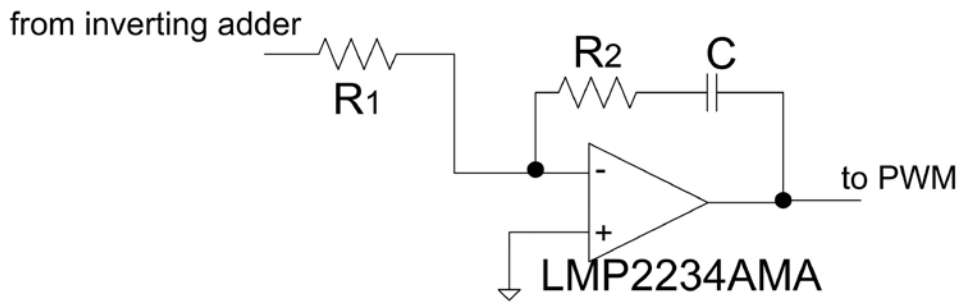


Fig. 4.12 PI controller circuit.

The K_i parameter is given by the following equation:

$$K_i = \frac{1}{CR_1} \quad (4.70)$$

Substituting the value of integral gain from (4.69) in (4.70) and for an available capacitor of 100 nF, the value of resistance R_1 is calculated.

The K_p parameter is given by the following equation:

$$K_p = \frac{R_2}{R_1} \quad (4.71)$$

Again, substituting the value of the proportional gain from (4.68) in (4.71) and for the previously calculated value of resistance R_1 , the value of resistance R_2 is calculated.

4.5 Pulse Width Modulator

The Pulse Width Modulation (PWM) circuit drives the MOSFET with the required switching frequency. The pulse width is modulated via a feedback loop by the PI controller. The PWM circuit diagram is presented in Fig. 4.13.

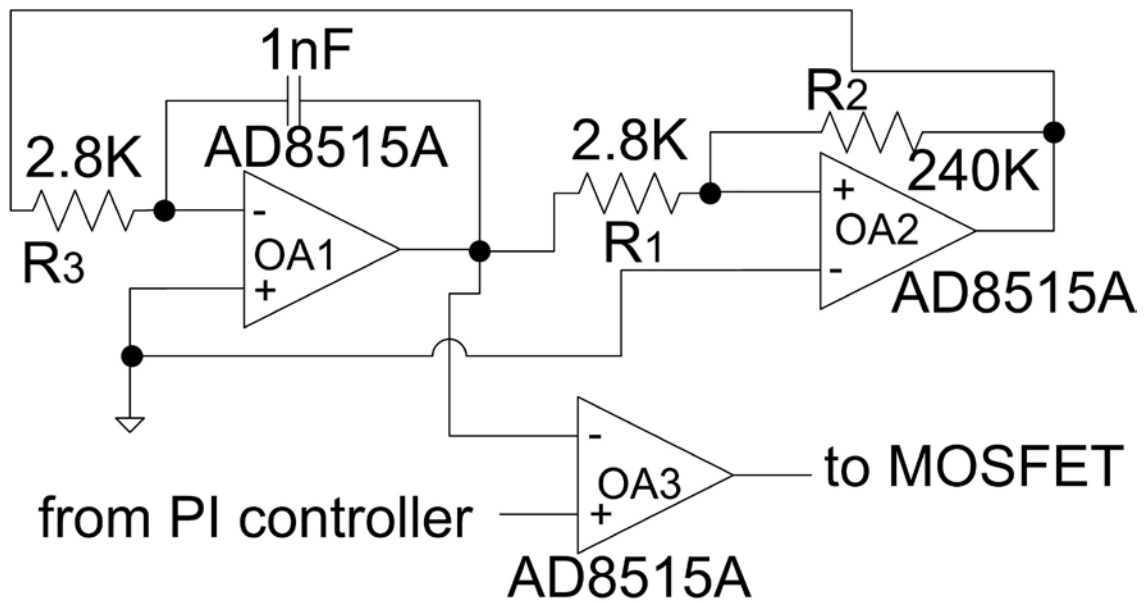


Fig. 4.13 The PWM modulator circuit.

The operational amplifiers OA1, OA2 and OA3 are configured as an integrator, a comparator with hysteresis and a comparator, respectively. The operational amplifiers OA1 and OA2 compose a triangular-wave generator. The operational amplifier OA3 compares the level of the PI controller output with the triangular-wave signal and produces the PWM control signal.

The triangular-wave maximum and minimum voltage levels, V_{TH} and V_{TL} , respectively, are given by:

$$V_{TH} = \frac{V_{CC}(R_1+R_2)}{2R_2} \quad (4.72)$$

$$V_{TL} = \frac{V_{CC}(R_1-R_2)}{2R_2} \quad (4.73)$$

where V_{CC} is the power supply voltage.

The peak-to-peak voltage is calculated by subtracting (4.73) from (4.72):

$$(4.66) - (4.67) = V_{TH} - V_{TL} = \frac{V_{CC}(R_1+R_2)}{2R_2} - \frac{V_{CC}(R_1-R_2)}{2R_2} = \frac{R_1}{R_2} V_{CC} \quad (4.74)$$

where $R_2 > R_1$.

The value of resistors R_1 and R_2 is determined by the ratio:

$$\frac{V_{TH}-V_{TL}}{V_{CC}} = \frac{R_1}{R_2} \quad (4.75)$$

The operating (switching) frequency of the PWM circuit is given by the following equation:

$$f = \frac{R_2}{4R_3CR_1} \Rightarrow \frac{4fR_1}{R_2} = \frac{1}{R_3C} \quad (4.76)$$

For a known desirable switching frequency, f , and available value of capacitor C , the value of resistor R_3 can be calculated using (4.76) by solving for R_3 . To reduce the power loss, large value resistors for R_1 and R_2 and micro-power high-frequency operational amplifiers are used to implement the PWM modulator circuit.

4.6 Battery overcharge protection

To avoid damage of the battery due to overcharging, an overcharge protection circuit has been designed and implemented. The overcharge protection circuit is illustrated in Fig. 4.14.

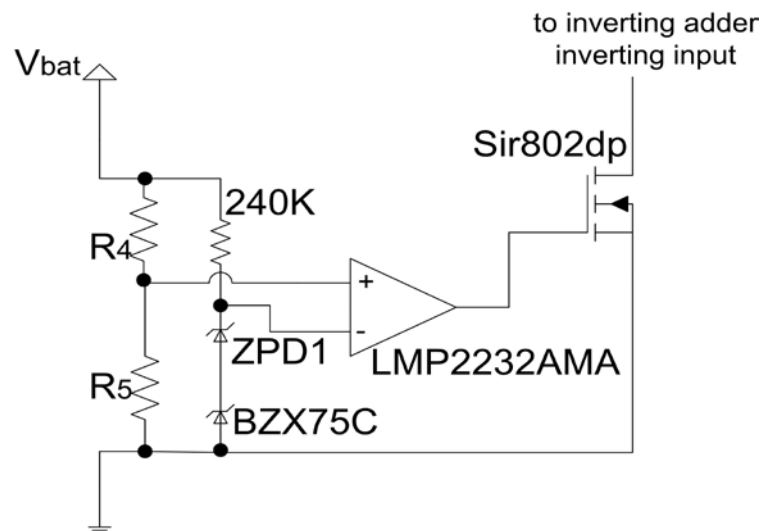


Fig. 4.14 Overcharge protection circuit.

Two zener diodes with part numbers ZPD1 and BZX75C, respectively, have been selected with nominal total voltage $V_z=2.1$ V. The values of resistors R_4 and R_5 of the

voltage divider are selected such that in case that the battery is fully charged (i.e. approximately $V_{\text{bat}}=2.8 \text{ V}$), the voltage produced by the voltage divider, V_{div} , is greater than the reference voltage produced by the zener diodes, V_z , which is also sufficient to drive the MOSFET gate. The comparator output equals V_{div} and the MOSFET short-circuits the inverting input of the inverting adder. As a consequence, the inverting adder output is set equal to the power supply voltage. The output of the inverting adder drives the inverting input of the PI controller, therefore, the PI controller output is set to zero. Thus, the duty cycle of the PWM signal is also set to zero and no power is transferred to the battery. In case that the accumulator voltage drops, such that V_z becomes greater than V_{div} , then the comparator output is set to zero. Therefore, the MOSFET is switched off and the normal operation of the control circuit continues, charging the battery according to the MPP energy produced by the TEG input source.

4.7 Power conditioning system total power dissipation

Based on the previous theoretical calculations and simulations about the P-V curves of the TEG devices presented in Chap. 2 and the power dissipation calculations for the individual components presented in this Chapter, the total power dissipation of the TEG power conditioning system can be analyzed by means of:

- the power conditioning system input and output power – input voltage curve,
- the efficiency ($\eta\%$) – power conditioning system output power curve and
- the power conditioning system input/output power at MPP – temperature difference curve,

for one TEG, as well as two TEG modules connected in series and in parallel for each value of ΔT . The efficiency, $\eta\%$, of a power conditioning system is given by the following equation:

$$\eta\% = \frac{P_{\text{out}}}{P_{\text{in}}} \cdot 100\% \quad (4.77)$$

4.7.1 Power conditioning system power dissipation for one TEG module

Figs. 4.15 - 4.17 illustrate the $P_{in} - V_{in}$, $P_{out} - V_{in}$ and $\eta\% - P_{out}$ curves for the same ΔT values as in Section 2.4.1, while Fig. 4.18 depicts the $P_{inMPP}/P_{outMPP} - \Delta T$ curve for one TEG.

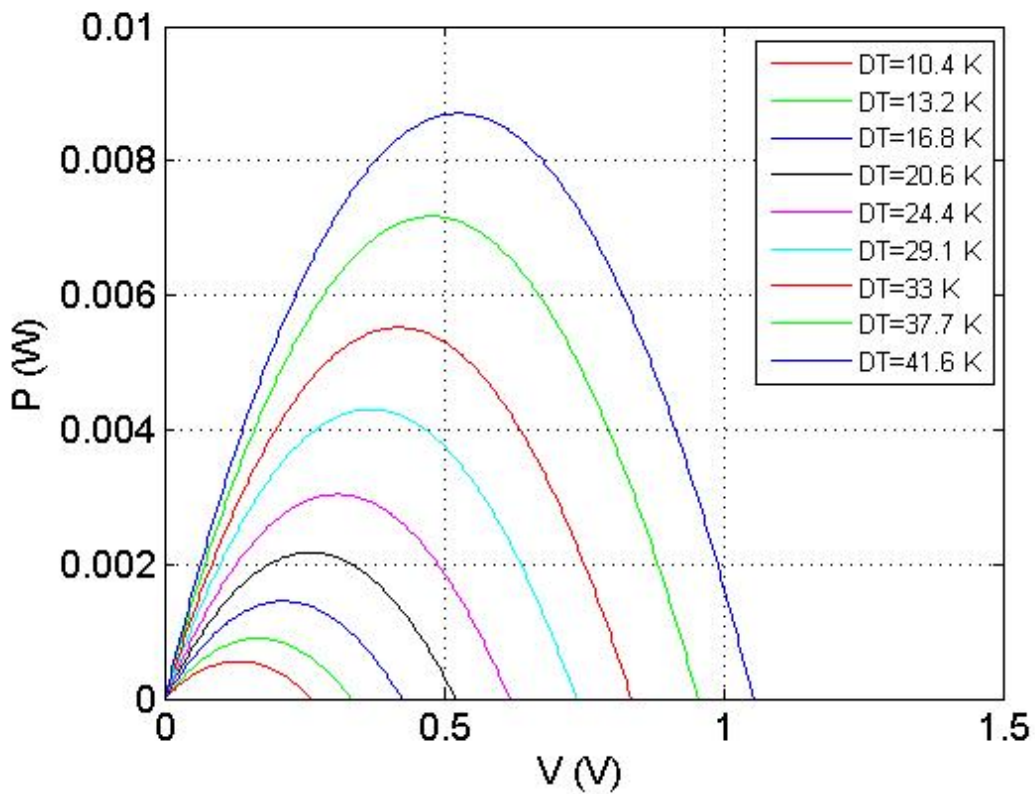


Fig. 4.15 Power conditioning system $P_{in} - V$ characteristics.

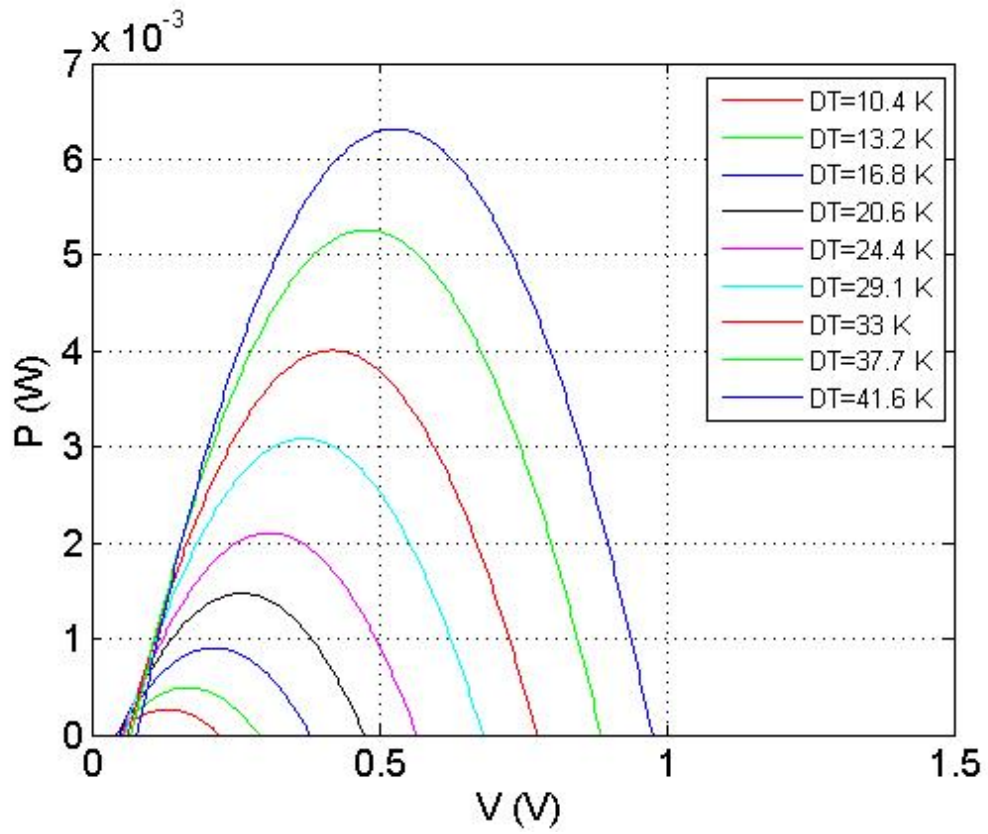


Fig. 4.16 Power conditioning system $P_{out} - V$ characteristics.

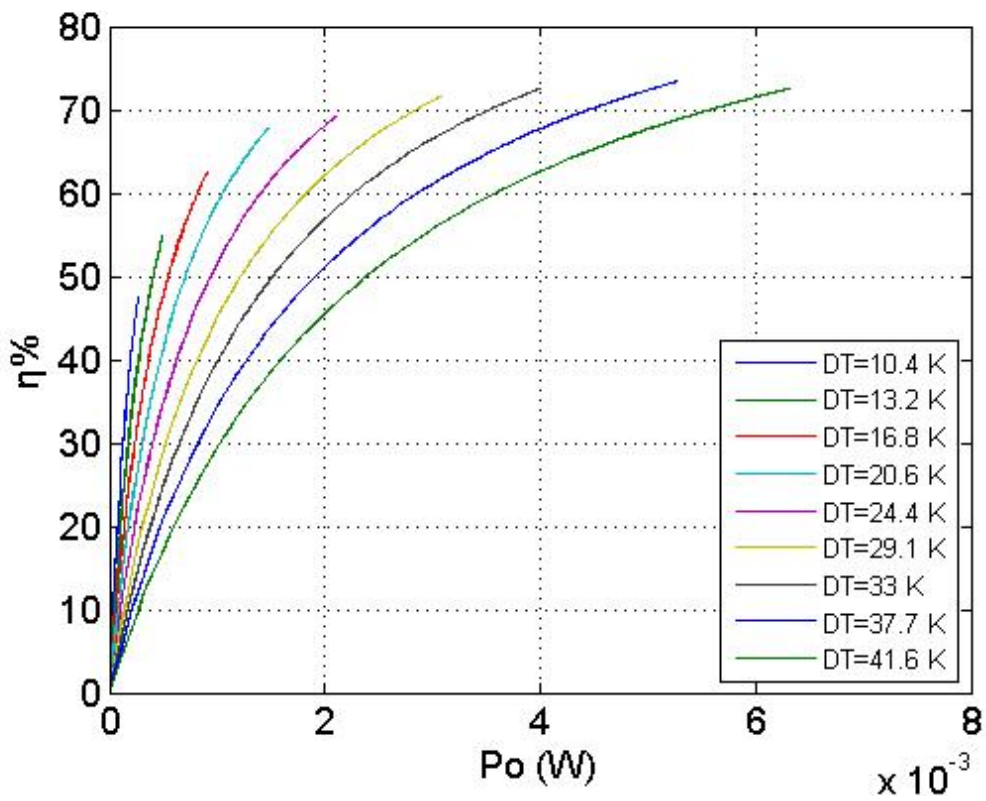


Fig. 4.17 Power conditioning system $\eta\% - P_{out}$ characteristics.

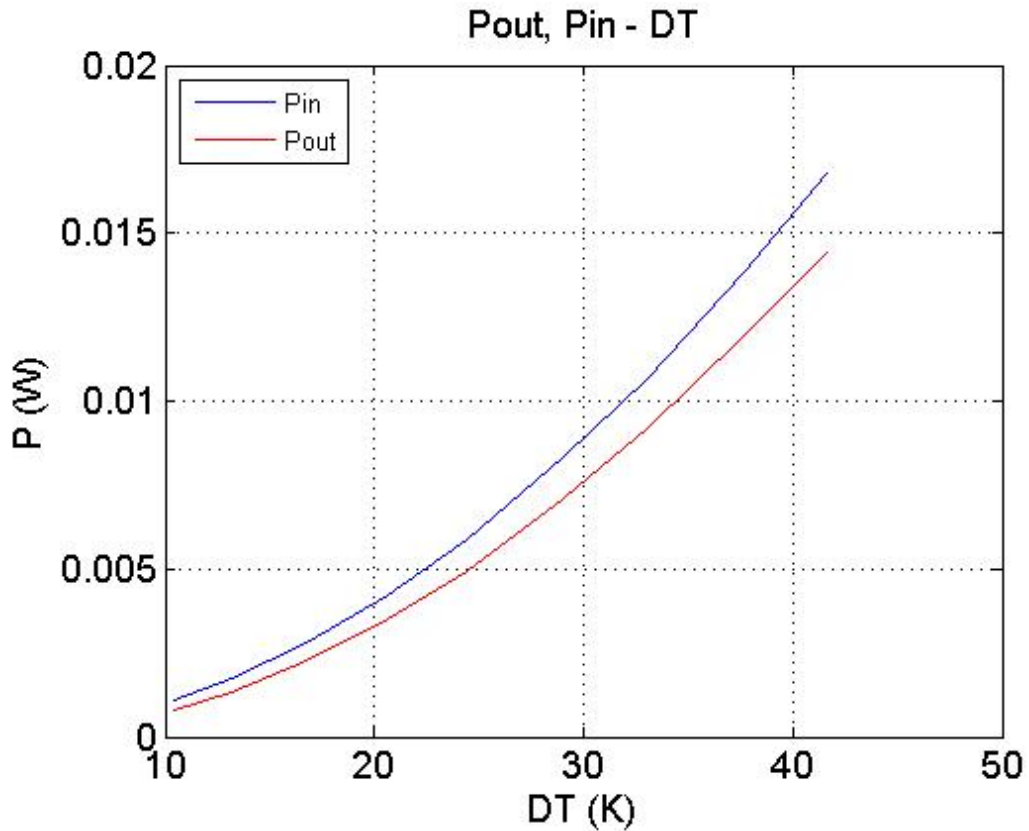


Fig. 4.18 Power conditioning system $P_{inMPP}/P_{outMPP} - \Delta T$ characteristics.

4.7.2 Power conditioning system power dissipation for two TEG modules connected in series

Figs. 4.19 - 4.21 present the $P_{in} - V_{in}$, $P_{out} - V_{in}$ and $\eta\% - P_{out}$ curves for the same ΔT values as in Section 2.4.2, while Fig. 4.22 illustrates the $P_{inMPP}/P_{outMPP} - \Delta T$ curve for two TEG modules connected in series.

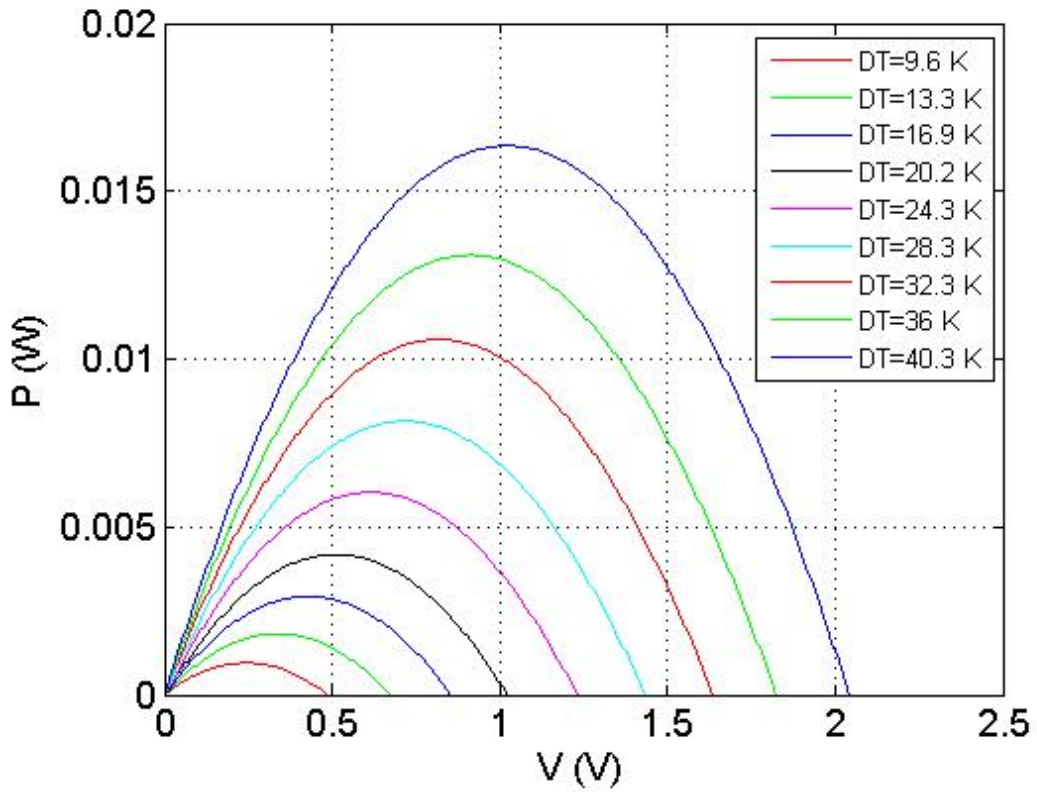


Fig. 4.19 Power conditioning system $P_{in} - V$ characteristics.

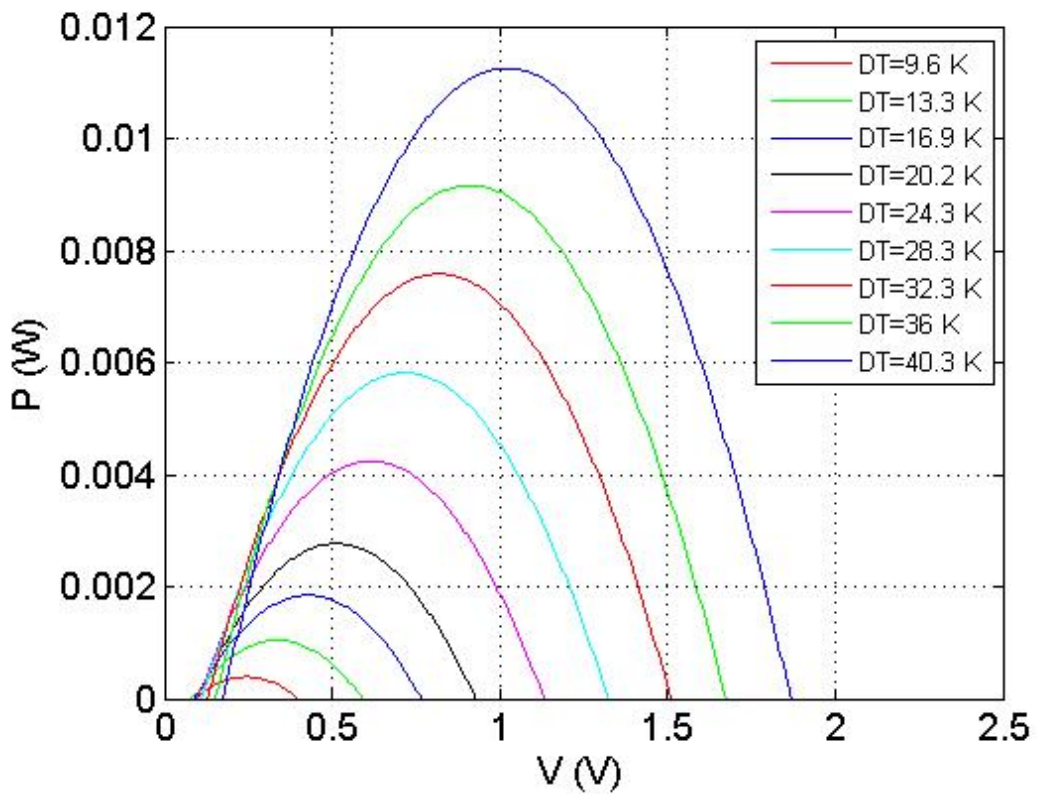


Fig. 4.20 Power conditioning system $P_{out} - V$ characteristics.

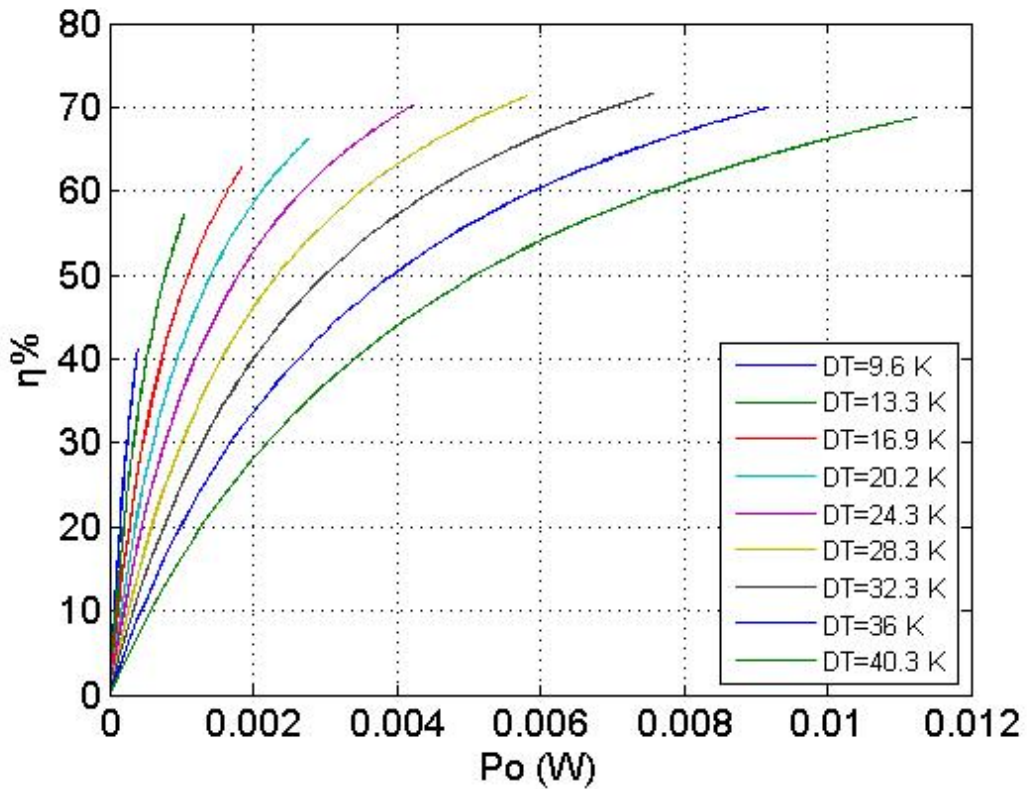


Fig. 4.21 Power conditioning system $\eta\%$ - P_{out} characteristics.

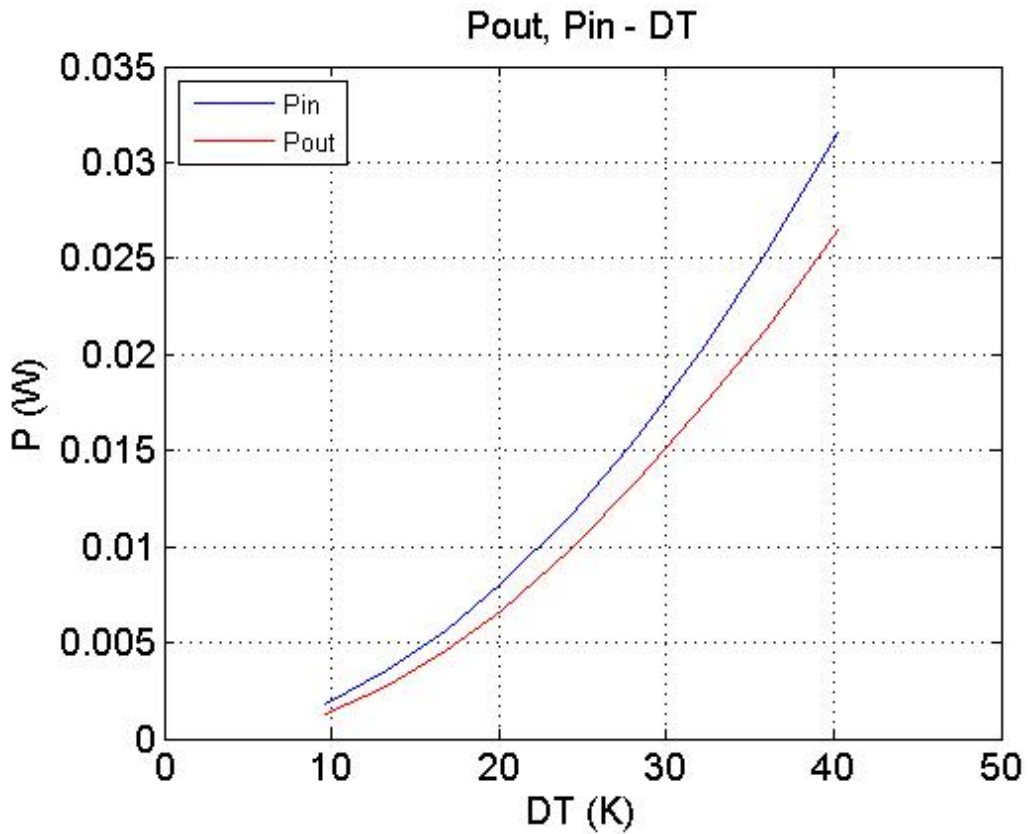


Fig. 4.22 Power conditioning system $P_{inMPP}/P_{outMPP} - \Delta T$ characteristics.

4.7.3 Power conditioning system power dissipation for two TEG modules connected in parallel

Figs. 4.23 - 4.25 illustrate the $P_{in} - V_{in}$, $P_{out} - V_{in}$ and $\eta\% - P_{out}$ curves for the same ΔT values as in Section 2.4.3, while Fig. 4.26 depicts the $P_{inMPP}/P_{outMPP} - \Delta T$ curve for two TEG modules connected in parallel.

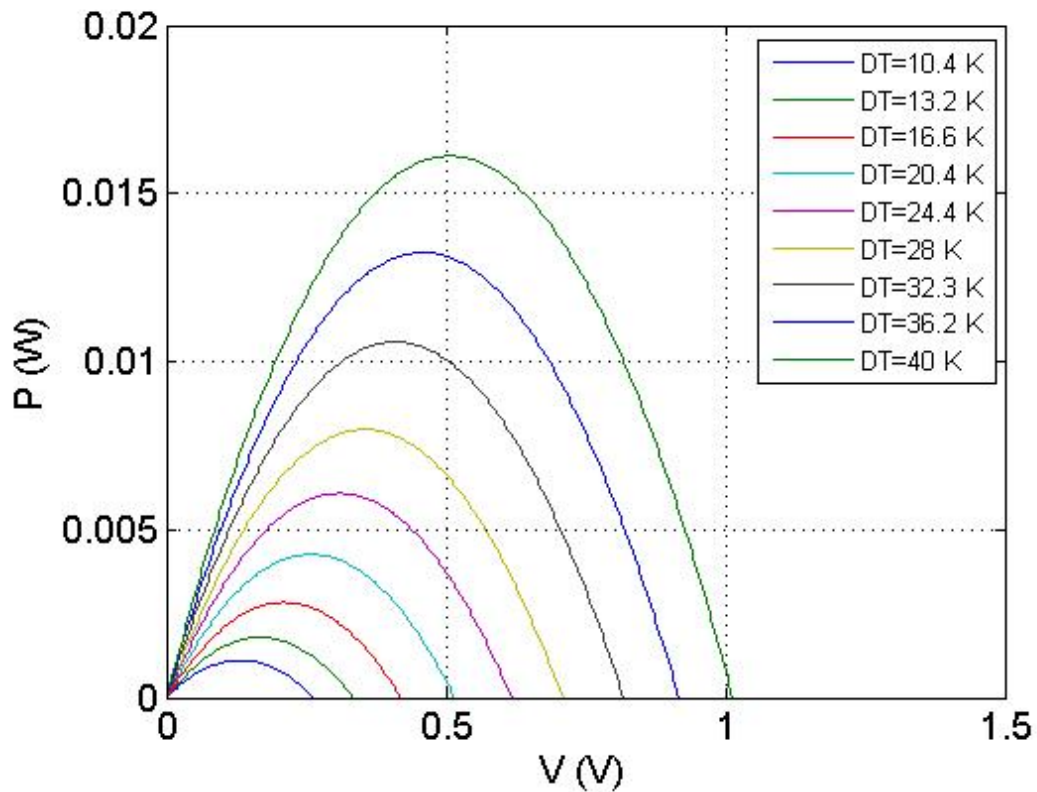


Fig. 4.23 Power conditioning system $P_{in} - V$ characteristics.

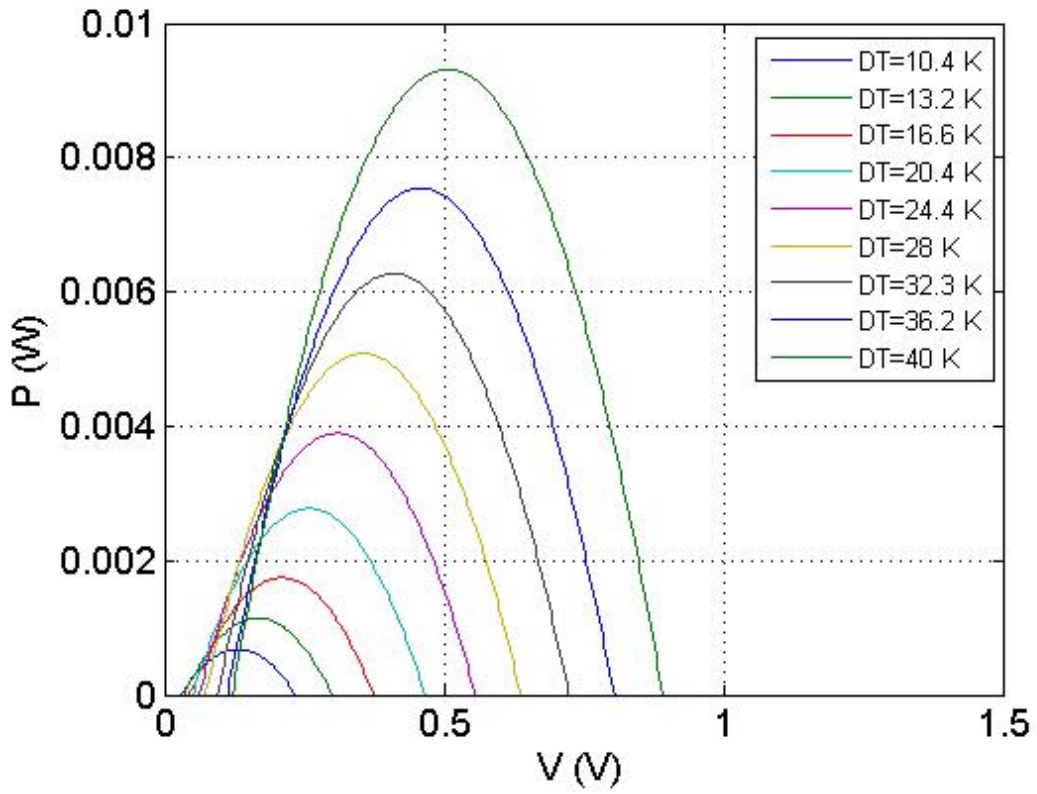


Fig. 4.24 Power conditioning system P_{out} - V characteristics.

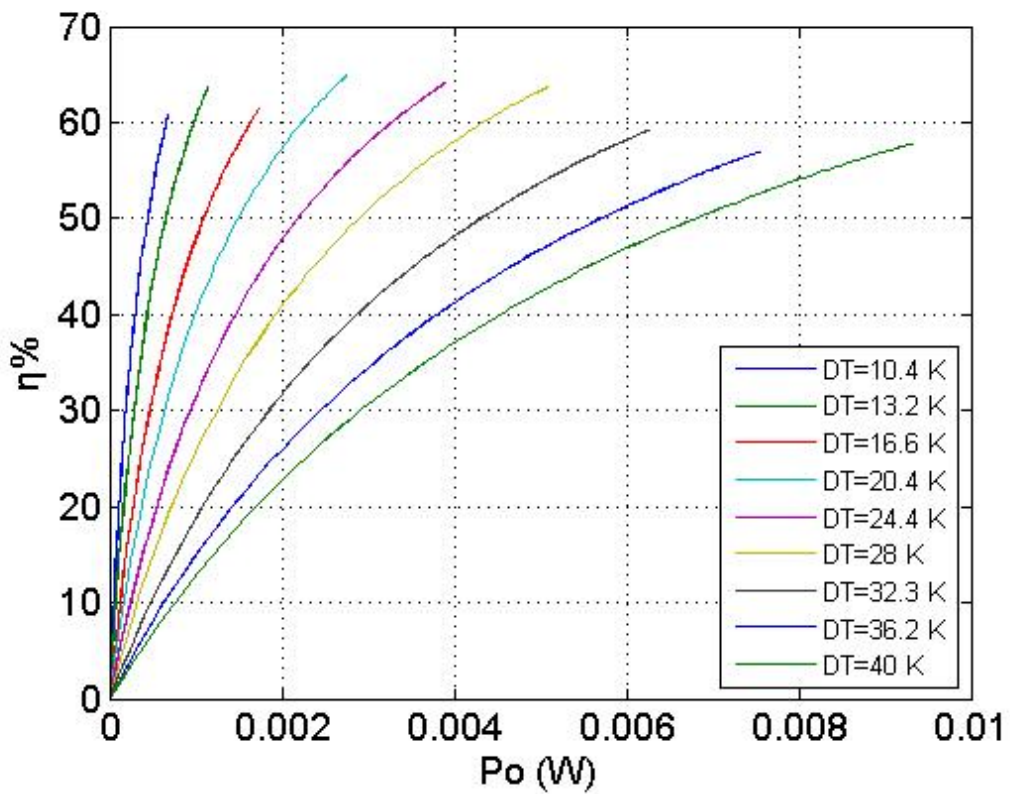


Fig. 4.25 Power conditioning system $\eta\%$ - P_{out} characteristics.

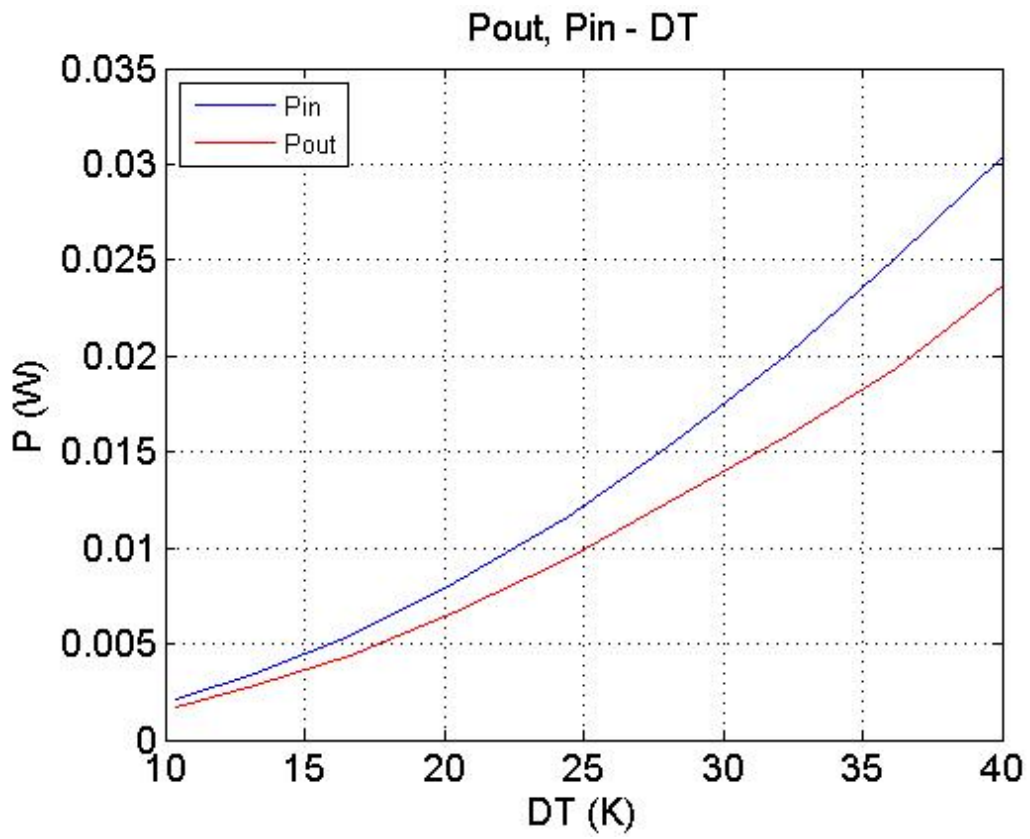


Fig. 4.26 Power conditioning system $P_{inMPP}/P_{outMPP} - \Delta T$ characteristics.

5.

Experimental Results

5.1 Introduction

In order to evaluate the performance of the system developed with the hardware setup described in Chap. 4 , the experimental prototype of the proposed system of Fig. 5.1 has been constructed.

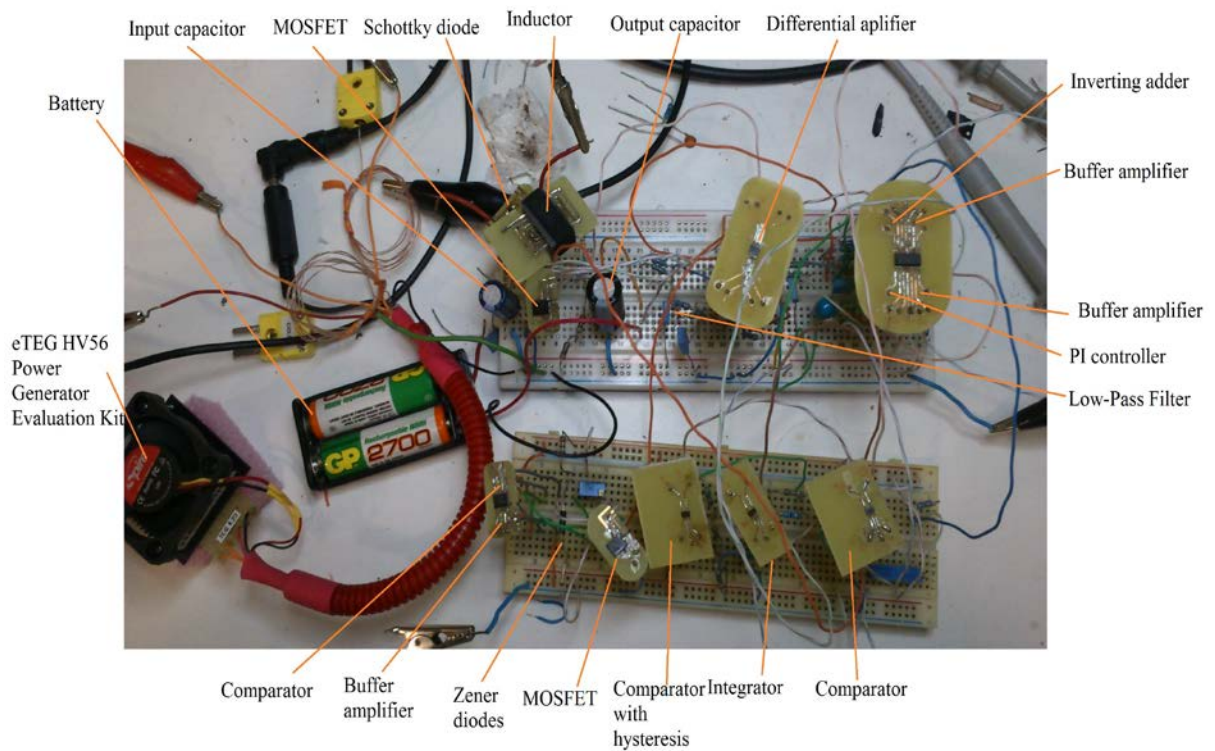


Fig. 5.1 The experimental prototype of the proposed MPPT system

5.2 Experiments

The performance of the system developed has been evaluated using three TEG energy source configurations, similarly to the simulated TEG sources:

- one eTEG HV56,
- two eTEG HV56 connected in series and
- two eTEG HV56 connected in parallel.

For each TEG configuration the following experiments at 293 °K ambient temperature have taken place:

1. having the duty cycle controlled by a frequency generator and with the TEG energy source connected at the input of the DC-DC boost converter, the I-V and P-V curves were measured for each temperature gradient, similarly to the simulations presented in Chap. 2, by altering the duty cycle value from 0 through 100%,
2. having the duty cycle controlled by a frequency generator and with a power supply unit connected to the input of the DC-DC boost converter, the efficiency-output power curve was measured, for input voltage of 0.2 V and 0.5 V, by altering the duty cycle values through the entire range of 0 to 100% and
3. having the system in fully operational mode, the MPP is measured for each temperature gradient similarly to the simulations presented in Chap. 2. Afterwards, a comparison was made between the theoretical MPP and the experimentally detected MPP by evaluating the corresponding percentage change, according to the following equation:

$$PC\% = \frac{MPP_{theory} - MPP_{experiment}}{MPP_{theory}} \cdot 100\% \quad (5.1)$$

5.2.1 Experimental results for one eTEG HV56

The experimental I-V curves of one eTEG HV56 for several temperature differences, similarly to the simulations in Chap. 2, obtained by the procedure described in previous section are illustrated in Fig 5.2. The corresponding experimental P-V curves are depicted in Fig 5.3.

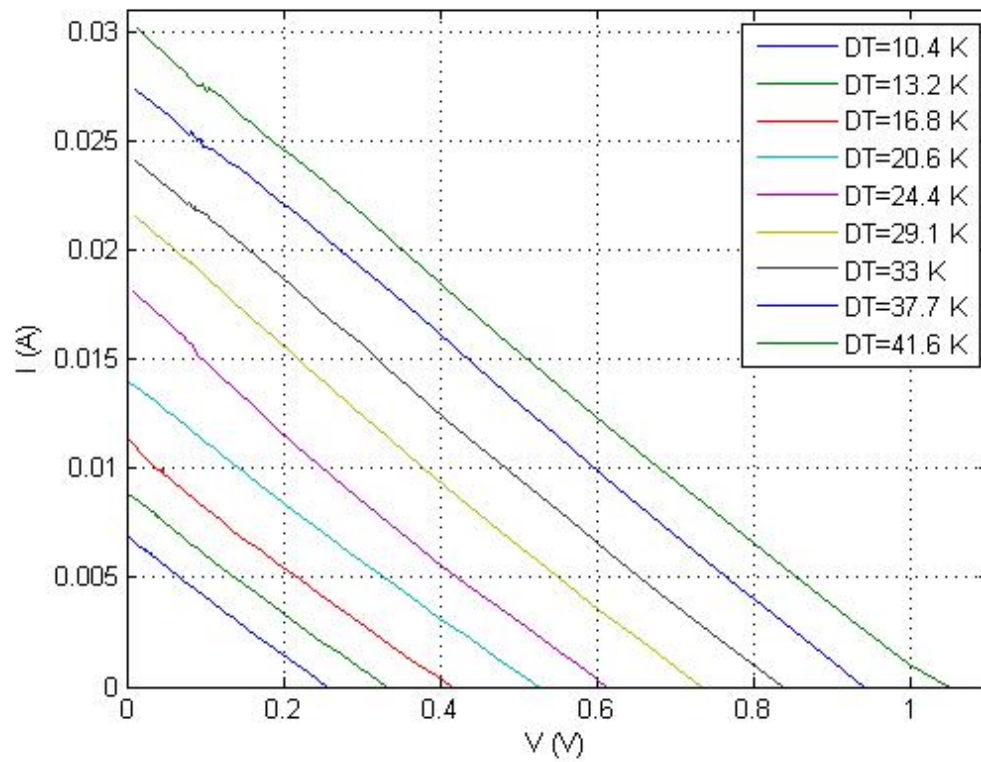


Fig. 5.2 Experimental *I-V* curves for one eTEG HV56.

The ripples observed in Fig 5.2 in the region between 0.08 V and 0.1 V, where the duty cycle value is close to 80%, are due to the non-linear characteristics of the circuit modules.

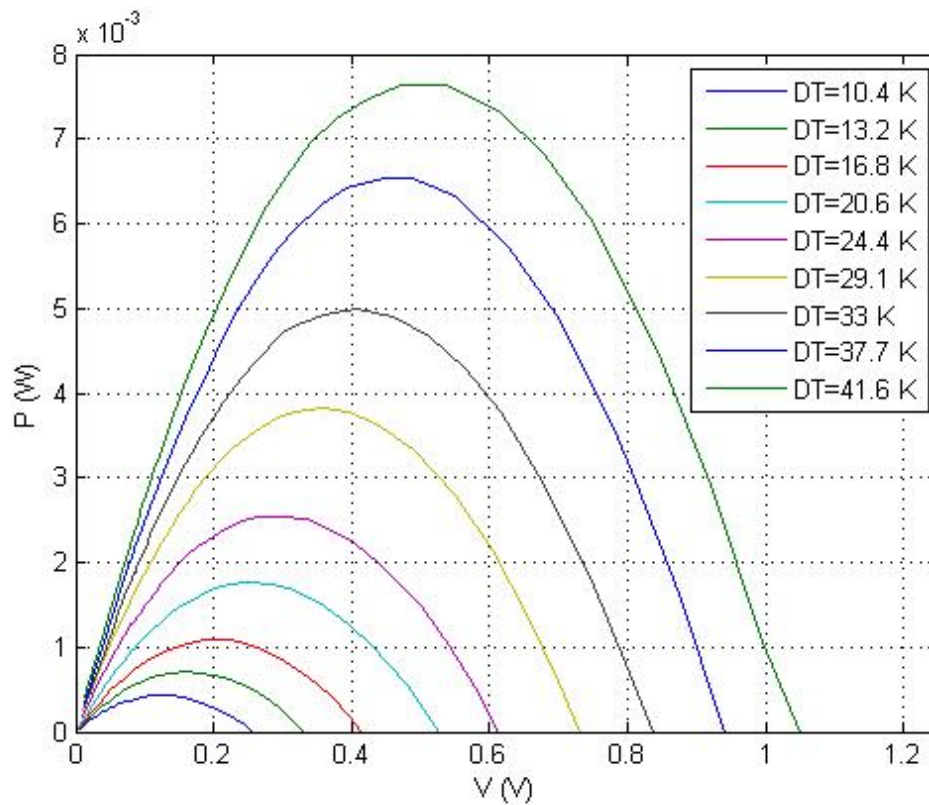


Fig. 5.3 Experimental P-V curves for one eTEG HV56.

The open-circuit voltage and short-circuit current of the TEG at various temperature differences have been measured, in order to obtain the corresponding P-V curves, before the TEG source is connected to the circuit for MPPT operation. The MPPs detected experimentally by the proposed MPPT system and the theoretical MPPs of the corresponding P-V curves are illustrated in Fig. 5.4.

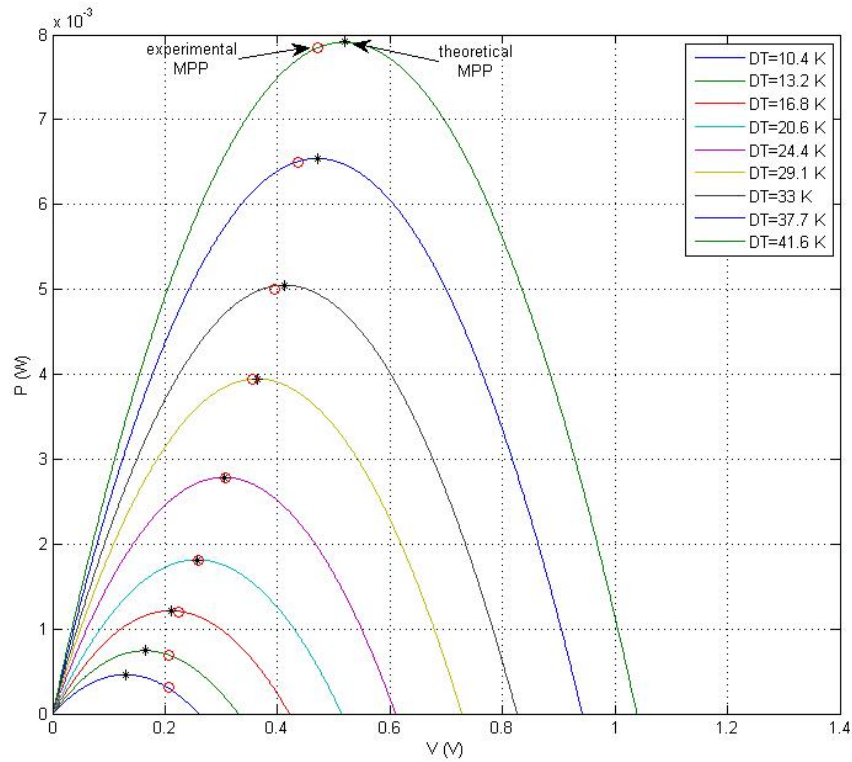


Fig. 5.4 The experimental MPPs derived by the proposed MPPT system and the corresponding theoretical MPPs for one eTEG HV56.

A deviation is observed between the experimental and theoretical values of MPP. This happens mainly due to the fact that the experimental MPP curve is a straight line, whereas the theoretical MPP curve, as seen in Fig. 1.2 is a curved line and cannot follow precisely the theoretical MPPs. Also, the largest value of percentage deviation is noticed for the two lowest temperature difference cases, where the power produced by the TEG source is very low.

The theoretical and experimental values of MPP, as well as the percentage deviation between the theoretical and experimental values are summarized in Table 5.1.

| Table 5.1 Theoretical and experimental MPP values for one TEG | | | |
|--|-----------------------------|------------------------------|---------------------------------|
| ΔT (°C) | Theoretical MPP (mW) | Experimental MPP (mW) | Percentage deviation (%) |
| 10.4 | 0.4608 | 0.3134 | 47.02 |
| 13.2 | 0.7429 | 0.6935 | 7.12 |
| 16.8 | 1.2133 | 1.205 | 0.69 |
| 20.6 | 1.814 | 1.8135 | 0.03 |
| 24.4 | 2.7854 | 2.776 | 0.34 |
| 29.1 | 3.9467 | 3.9376 | 0.23 |
| 33 | 5.0499 | 5.002 | 0.96 |
| 37.7 | 6.5422 | 6.4982 | 0.68 |
| 41.6 | 7.9133 | 7.8423 | 0.91 |

The percentage deviation between the theoretical and experimental MPPs is less than 1%, except for the lowest temperature gradients. As seen in Table 4.1, a temperature gradient of 10 °K is the lowest boundary of the HV56 thermal operation range.

5.2.2 Experimental results for two eTEG HV56 connected in series

The experimental I-V curves of two modules eTEG HV56 connected in series for several temperature gradients, similarly to the simulations presented in Chap. 2, are presented in Fig. 5.5. The corresponding experimental P-V curves of two modules eTEG HV56 connected in series are shown in Fig. 5.6.

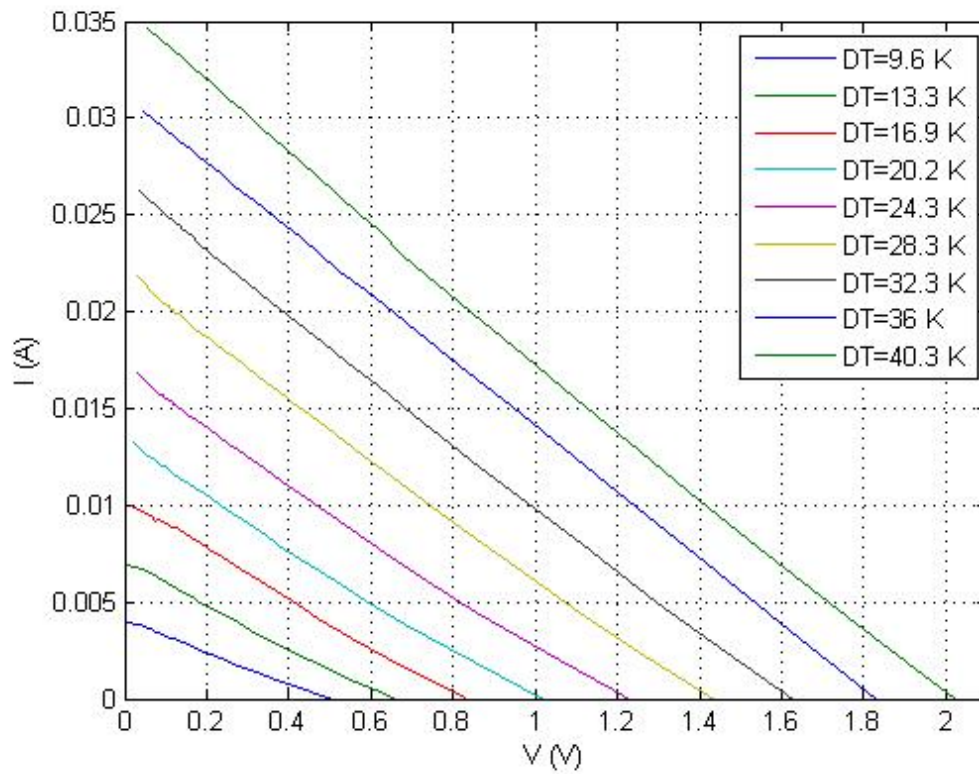


Fig. 5.5 Experimental I-V curves for two eTEG HV56 modules connected in series.

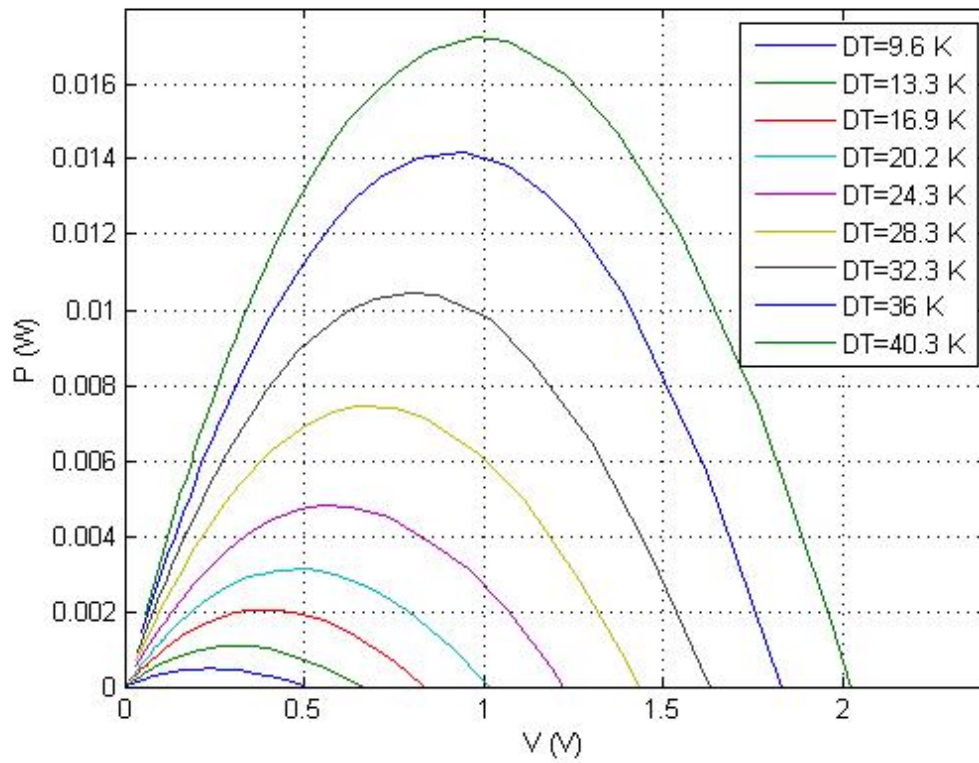


Fig. 5.6 Experimental P-V curves for two eTEG HV56 modules connected in series.

In this case, as shown in Fig. 5.5, the spikes are less and they are limited only in the lower region of the I-V curves (i.e. for low temperature gradient) where the power produced is very low, again at about 80% duty cycle. As the temperature gradient is increased, the power produced also increases and the modules of the power conditioning circuit operate linearly.

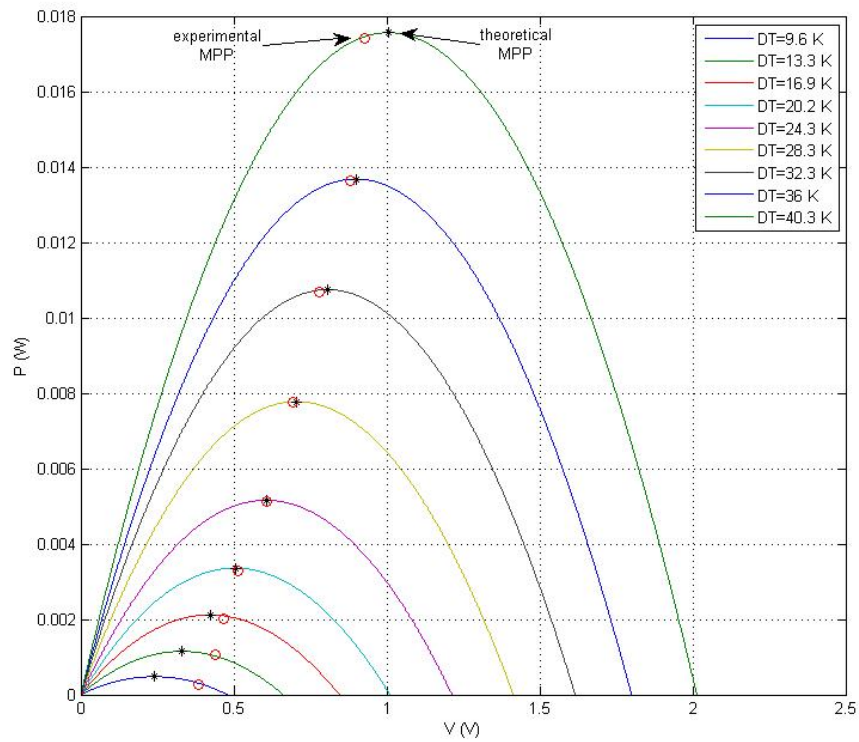


Fig. 5.7 The experimental MPPs derived by the proposed MPPT system and the corresponding theoretical MPPs for two eTEG HV56 modules connected in series.

The theoretical and experimental MPPs are shown in Fig. 5.7. The deviation is higher for low temperature gradients, due to the fact that the power produced is very low.

The theoretical MPP and experimental MPP values and the comparison between them by means of the percentage deviation are summarized in Table 5.2.

| ΔT (°C) | Theoretical MPP (mW) | Experimental MPP (mW) | Percentage deviation (%) |
|-----------------|----------------------|-----------------------|--------------------------|
| 9.6 | 0.482 | 0.2796 | 72.42 |
| 13.3 | 1.153 | 1.14 | 8.18 |
| 16.9 | 2.1192 | 2.0199 | 4.92 |
| 20.2 | 3.36 | 3.2806 | 2.42 |
| 24.3 | 5.1613 | 5.1207 | 0.79 |
| 28.3 | 7.777 | 7.7755 | 0.02 |
| 32.3 | 10.7464 | 10.6911 | 0.52 |
| 36 | 13.6194 | 13.6194 | 0.45 |
| 40.3 | 17.419 | 17.419 | 0.83 |

It is observed that with the exception of the first temperature gradient the percentage deviation between the theoretical and experimental MPP values remain below 5% and in most cases below 1%.

5.2.3 Experimental results for two eTEG HV56 connected in parallel

The experimental I-V curves of two modules eTEG HV56 connected in parallel for several temperature gradients, similarly to the simulations in presented Chap. 2, are presented in Fig. 5.8. The corresponding experimental P-V curves of two modules eTEG HV56 connected in parallel are shown in Fig. 5.9.

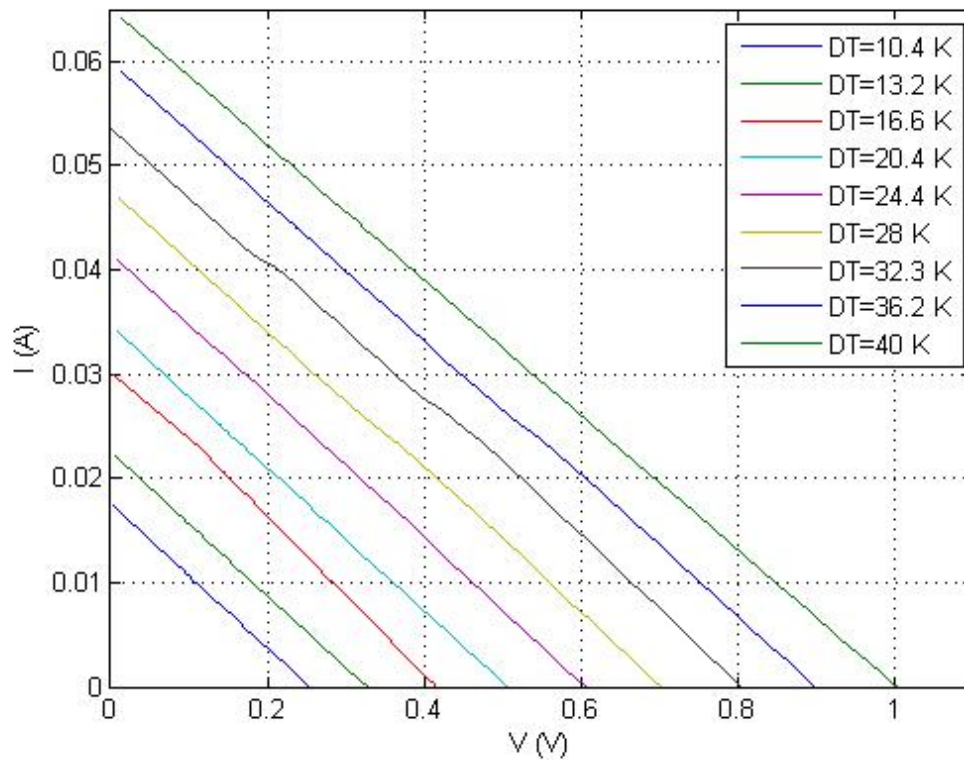


Fig. 5.8 Experimental I-V curves for two eTEG HV56 connected in parallel.

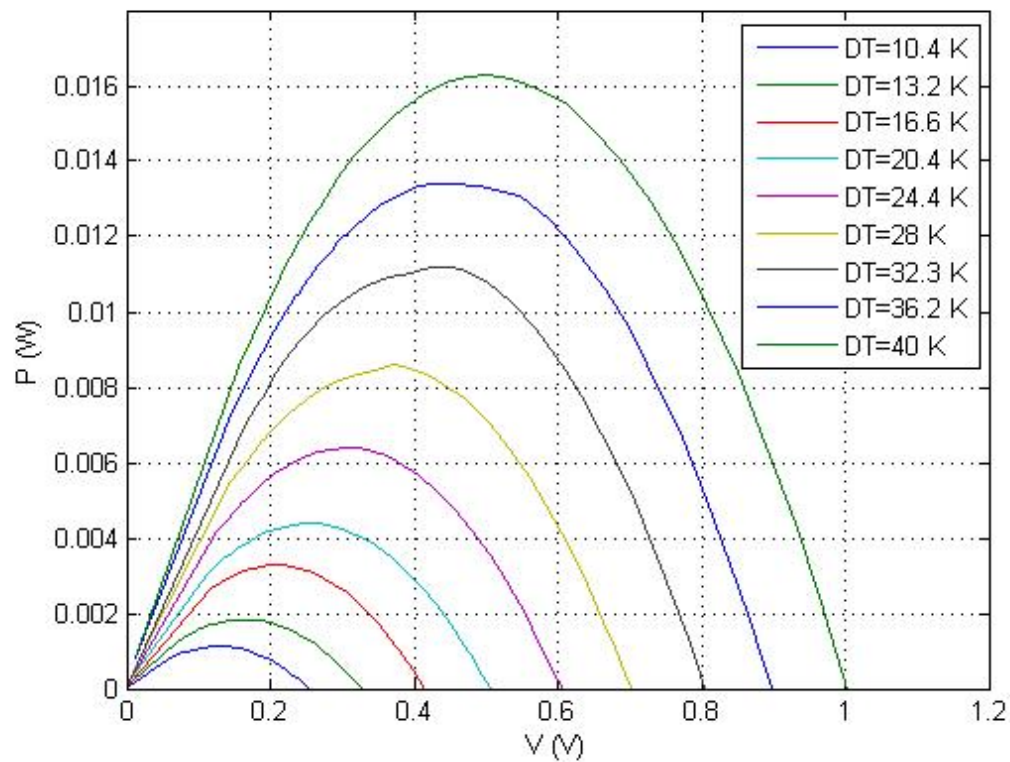


Fig. 5.9 Experimental P-V curves for two eTEG HV56 connected in parallel

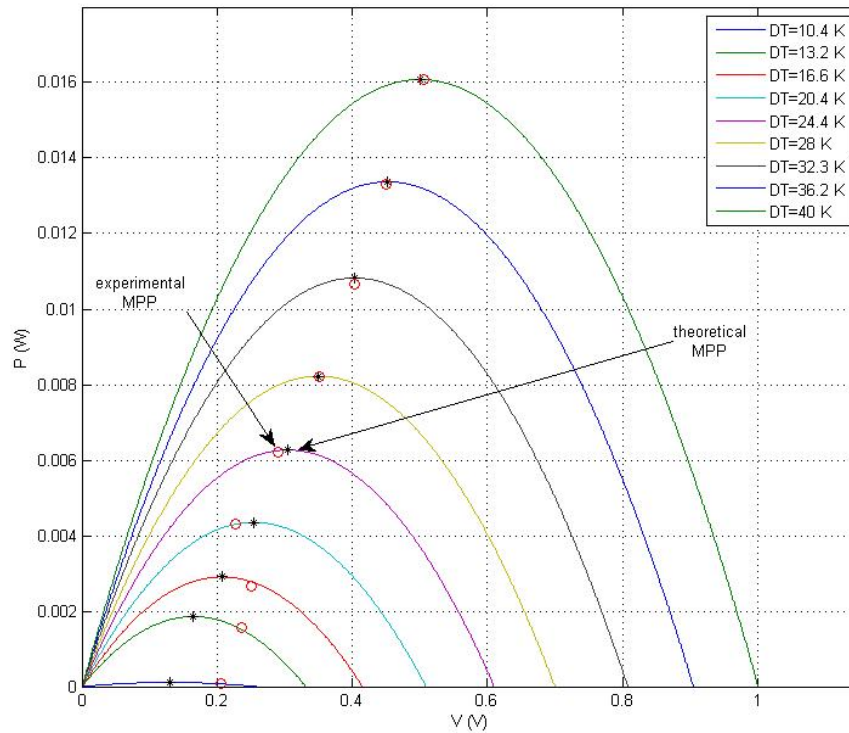


Fig. 5.10 The experimental MPPs derived by the proposed MPPT system and the corresponding theoretical MPPs for two eTEG HV56 modules connected in parallel.

The theoretical and experimental MPP values are presented Fig. 5.10. As in the one TEG and two TEG modules connected in series cases the deviation is higher for low values of the temperature gradient, due to the low power produced.

The theoretical and experimental MPP values and the corresponding percentage deviation are summarized in Table 5.3.

| ΔT ($^{\circ}\text{C}$) | Theoretical MPP (mW) | Experimental MPP (mW) | Percentage change (%) |
|-----------------------------------|-------------------------|--------------------------|-----------------------|
| 10.4 | 1.1267 | 0.7387 | 52.51 |
| 13.2 | 1.857 | 1.5694 | 18.32 |
| 16.6 | 2.905 | 2.65 | 9.62 |
| 20.4 | 4.3085 | 4.3085 | 1.01 |
| 24.4 | 6.1953 | 6.1953 | 1.17 |
| 28 | 8.2016 | 8.2016 | 0.29 |
| 32.3 | 10.6656 | 10.6656 | 1.48 |
| 36.2 | 13.3713 | 13.32 | 0.39 |
| 40 | 16.0836 | 16.0821 | 0.01 |

As seen in Table 5.3, except for the first three cases of temperature gradient, the percentage deviation remains below 1.5%.

5.2.4 I-V and P-V curves for two TEG modules at different ΔT

In order to investigate the operation of the proposed MPPT system for TEG modules at different temperature gradients, the corresponding I-V and P-V curves have been measured experimentally.

Two cases of two TEG modules connected in series are shown in Figs. 5.11 and 5.12. To acquire the I-V and P-V curves of the first case of the serial connection, $\Delta T=16.8^{\circ}\text{K}$ has been applied to the first TEG and $\Delta T=4.1^{\circ}\text{K}$ has been applied to the second TEG. Also, to obtain the I-V and P-V curves of the second case of the connection in series, $\Delta T=24.4^{\circ}\text{K}$ has been applied to the first TEG and $\Delta T=3.1^{\circ}\text{K}$ has been applied to the second TEG.

The I-V and P-V curves, respectively, of two TEG modules connected in parallel with different values of ΔT are presented in Figs 5.13 and 5.14. A temperature gradient of $\Delta T=20.6^{\circ}\text{K}$ has been applied to the first TEG and $\Delta T=3.1^{\circ}\text{K}$ has been applied to the second TEG.

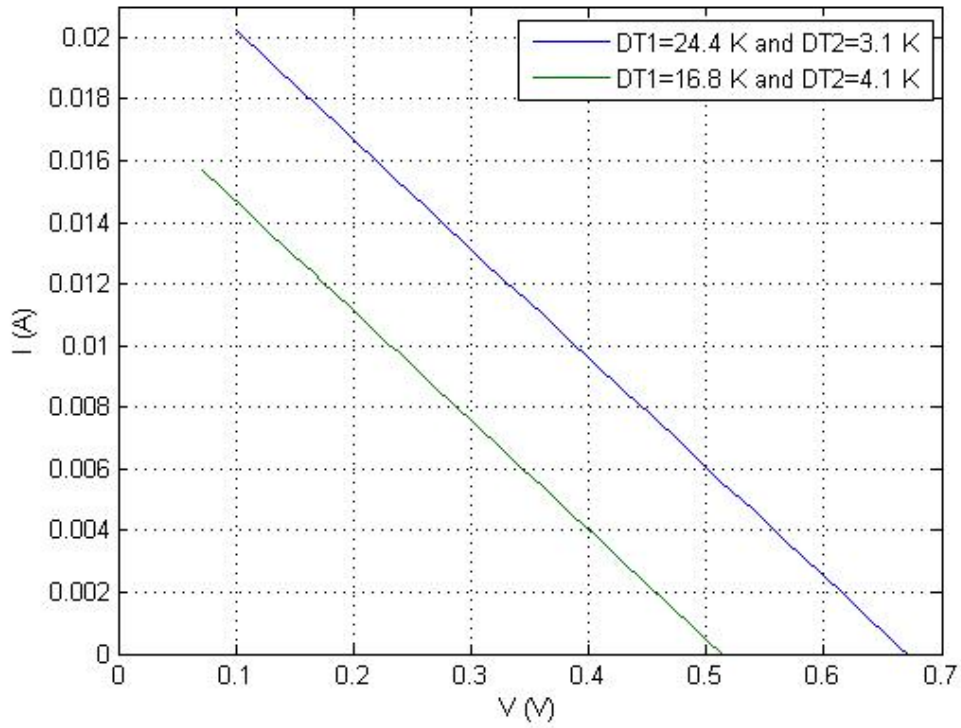


Fig. 5.11 I-V curves for two eTEG HV56 connected in series with different values of ΔT .

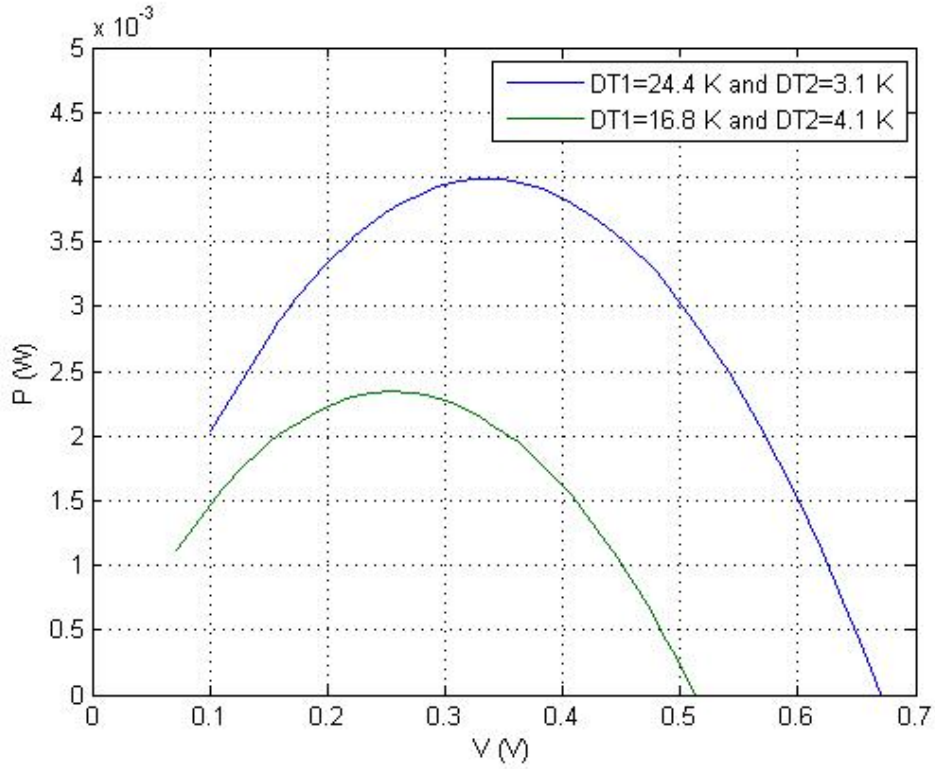


Fig. 5.12 P-V curves for two eTEG HV56 connected in series with different values of ΔT .

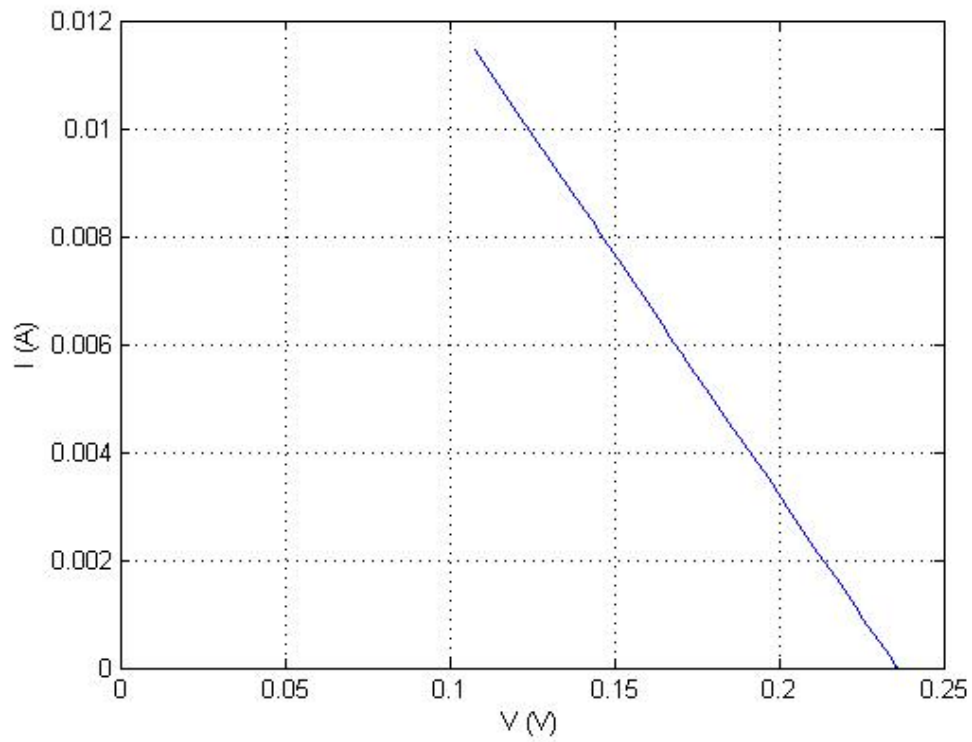


Fig. 5.13 I-V curve for two eTEG HV56 connected in parallel with different values of ΔT .

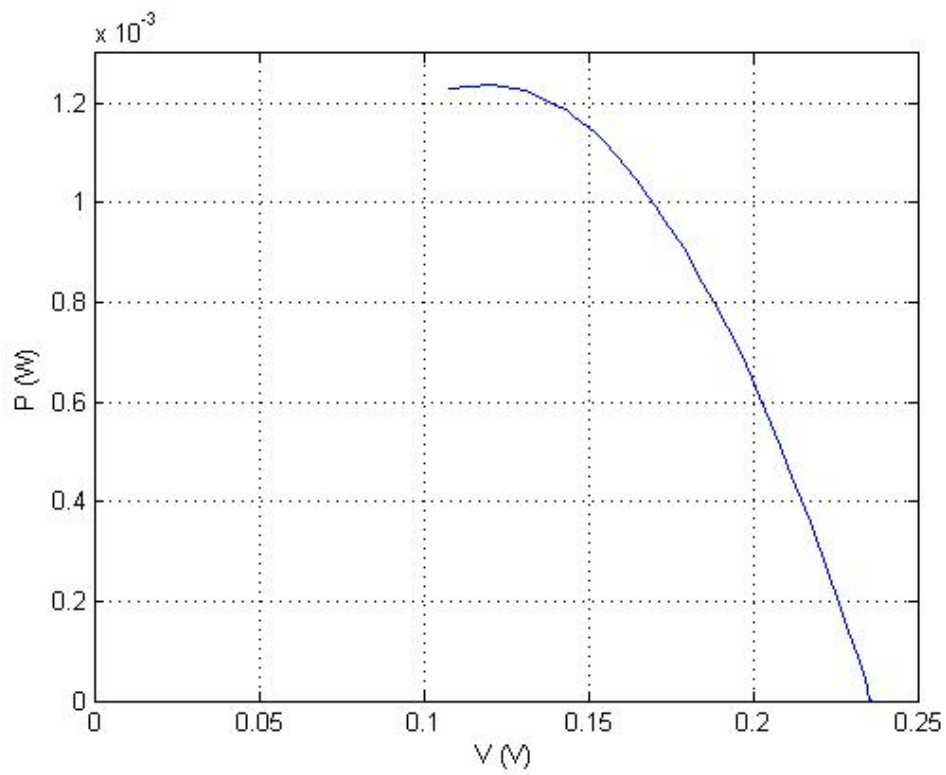


Fig. 5.14 P-V curve for two eTEG HV56 connected in parallel with different values of ΔT .

The specific values of ΔT have been selected to verify that the P-V curves in such cases are similar to the P-V curve of one TEG module, with absence of any local maximum. Thus, the proposed MPPT control algorithm is able to track the MPP in such cases too.

5.2.5 System efficiency

In order to evaluate the performance of the power conditioning system, the system efficiency has been measured. The input voltages of 0.2 V and 0.5 V have been selected as two random values of input voltage produced by the TEG modules when operating in the available thermal operating range. The efficiency, $\eta\%$, of a power conditioning system is given by the following equation:

$$\eta\% = \frac{P_{out}}{P_{in}} \cdot 100\% \quad (5.2)$$

The efficiency of the power conditioning system for 0.2 V and 0.5 V input voltage is shown in Figs 5.15 and 5.16, respectively.

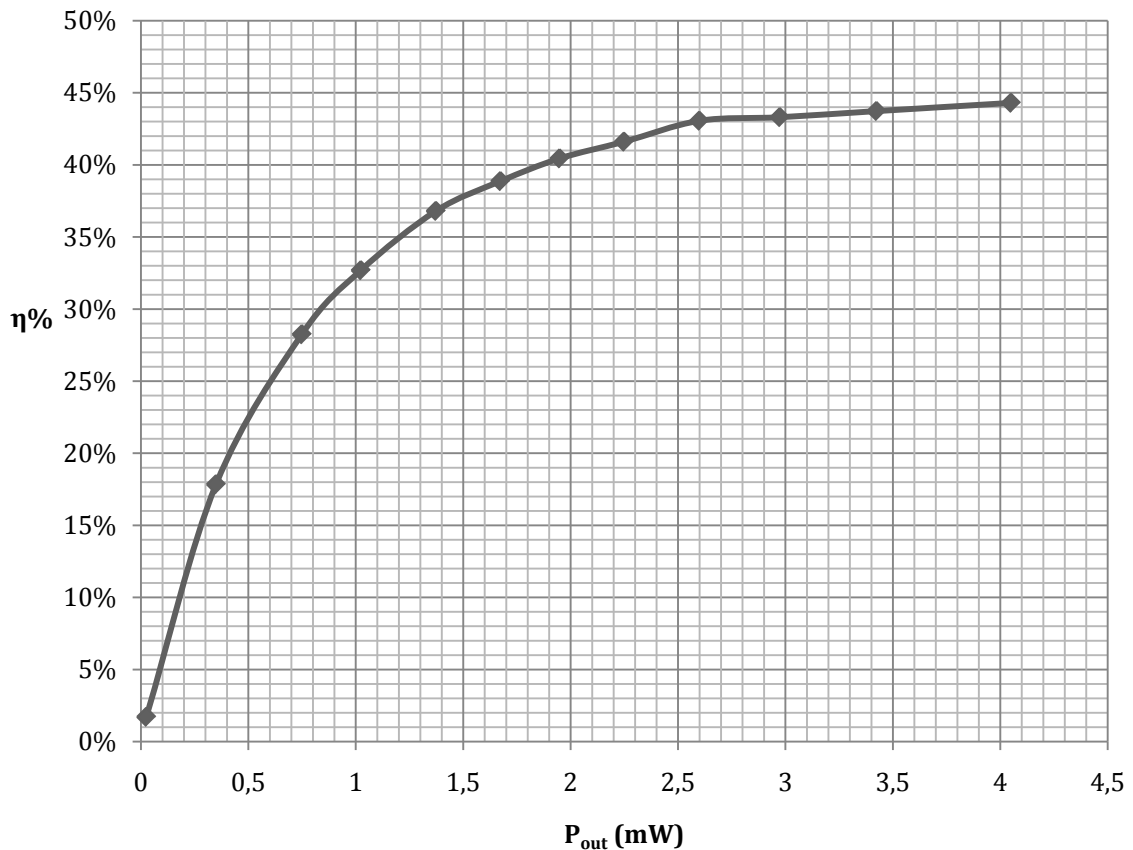


Fig. 5.15 The efficiency of the proposed power conditioning system for 0.2 V input voltage.

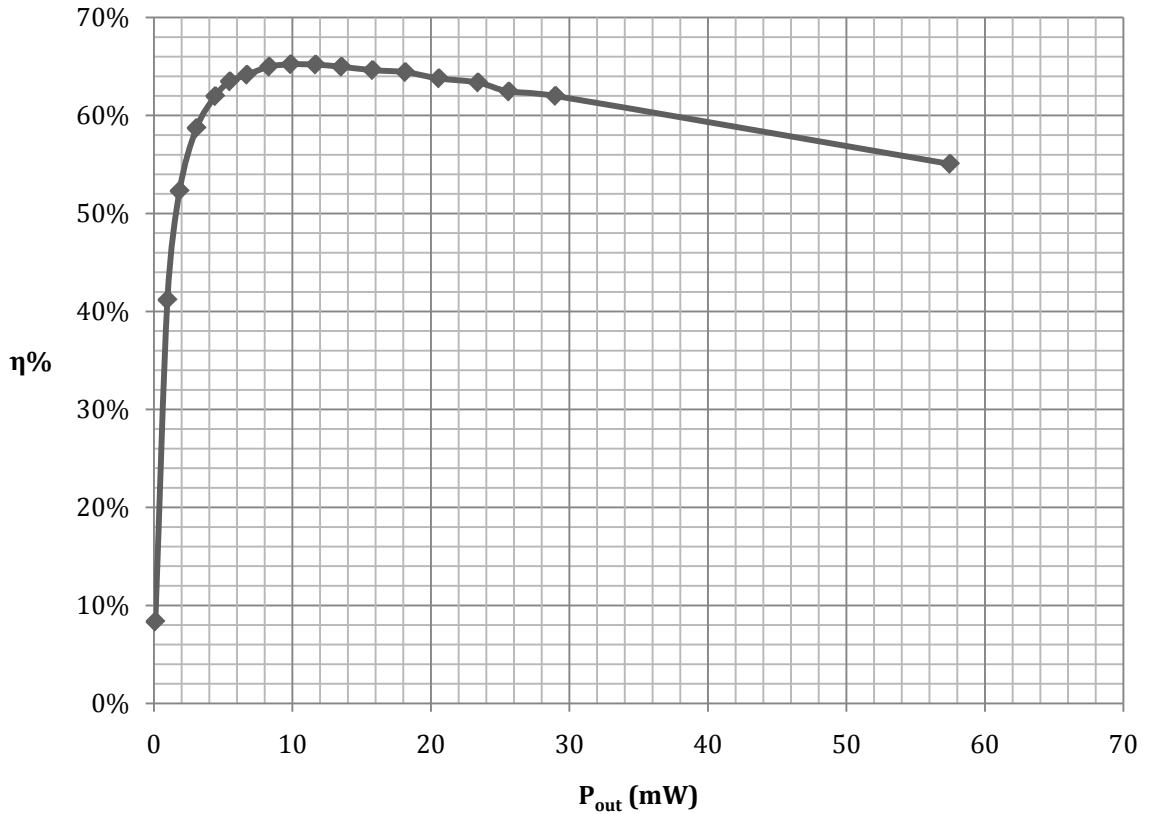


Fig. 5.16 The efficiency of the proposed power conditioning system for 0.5 V input voltage.

5.2.6 Oscilloscope waveforms

During the experiments, the following oscilloscope waveform snapshots were taken.

Fig. 5.17 shows the PWM control voltage waveform.

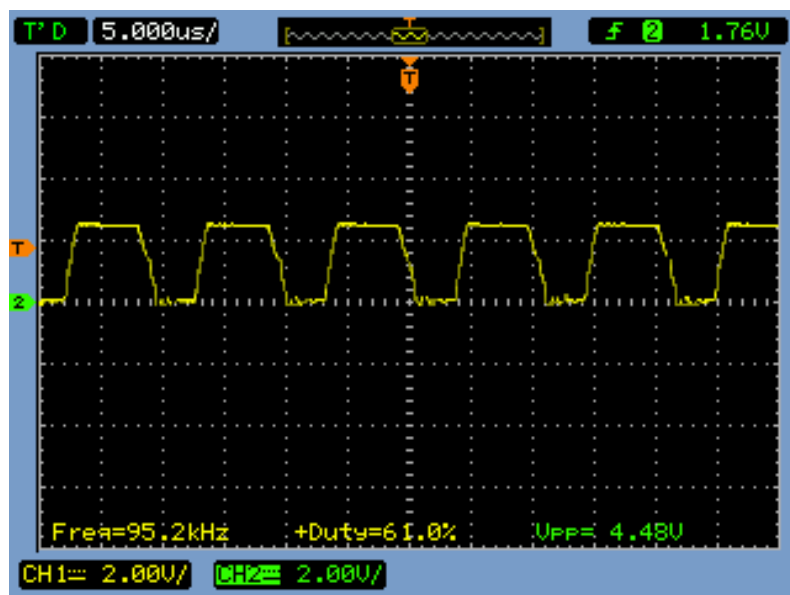


Fig. 5.17 Duty Cycle voltage.

The PWM control voltage waveform has been measured at the gate of the MOSFET.

Fig. 5.18 shows the DC-DC boost converter output and input voltage, which are sampled with CH1 and CH2, respectively.

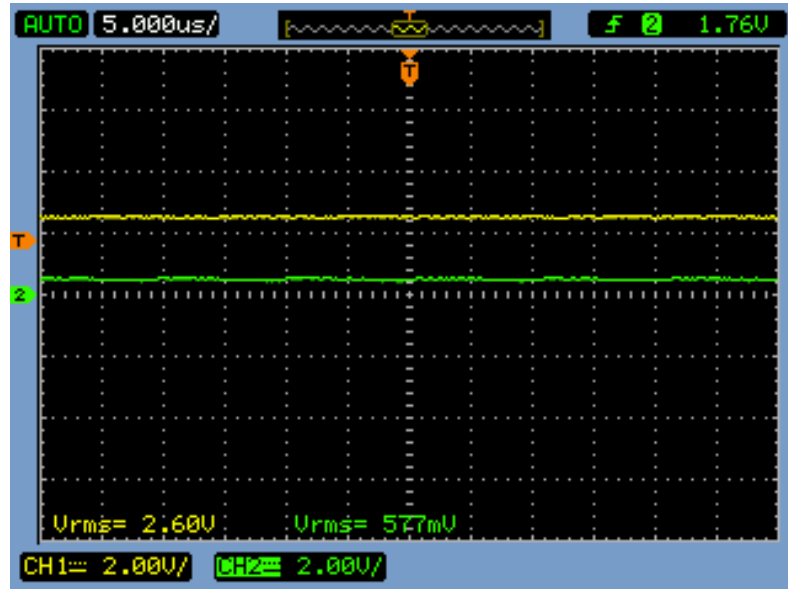


Fig. 5.18 Boost converter input and output voltage.

Fig. 5.19 shows the PI controller output voltage, which is sampled with CH1, and the inverting adder output voltage, which is sampled with CH2, at the MPP. As expected, the two voltage levels are equal, since the error signal of the feedback control loop tends to zero.

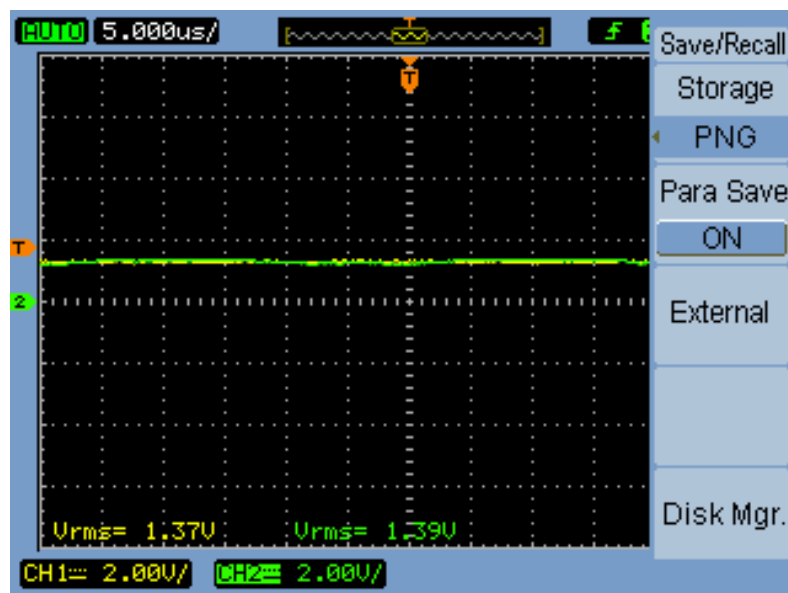


Fig. 5.19 PI controller output and inverting adder output.

Fig. 5.20 shows the PI controller and triangular-wave generator outputs.

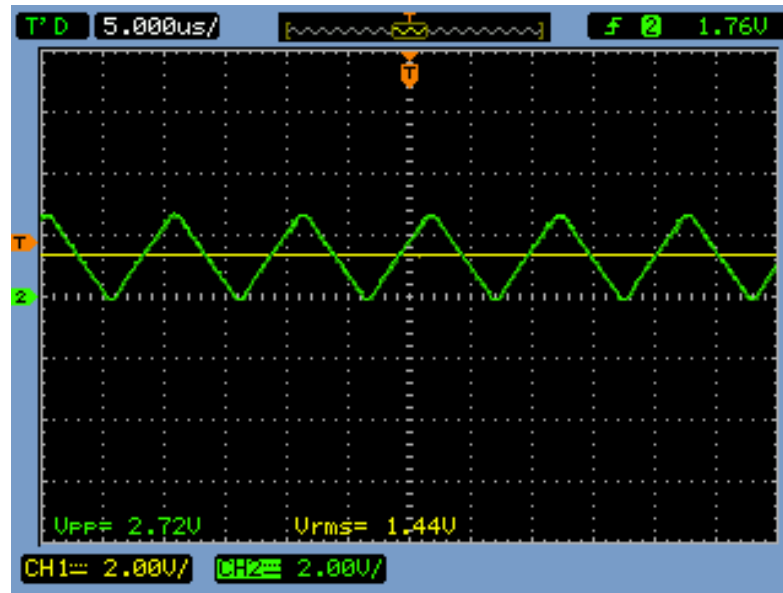


Fig. 5.20 PI controller and triangular-wave generator outputs.

In Fig. 5.20 the PI controller output is sampled with CH1 and the triangular-wave generator is sampled with CH2. The two signals are compared to produce the PWM signal of Fig. 5.17.

5.2.7 Control circuit power consumption

The power consumption of the proposed MPPT control circuit has been calculated by measuring the battery voltage and the current flow towards the control circuit. The battery voltage has been measured as $V_{\text{bat}}=2.7\text{ V}$ and the current as $I_{\text{ctrl}}=1.9\text{ mA}$. Hence, the power consumption has been calculated to be equal to $P_{\text{ctrl}}=5.13\text{ mW}$.

The developed system can be used in applications with temperature gradient (ΔT), which is applied on the TEG modules connected to the input of the system, which is adequately high, so that the power produced by the TEGs is higher than the power consumption of the control circuit (i.e. 5 mW), or employ configurations with more than one or two TEGs, as investigated in the present work, so that the battery can be charged. In this thesis the intention was to investigate the MPPT accuracy for power produced lower than 5 mW too.

6.

Conclusion

As mentioned in previous chapters, the research focusing on energy harvesting becomes more and more intensive, especially due to its suitability for small-scale applications. However, due to the low energy conversion efficiency, much work has yet to be done towards the development of more efficient systems, which are capable to utilize the most of an energy source. The performance of an energy conversion system can be upgraded by improving the conversion ratio and developing more efficient power transfer techniques. The aim of the current study is to examine and propose a novel power transfer system from the energy source to a load, in this case, a battery bank.

The model of the thermoelectric energy conversion system under study has been derived based on the basic characteristics of its structure and operation. Using the set of equations of the calculated model, the P-V, I-V, T_{cj} -V and T_{hj} -V curves have been plotted to determine the TEG behavior, in order to design the suitable power conversion system, which is based on the load matching theory.

The basic idea was to design a system with as small dimensions as possible and maximum efficiency. Thus, a model for each circuit module has been calculated and several simulations have been performed to select the most suitable modules out of many available in the market. In addition, a planar core inductor has been designed and constructed for a 100 kHz switching frequency, which proved to be the most efficient out of four possible frequencies. To maximize the efficiency of the system, the power consumption had to be minimized. Towards this direction, an analog microelectronic control system has been designed, consisting of low-voltage operational amplifiers.

The proposed MPPT system is pre-programmed to operate on a specific MPP locus in order to maximize the power transferred to the system load and it consists of a power conditioning system, a closed-loop control system and a PWM generator.

To evaluate the performance of the developed system, experiments for several temperature gradients were performed, for one TEG module, as well as two TEG modules connected in series and in parallel. The MPP tracking, when lower temperature gradients are applied to TEG, has lower efficiency due to the low values of the power produced. In contrast, for the MPP tracking at higher temperature gradients, within the thermal operating range of the available evaluation kit, the deviation between the TEG operating points and the theoretical MPP is less than 1% in most cases investigated.

In [3], a comparison is performed between three MPPT methods for TEGs providing information about the efficiency of the system using the following equation:

$$\eta_x = \frac{P_{MPP,experimental}}{P_{MPP,theoretical}} \cdot 100\% \quad (6.1)$$

where $P_{MPP,experimental}$ refers to the minimum, P_{min} , and the maximum, P_{max} , output power as a result of the oscillation of the operating point around the MPP or stopping at a nearby point for P&O and INC algorithms as described in Chap. 3. For INC and Fractional Short-Circuit methods the P_{min} and P_{max} values are the same.

Extracting MPPT efficiency values from [3] for $V_{oc}=2$ V for each MPPT method and comparing with the proposed method for two TEG modules connected in series and $\Delta T=40.3$ °K, Table 6.1 has been constructed, summarizing the performance of these MPPT methods. The minimum, $\eta(\%)_{min}$, and maximum, $\eta(\%)_{max}$, efficiencies in Table 6.1 result from equation (6.1) where $P_{MPP,experimental}$ is P_{min} and P_{max} , respectively.

| Method | $\eta(\%)_{min}$ | $\eta(\%)_{max}$ |
|--------------------------|------------------------------------|------------------------------------|
| Perturb and Observe | 32.3 | 91.8 |
| Incremental Conductance | 91.8 | 91.8 |
| Fractional Short-Circuit | 90.1 | 90.1 |
| Proposed Method | 99.17 | 99.17 |

Apart from better results in reaching the TEG MPP, compared to the methods mentioned in Chap. 3, the proposed method also employs a less power consuming control circuit, achieving better efficiency. Table 6.2 illustrates the comparison of power consumption for each MPPT method. In order to compare the methods, it was assumed that the methods described in Chap. 3 used the same types of analog devices to implement the control circuit, as those used in the proposed MPPT system.

| Table 6.2 Comparison of the power consumed by the proposed system with the estimated power consumption of three widely used MPPT methods for TEGs. | |
|---|--------------------------------|
| Method | Power consumption (mW) |
| Perturb and Observe | 9.5-12 |
| Incremental Conductance | 13.5-17 |
| Fractional Short-Circuit | Similar to the proposed method |
| Proposed Method | 5.13 |

As shown in Table 6.2, the deviation in power consumption among the proposed and the past-proposed MPPT methods is significant. This happens due to the fact that the proposed method requires less complex computations to reach the TEG MPP.

The implemented system is a complete energy harvesting system for TEG devices. Future work could focus on adapting the system for other types of batteries, the use of a supercapacitor-based storage unit of the system, as well as the extension of the proposed control circuit to regulate the battery/supercapacitor charging process.

References

- [1] L. Chen, D. Cao, Yi Huang and F. Z.Peng, "Modeling and power conditioning for thermoelectric generation," IEEE Power Electronics Specialists Conference, pp. 1098-1103, June 2008.
- [2] S. Dalola, M. Ferrari, V. Ferrari, M. Guizzetti, D. Marioli and A. Taroni, "Characterization of thermoelectric modules for powering autonomous sensors," IEEE Trans. Instrum. Meas., vol. 58, no 1, pp. 99-107, Jan. 2009.
- [3] I. Laird, H. Lovatt, N. Savvides, D. Lu, V.G. Agelidis, "Comparative study of maximum power point tracking algorithms for thermoelectric generators," Australasian Universities Power Engineering Conference, pp. 1-6, 2008.
- [4] Yu Chuang and K. T. Chau, "Thermoelectric automotive waste heat energy recovery using maximum power point tracking," Energy Conversion and Management, vol. 50, no. 6, pp. 1506-1512, June 2009.
- [5] A. Mirocha and P. Dziurdzia, "Improved electrothermal model of the thermoelectric generator implemented in SPICE," Signals and Electronic Systems, Sept. 2008.
- [6] S. Kasap, "Thermoelectric effects in metals: thermocouples," e-booklet, 1997-2001.
- [7] S. Cho, N. Kim, S. Park and S. Kim, "A coreless maximum power point tracking circuit of thermoelectric generators for battery charging systems," IEEE Solid State Circuits Conference, vol.9, no. 6, pp. 1-4, 2010.
- [8] L. Mateu, M. Pollak and P. Spies, "Analog Maximum Power Point Circuit Applied to Thermogenerators," PowerMEMS, pp.461-464, Nov. 2008.
- [9] J. Eakburanawat and I. Boonyaroonate, "Development of a thermoelectric battery-charger with microcontroller-based maximum power point tracking technique," Applied Energy, vol. 83, no. 7, pp687-704, 2006.
- [10] A. Yafaoui, B. Wu and R. Cheung, "Implementation of maximum power point tracking algorithm for residential photovoltaic systems," 2nd Canadian Solar Building Conference, June 2007.
- [11] T. Eswam, and P. L. Chapman, "Comparison of photovoltaic array maximum power point tracking techniques," IEEE transactions on Energy Conversion, vol. 22, no. 2, pp. 439-449, June 2007.

- [12] B. Hauke, "Basic Calculation of a Boost Converter's Power Stage," Texas Instruments, Application Report, Nov 2009.
- [13] K. Smedley, Y. Sun, O. Egterafi, E. Matthes and R. Tikia, "Industrial & Power Electronics EECS 166/267A – Boost Converter Lab," University of California, 2005.
- [14] B. R. Reemmer, "DC to DC conversion: Boost Converter Design," 2007. <http://roboturk.googlecode.com/files/DC%20to%20DC%20Conversion.pdf>.
- [15] Xu Huang, "Selection Guide of SiC Schottky Diode in CCM PFC Applications," 2006. <http://scn.cree.com/products/pdf/CPWR-AN05-.pdf>.
- [16] N. Mohan, W. P. Robbin and T. M. Undeland. "Power electronics: converters, applications, and design, " Wiley, 2007.
- [17] J. Brown, "Modeling the switching performance of a MOSFET in the high side of a non-isolated buck converter," IEEE Transactions on Power Electronics, vol. 21, no. 1, pp. 3-10, Jan 2006.
- [18] D. Graovac, M. Purschel and A. Kiep, "MOSFET power losses calculation using the data-sheet parameters," *Application Note 1*, July 2006.
- [19] Nextreme. "eTEGTM HV56 Power Generator." http://www.nextreme.com/media/pdf/techspecs/Nextreme_eTEG_HV56_Data_Sheet.pdf.
- [20] Nextreme. "eTEGTM HV56 Power Generator Evaluation Kit." http://www.nextreme.com/media/pdf/techspecs/Nextreme_eTEG_Evaluation_Kit_Data_Sheet.pdf.
- [21] Nextreme. "eTEGTM HV56 Power Generator Evaluation Kit Application Notes." http://www.nextreme.com/media/pdf/techspecs/Nextreme_eTEG_Evaluation_Kit_Application_Note.pdf.
- [22] A. K. Jain and R. Ayyanar, "Standard Handbook for Electrical Engineers - Section 22 Power Electronics," McGraw-Hill, 16th ed., 2006.
- [23] MAXIM, "Pulse-Width Modulator Operates at Various Levels of Frequency and Power," 2004. <http://pdfserv.maximintegrated.com/en/an/AN3201.pdf>.
- [24] Xu Huang, K. D. T. Ngo and G. Bloom, "Design techniques for planar windings with low resistances," Proc. IEEE Appl. Power Electron. Conf. and Expo., pp. 533 -539, 1995.

- [25] Magnetics. "Fundamental of Tape Wound Core Design."
2000. https://www.google.gr/url?sa=t&rct=j&q=&esrc=s&source=web&cd=1&ved=0CC4QFjAA&url=http%3A%2F%2Fwww.mag-inc.com%2Ffile%2520Library%2FProduct%2520Literature%2FStrip%2520Wound%2520Core%2520Literature%2Ftwc-s1.pdf&ei=TjMrUvPUJcqtAaR7ICgBw&usg=AFQjCNGMRHnUglZP2zHEgNxArOu-anPiQg&sig2=a5BJceW1TR9JO9H_BSEMIw&bvm=bv.51773540,d.Yms&cad=rja.
- [26] Magnetics. "Designing with Planar Ferrite Cores."
2001. https://www.google.gr/url?sa=t&rct=j&q=&esrc=s&source=web&cd=1&ved=0CDAQFjAA&url=http%3A%2F%2Fwww.mag-inc.com%2Ffile%2520Library%2FProduct%2520Literature%2FFerrite%2520Literature%2Ffc-s8.pdf&ei=-TgrUrLMIoLQtAbUtIGYBQ&usg=AFQjCNH-zXZ_hGbtKx8pIk44iTeYrAPsoA&sig2=c0JfyqvamcCOSsRHiwFLA&bvm=bv.51773540,d.Yms&cad=rja.
- [27] Magnetics. "Inductor Design in Switching Regulators."
2000. https://www.google.gr/url?sa=t&rct=j&q=&esrc=s&source=web&cd=1&ved=0CDAQFjAA&url=http%3A%2F%2Fwww.mag-inc.com%2Ffile%2520Library%2FProduct%2520Literature%2FGeneral%2520Information%2Fsr-1a.pdf&ei=ZjgrUpWpA4rctAb0xIHACA&usg=AFQjCNG34_KRA5yc3k-mHSqzWSCW0Wfm7g&sig2=-2vT-YcC04Z9gdIefUVd4w&bvm=bv.51773540,d.Yms&cad=rja.
- [28] Magnetics. "Curve Fit Equations for Ferrite Materials."
1999. https://www.google.gr/url?sa=t&rct=j&q=&esrc=s&source=web&cd=1&ved=0CDAQFjAA&url=http%3A%2F%2Fwww.mag-inc.com%2Ffile%2520Library%2FProduct%2520Literature%2FFerrite%2520Literature%2FFC-S7.pdf&ei=wjcrUviJCMvPsgbRzYDwDw&usg=AFQjCNEwhTiCuDx7vyubiGXwTJg_bvoqgA&sig2=S5ckYpB2pBPGbFkvi-GUnw&bvm=bv.51773540,d.Yms&cad=rja.

- [29] R. West, "Common Mode Inductors for EMI filters require careful attention to core material selection," Powerconversion and Intelligent Motion-English Edition 21.7, pp. 52-59, 1995.
- [30] Magnetics. "Tape Wound Cores."
2000. <http://www.datasheetarchive.com/indexer.php?file=DSA0013329.pdf&dir=Datasheet-054&keywords=TWC-500&database=user-highscore#>.
- [31] http://www.micrometals.com/material/pc_coreloss_txt.html.
- [32] R. C. Pilawa-Podgurski, N. A. Pallo, W. R. Chan, D. J. Perreault, and I. L. Celanovic "Low-power maximum power point tracker with digital control for thermophotovoltaic generators," Proc. Twenty-Fifth Annual IEEE Applied Power Electronics Conf. and Exposition, pp. 961-967, 2010.